SAPIENZA
UNIVERSITÀ DI ROMA

Electronic structure and properties of materials for artificial photosynthesis

Dipartimento di Scienze di Base e Applicate per l'Ingegneria

Dottorato di Ricerca in Mathematical Models for Engineering, Electromagnetism and Nanoscience – XXXI Ciclo

Candidate

Aliya Tychengulova

ID number 1690536

Thesis Advisor

Professor Leonardo Guidoni

October 2019

Thesis defended on 19-02-2020
in front of a Board of Examiners composed by:

Professor Claudio Goletti (chairman)

Professor Massimo Gurioli

Professor Laura Micheli

Electronic structure and properties of materials for artificial photosynthesis
Ph.D. thesis. Sapienza – University of Rome
ISBN: 000000000-0

This thesis has been typeset by LaTeX and the Sapthesis class.

Version: 19-02-2020

Author's email: tychengulova.1690536@studenti.uniroma1.it

Dedicated to
My family

Acknowledgements

My research work and education would not have been possible without the support of a number of people. My first thanks goes to my supervisor Prof. Leonardo Guidoni and CBBC group members, first and foremost, Matteo Capone. They kindly accepted me into their research group without reservation and guided me through the years of my graduate education and research.

In the CBBC group, I have been privileged to work with many creative and intelligent colleagues with unique personalities. I am grateful to have had the opportunity to learn from all of them.

Finally I would also like to express my deepest thanks to my parents and my family who have supported me throughout my studies. Their words of encouragement have helped immensely during my PhD.

Contents

Abstract

The oxygen evolution reaction during the photosynthesis process performed in plants, algae and cyanobacteria is possibly one of the most important reactions on the planet that sustain most life on our planet. Understanding the structure and function of the "engine of life", the oxygen-evolving complex (OEC) in the active site of Photosystem II (PSII), has been one of the great and persistent challenges of modern science. Over the past decades, immense progress has been achieved in understanding the structure and mechanism of photosynthetic reactions. This progress is in large part due to the refinement of preparative protocols, X-Ray Diffractometry (XRD), site-directed mutagenesis, Electron Paramagnetic Resonance (EPR) spectroscopy, the coming of age of X-ray Free Electron Laser (XFEL) diffractometry and computational approaches in the investigation of PS II. Nevertheless, key mechanistic and electronic details of water oxidation still remain highly contentious. Elucidation of these details is complicated by the fact that the active site of PSII exists in four natural metastable oxidation states, as well as putative unnatural forms that are plausibly induced during experimental investigation.

The leading motivation of the scientific community studying PSII is ultimately the development of new catalysts and even bio-inspired solar cells, that will produce clean and sustainable energy for the world. Over the last hundred years, approximately 80% of worldwide energy consumption has been based on fossil fuels, including coal, oil, and natural gas. However, humankind now has to face the consequences arising from this dependence on fossil fuels. Worldwide energy consumption is expected to increase by over 50% by the mid-2000s (see Fig. 0.1). Because fossil fuels are finite and regional around the world, it is greatly challenging to ensure that this demand can be met, in the face of possible political tensions and other potential problems with energy supplies. Due to the usage of fossil fuels, large quantities of emissions, e.g., CO_2, SO_2, and oxide particles, are the predominant reasons for global warming and severe pollution. Recent reports from the Intergovernmental Panel on Climate Change emphasized the necessity of decreasing CO_2 emissions on a global scale to the zero level before the next century. These arguments make the development of sustainable and carbon-neutral energy technologies one of the most urgent challenges facing humankind all over the world. Wind, ocean currents, tides, and waves are all potential sources of energy, but by far the most abundant renewable energy source on the planet is solar energy: solar illumination on Earth every hour is greater than the worldwide energy consumption for a whole year [35]. Therefore, the conversion and utilization of solar energy is a promising solution for energy problems. An intriguing potential solution to the expected shortfall in energy supplies is artificial photosynthesis [108], whereby light energy can be stored

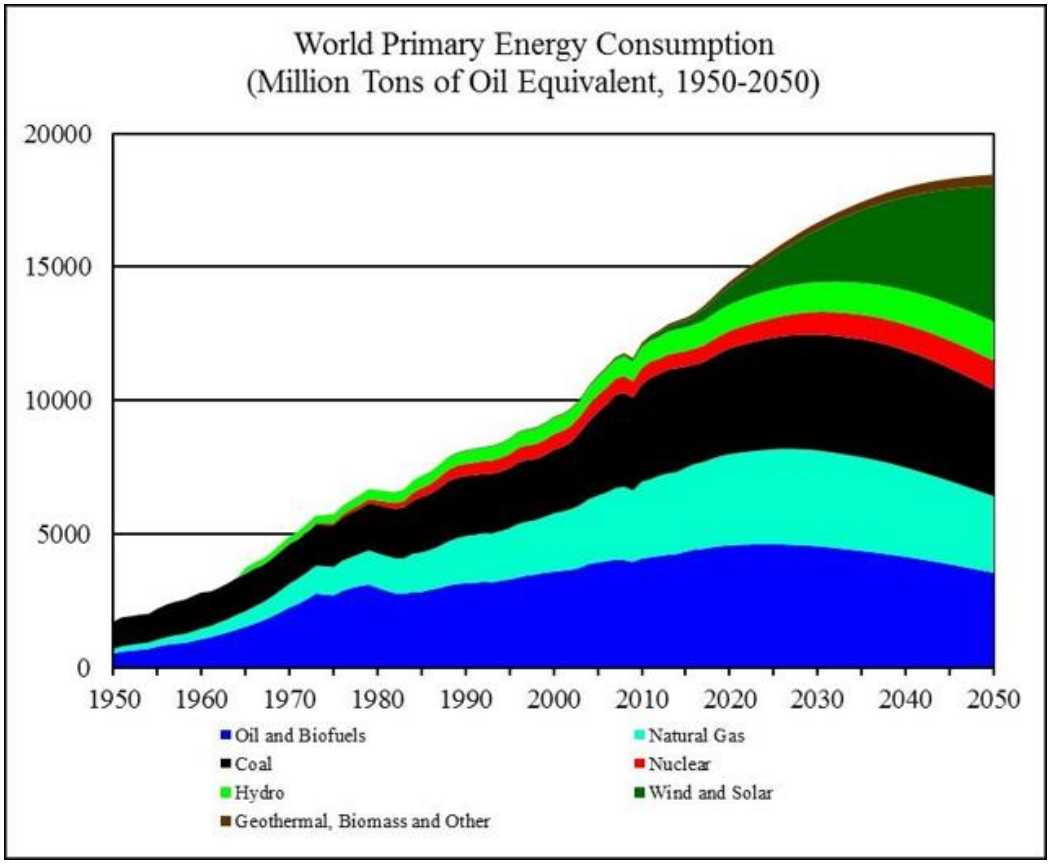

Figure 0.1. World primary energy consumption

in chemical bonds and, hence, be made available as fuels [18, 200, 19, 364].

Synthetic molecular and heterogeneous manganese analogues still struggle to mimic the function and performance of the OEC. This is partly because these distinctive features are not intrinsic to the Mn_4CaO_5 core of the OEC but depend on its environment and result from elaborate gating and regulation mechanisms for coordinating the coupling of proton-electron transfer and the access, delivery, binding, positioning, activation, and coupling of substrate waters to form dioxygen. The high level of geometric and electronic control, both spatial and temporal, extends along the whole catalytic cycle and involves simultaneously the Mn_4CaO_5 cluster, its first coordination sphere, and the protein matrix that controls the flow of electrons, protons, substrates, and products.

From the side of theoretical methods great progresses have been made in recent years. Due to the success of the density functional theory (DFT), not only in the field of solid state physics, but also on liquids and molecular compounds, it is possible to obtain the electronic structure of few hundreds atoms with an acceptable computational effort. Using the information provided by the experiments as starting point, it is possible to employ DFT to refine the geometries in relationship with the electron ground-state or different electronic states, to calculate the electron and spin density for a given system and to estimate spectroscopic properties. The coupling of DFT with molecular dynamics also allows us to perform ab-initio

molecular dynamics of large systems at finite temperature to fully consider entropic contributions and low-energy conformational changes. Computational techniques can also provide considerable support in the analysis and interpretation of the complex IR spectra of such biological systems. In this thesis, the molecular and electronic structures of the multinuclear manganese containing bioinorganic system together with oxygen-evolving complex of PS II are investigated using DFT-based methods for the theoretical modeling of vibrational spectra in the gas phase by normal mode analysis and molecular dynamics simulations.

Research on biological water oxidation traverses scientific fields and concentrates the efforts of a multitude of experimental and theoretical approaches. Different methods of investigation naturally lead to distinct views on the OEC. These are often complementary but at times are contradictory, and it is not always obvious whether the contradictions already exist in the data or arise from their suggested interpretations. Nevertheless, the overarching goals are common to all experimental and theoretical studies. These are not limited to the geometric and electronic structure of the cluster in each state of the cycle but encompass the role of the protein matrix, the channels, and secondary components of the second sphere of the cluster, such as the chloride ions.

Chapter I of the thesis considers in detail the progress that have been done so far in structural and spectroscopic studies of OEC and its synthetic mimics given together with the general introduction on photosynthetic reactions occurring in the leaf. Theoretical background of the computational methods used in present work is given in detail in Chapter II.

In this thesis, we explored the potentialities and the reliability of different state-of-the-art computational techniques for the investigation of the structural and vibrational properties of complex macromolecular materials of biochemical importance. The use of FTIR spectroscopy to probe the structure and function of the OEC complex in PS II has a long history. The synthesis of a very close structural mimic of the catalytic center has opened up the opportunity to perform a comprehensive and parallel study of both the natural and artificial compounds and of their vibrational modes. Chapter III is dedicated to the detailed assignment of the bands in the mid- and low-frequencies region by static and dynamic vibrational spectra calculations of the unique biomimetic complex. The detailed parallel analysis between the Natural and Synthetic complexes also provided a comprehensive characterization of the vibrational fingerprints in such class of cubane-like Mn-based compounds and is reported in Chapter IV. In Chapter V of the thesis we discussed the electronic and structural properties of the novel Mn_4O_4 synthetic compound mimicking the EPR spectroscopic nature of OEC in S_2 state.

Chapter 1

Historical perspective and general introduction

Oxygenic photosynthesis is evolutionary process for the conversion and storage of solar energy based on abundant and non-toxic elements. And, as it is assumed that photosynthesis is converting solar into chemical energy at a rate of about 120 TW per year [35], it is an outstanding paragon for sustainable energy production. But to realize a technical process for energy production inspired by photosynthesis, it is crucial to understand the fundamental reactions of the biological complex. Hence, a brief overview on the reaction pathways of photosynthesis taking place in plants and water-oxidation catalysis in particular will be given. Also, the term photosynthesis will be used synonymous with oxygenic photosynthesis in the following.

Schmitt and coworkers describe plant metabolism at its base as the 'capture of solar radiation and transformation into Gibbs free energy'. [307] This sentence expresses the underlying truth that the Earth lies in a thermodynamic gradient between the Sun and the cold vacuum of deep space, and that the ultimate provenance of almost all biochemical energy on Earth is the fixation of solar energy in the form of thermodynamically unstable chemical species.

The evolution of photosynthetic life on Earth precipitated epochal changes in Earth's biogeochemistry, including the considerable reconstitution of the ancient atmosphere [18]. It is photosynthesis that is responsible for almost all free dioxygen on the planet, and the generation of this oxygen by the emergence of photosynthetic organisms approximately 2.4 Ga before present is correlated with considerable changes in the palaeogeochemical record. Notably, increasing oxygen concentrations in the atmosphere and oceans precipitated a mass extinction of anaerobic life. This transition in Earth's palaeobiogeochemical history is termed the 'oxygen catastrophe', and was also accompanied by a dramatic drop in the atmospheric concentration of CO_2 and H_2 Nevertheless, the oxygenation of the atmosphere paved the way for aerobic respiration and the wide variety of complex lifeforms it supports.

Oxygen is produced by photosynthetic water oxidation in plants, algae, and cyanobacteria. The water-oxidation reaction probably first appeared in nature ~ 3 billion years ago in the precursors to present-day cyanobacteria, although the exact timing is not yet entirely clear [375, 28, 6]. A key component in the appearance of oxygenic photosynthesis was a metal complex that could store oxidizing equivalents to

facilitate the four-electron oxidation of two water molecules to dioxygen, meanwhile making the electrons available for the reductive carbon-fixing reactions required for sustaining life [155, 8, 304]. This metal complex involved in photosynthesis, the oxygen-evolving complex (OEC), consists of an oxo-bridged structure with four Mn atoms and one Ca atom. No variations have been observed so far among photosynthetic organisms through higher plants and algae back to cyanobacteria, which represents the earliest photosynthetic organisms. Oxygen itself is the byproduct of the photosynthetic water oxidation reaction shown in equation 1.1:

$$2H_2O \rightarrow O_2 + 4H^+ + 4E^- \tag{1.1}$$

However, it was this oxygen that enabled oxygenic life to evolve and that led to the current diverse and complex life on earth by dramatically increasing the metabolic energy that became available from aerobic respiration. Oxygen produced by this process was also key for the development of the protective ozone layer, which allowed life to transition from marine forms to terrestrial life.

We are now going to make a journey into a leaf to explore in more detail where different components of the photosynthetic machinery, that convert sunlight into chemical (or free) energy, are located (Figure 1.1). The inner tissue of a plant is called mesophyll and it is made up of cells specialized in photosynthesis. These cells range from 20 to 40 μm in diameter and 100 to 200 μm in length [210], which is enough to embrace the various plastids of the cell. Plastids are units that have specific functions in the cell and they are shaped as compartments by their enclosing membrane. Their specific functions are executed by different proteins that reside both in the membrane and the inner compartments of the plastids. We will now zoom in further and investigate a plastid known as the chloroplast (Figure 1.1). The chloroplasts range from 5 to 10 μm in diameter [376] and their complex structure is shaped by an intricate system of three different membrane enclosures: the outer, the inner and the thylakoids membrane. The Rubisco protein accumulates at the stromal side of the inner membrane and catalyzes the conversion of carbon dioxide into carbohydrates in a reaction cycle known as the Calvin-Benson cycle [285]. The overall process of carbon dioxide fixation in the stroma can be summarized by a simple chemical equation:

6 CO_2 + 12 $NADPH_2$ + 18 ATP $\rightarrow$ $C_6H_12O_6$ + 12 NADP + 18 ADP + 18 P_i + 6 H_2O

The annual net production of fixed carbon from carbon dioxide via photosynthesis is ~112 000 billion kilogram [151] and this production is energy demanding. It can be seen from equation above that for every carbon dioxide that is fixed to a growing chain of carbohydrates two NADPH molecules are oxidized and three ATP molecules are hydrolyzed. NADPH provides the reducing power to the reaction by giving off two electrons whereas ATP provides energy for the work to be done by giving off a phosphate (P_i). This phosphate binds to a three carbon intermediate, making it more reactive and ready to accept electrons from NADPH. The reactions in the Calvin cycle are not directly dependent on the presence of light and are therefore described as the dark reactions of photosynthesis. The NADP and ADP molecules formed during the dark reactions need to be regenerated into NADPH and ATP by a series of reactions that are known as the light reactions.

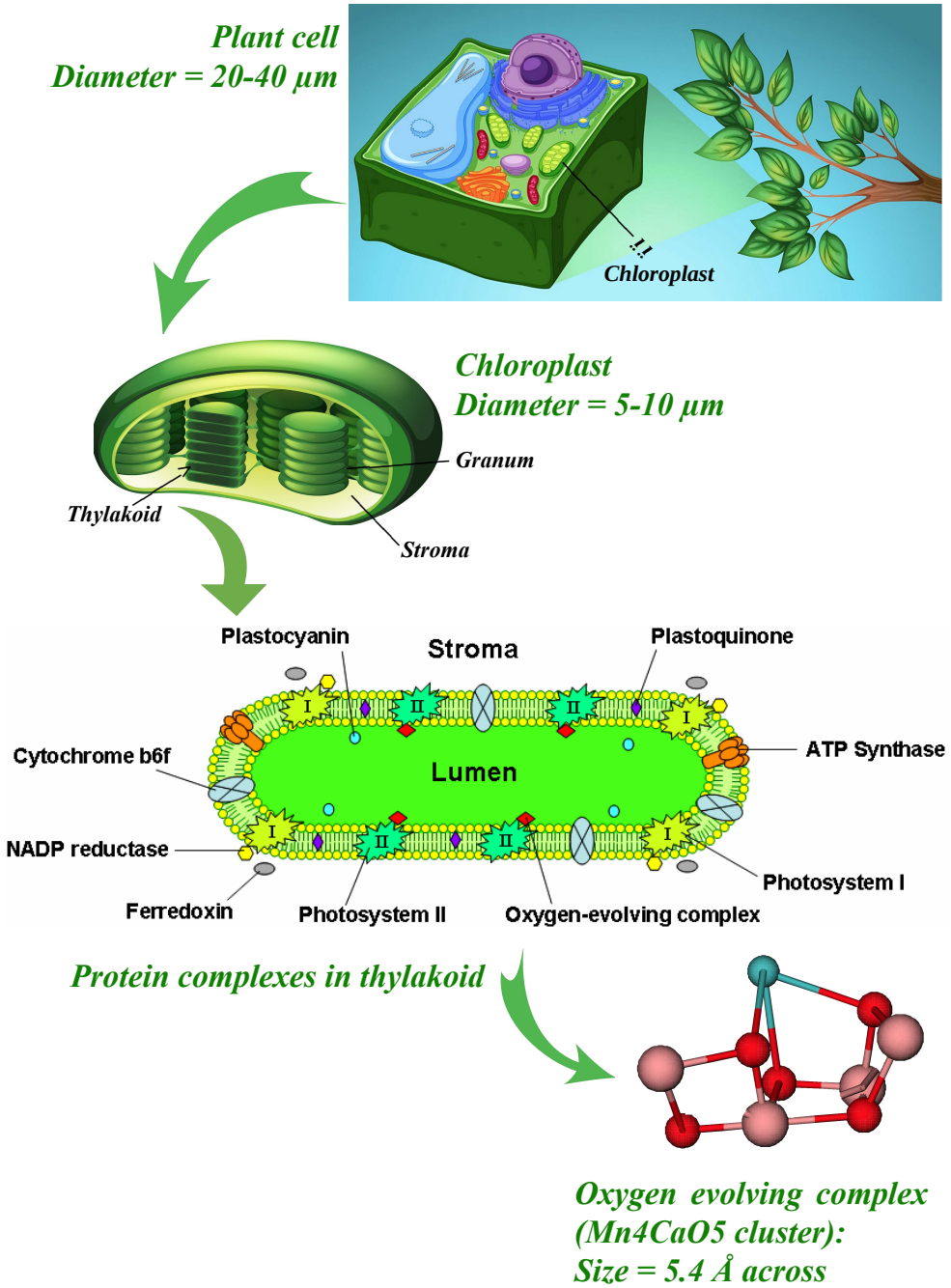

Figure 1.1. Overview of the main photosynthetic components inside a plant leaf. Image of Mn_4CaO_5 cluster was prepared from PDB

We are now going to continue to explore the chloroplast and take a look the protein complexes that carry out the light reactions by zooming into the very special shape of thylakoid membranes (Figure 1.1). The thylakoid membrane encloses the lumen. In higher plants the thylakoid membrane folds to disk shaped, stacked bodies known as grana which are connected with each other via the unstacked stroma lamellae. The first stage of the light reactions takes place in PS II that is localized in the grana. The cytochrome b_{6f} complex is distributed in both grana and stroma lamellae, whereas Photosystem I (PSI) and the ATP synthase are present in the edges of the grana and in the stroma lamellae [5]. The cooperation between PSII and PSI generates an electron current from H_2O to NADP, producing reducing power in the form of NADPH, and the byproduct O_2.

It is PSII that contains the catalytic center for water oxidation, which is also known as the OEC. The width of PSII homodimer in *T.Elongatus* is ∼110 Å [109] and in order to be able to observe the OEC, we have to further zoom in until we reach the atomic scale (Figure 1.1). The OEC harbours the chair shaped Mn_4CaO_5 cluster, which measures 5.4 Å across [349]. Oxygenic autotrophs such as cyanobateria, algae and plants all contain the Mn_4CaO_5 cluster and the annual net production of O_2 has been estimated to be $\sim 2.7 \times 1014$ kilogram [20]. In the following section oxygen evolution and light reactions are described by following the path of an electron as it is transferred from one cofactor to another, starting with water and PSII, and ending with Ferredoxin – $NADP^+$ reductase (FNR) and NADPH.

1.1 Photosystem II: Biological Function and Electron Transport Chain.

1.1.1 Biological function

The photons from the sun are absorbed by pigment molecules that are assembled in light harvesting systems inside PSI and II, and in special antenna complexes associated with the photosystems (e.g. LHC I, LHC II or phycobillisoms). The main pigments in higher plants are chlorophyll *a* and *b*, and the light harvesting system connected with each photosystem contains normally around two-to-three hundred pigments of this type. The absorption of one photon leads to the excitation of one electron into an excited state of the chlorophyll molecule. This excitation energy is transferred through the whole antenna to a reaction center that traps the energy by charge separation. In PSII the reaction center contains four chlorophyll a molecules P_{D1}, P_{D2} Chl_{D1} and Chl_{D2}, which are collectively known as P680, and a pheophytin molecule. The P denotes pigment and 680 is the maximum of the low-energy absorbtion peak expressed in nanometers. The arrival of excitation energy from one photon at P680 expels one electron from P680 to the nearby pheophytin molecule. The radical cation $P680^{\bullet+}$ formed has a potential of around $+1.25V$ and it is the strongest oxidant known for a biological system [288, 287]. We will see in a coming section that this voltage is insufficient to extract electrons from a water molecule directly, but that it is high enough to drive water oxidation via tyrosine Z and the Mn_4CaO_5 cluster.

PSI has a light harvesting system that is similar to that of PSII, but the reaction

center and the redox cofactor differ. The reaction center in PSI is known as P700 due to its further red shifted absorption maximum. It is formed by a pair of chlorophylls $_e$C-A1/$_e$C-B1 that act as the primary electron donor to a nearby chlorophyll pair known as A_0 $_e$C-A/B-3. The P700/P700$^{\bullet+}$ midpoint potential has a value of about + 500mV [292, 107].

The absorption of light by PSII and PSI drives a linear flow of electrons from H_2O to NADP that involves a number of other electron transfer cofactors and complexes. Having two light driven photosystems that are coupled was proposed in the 1960s [141]. The authors depicted this in a redox potential diagram that later became known as the Z-scheme of photosynthesis due to its likeness with the letter Z (if rotated by 90 °). The Z-scheme (Figure 1.2) marks the different reduction potentials of the molecules that transport the excited electron from water to NADP. With the exception of the two charge separations in the reaction centers, these electron transfer events are always connected with the loss of potential energy. While wasteful, this arrangement leads to the exceptional high quantum yield of photosynthesis, since the loss of potential energy difference and the increase in spatial distance connected with the linear electron flow reduces the likelihood of potentially harmful charge separations even under low light conditions [336]. As such the excited electron from P680*moves from a negative to positive redox potential until it reaches P700$^{\bullet+}$ where it gets excited a second time. Part of the potential loss between the two photosystems is recovered by coupling these electron transfer steps with the 'pumping' of protons from the stroma into the lumen. The sequence of electron transfer reactions in PSII and PSI will be described in the following subsection.

1.1.2 Electron Transport Chain

Six different protein complexes participate in the electron transport chain: PSII, Cytochrome b_6f, Plastocyanin, PSI, Ferredoxin, Ferredoxin-NADP reductase and ATP synthase (Figure 1.3). The light reactions of the electron transport chain (ETC) produce reducing power (NADPH) and a proton motive force to be used for the synthesis of ATP. Oxygen is released as a byproduct in the electron abstraction reaction that takes place in PSII.

Absorption of one photon by the chlorophylls (Chl) in the LHC of PSII leads via excitation energy transfer to the reaction center to the excitation of P680. The primary charge separation is assumed to occur between the Chl_{D1} of P680 and a nearby pheophytine ($Pheo_{D1}$). The transfer of one electron from Chl_{D1} to $Pheo_{D1}$ creates the radical cation P680$^{\bullet+}$ in which the subsequently formed $P^{\bullet+}_{D1}$ is the strong oxidant that is required to oxidize water. The oxidizing power of P_{D1} is around $+1.25V$ [288, 287]. To avoid charge recombination between P680$^{\bullet+}$ and Pheo$^{\bullet-}$ the electron is rapidly transferred (200-500 ps) [257, 345, 32] from Pheo$^{\bullet-}$ to a tightly bound plastoquinone (Q_A) that is located on the stromal side of the thylakoid membrane. Due to its special protein environment it can only act as one-electron acceptor. The electron is thereafter transferred to the mobile secondary plastoquinone (Q_B). After the arrival of a second electron from the next charge separation in the reaction center, it takes up two protons from the stroma. The thus formed platoquinol molecule (QH2) leaves its binding pocket at the acceptor side of

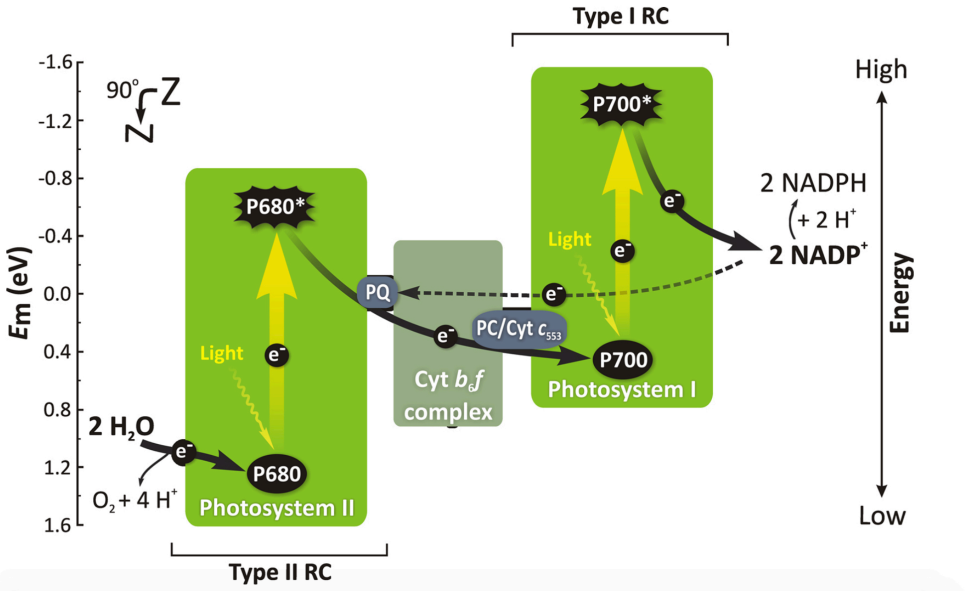

Figure 1.2. The electron flow from H_2O to NADP in PSII. The main components in this transport chain are: the oxygen evolving complex (OEC or Mn_4CaO_5 cluster), tyrosine Y_Z (Y_Z), a tetrad of chlorophyll molecules (P680), pheophytine (Pheo), plastoquinone (Q_A) (Q_B), cytochrome b_{6f} ($Cytb_{6f}$), plastocyanin (Pc), a pair of chlorophyll molecules (P700), a pair of chlorophyll molecules (A_0), a pair of phylloquinones (A_1), an iron-sulfur complex (4Fe-4S), ferredoxin (Fd), ferredoxin-NADP reductase (Fd-NADP reductase). From ref. [125]

PSII and the empty Q_B binding pocket is quickly occupied with a new plastquinone molecule. QH2 diffuses into the thylakoid membrane where it is oxidized by the $Cytb_6f$ complex. The released electrons flow one at a time through a Fe-S protein that reduces platocyanin, a soluble electron carrying protein that transfer the electron to PSI. The two protons that were taken up from the stroma are released into the thylakoid lumen together with two additional protons from the stroma that are pumped by the electron transfer reactions occurring at the Cytb6f complex. Protons from the water oxidation reaction also contribute to creating a proton concentration difference across the thylakoids membrane. This results in a proton motive force that drives the ATP synthesis by sending protons through the ATP synthase back into stroma. The electron that was delivered by plastocyanin to PSI is excited a second time by P700. The electron is then transferred to a pair of chlorophylls (A_0) and further to a pair of phylloquinones (A_1) that reduce a 4Fe-4S cluster. A soluble protein called ferredoxin transports the electron from PSI to the ferredoxin-NADP reductase that catalyzes the formation of NADPH.

1.2 The Oxygen-Evolving Complex

The OEC is embedded in PSII, a membrane pigment-protein complex, where the primary charge separation by absorbed sunlight energy and successive electron transfer occurs through several vectorially arranged pigment molecules (Fig. 1.4). The

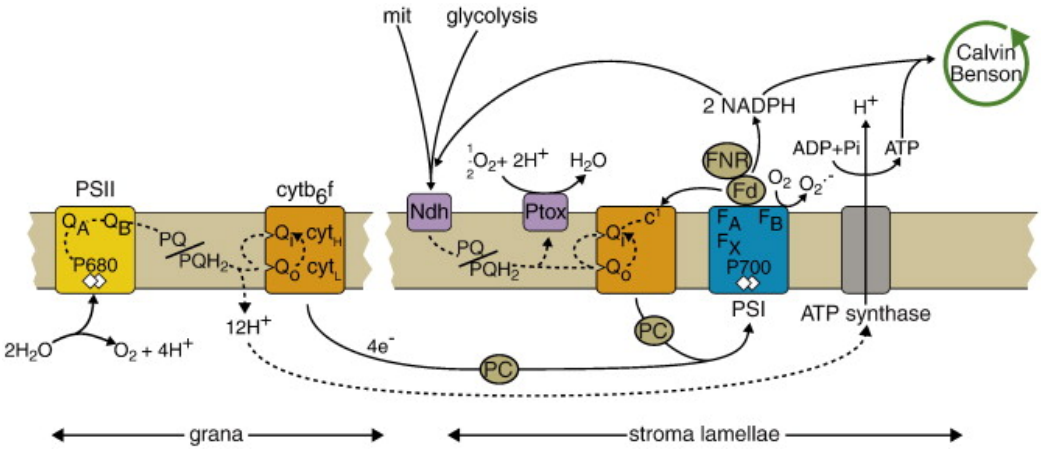

Figure 1.3. Electron transport pathways of oxygenic photosynthesis. The thylakoid membrane with PSII, Cytb$_6f$, PSI, and the ATP synthase is shown. Electron transport pathways are shown by dotted lines with arrows to indicate the direction of electron flow. From ref. [296]

electrons and protons produced in the water oxidation reaction in PSII are ultimately used to store energy in the form of ATP and to reduce CO_2 to carbohydrates via the Calvin-Benson cycle, and are the precursors for synthesis of the biological molecules needed by the organism. Nature has thus evolved an elegant way to store sunlight energy in the form of chemical energy, and it is this form of energy created by photosynthesis that all life depends on.

In the Bioinorganic Enzymology issue of Chemical Reviews in 1996, the Mn cluster in PSII was reviewed [381]. In the almost 23 years since then, there has been an enormous amount of progress in the field with new studies in X-ray spectroscopy [386, 87] and crystallography [397, 161, 109, 208, 131, 349, 184, 335], in addition to many other spectroscopic and biochemical studies, that have had a profound effect on the understanding of the structure and mechanism of photosynthetic water oxidation. In this chapter, we summarize the current understanding of the structure of the Mn_4CaO_5 cluster, as well as the water oxidation reaction based on the insights learned from various spectroscopic techniques.

The biological catalyst, PSII, has been studied in detail for more than 50 years. Progress in understanding the site of catalysis, the OEC, has depended on advances in several fields, including biochemistry, biophysics, spectroscopy, inorganic chemistry, and computational chemistry. While many properties of the OEC are well documented and generally agreed upon, many aspects of the catalytic site remain controversial, with computational and experimental chemists still pushing the boundaries of our understanding of the OEC.

1.2.1 Structural proposals for the OEC: Historical Perspective

For quite a while X-ray crystal structure of the reaction centre of purple bacteria [93] served as scaffold for discussing the structure of PSII. Several labs tried to reveal the structure of PSII from spectroscopic data without any proper structural model. Thus, Gary Brudvig's group proposed a tetrameric Mn_4O_4-cluster in a cuban-like

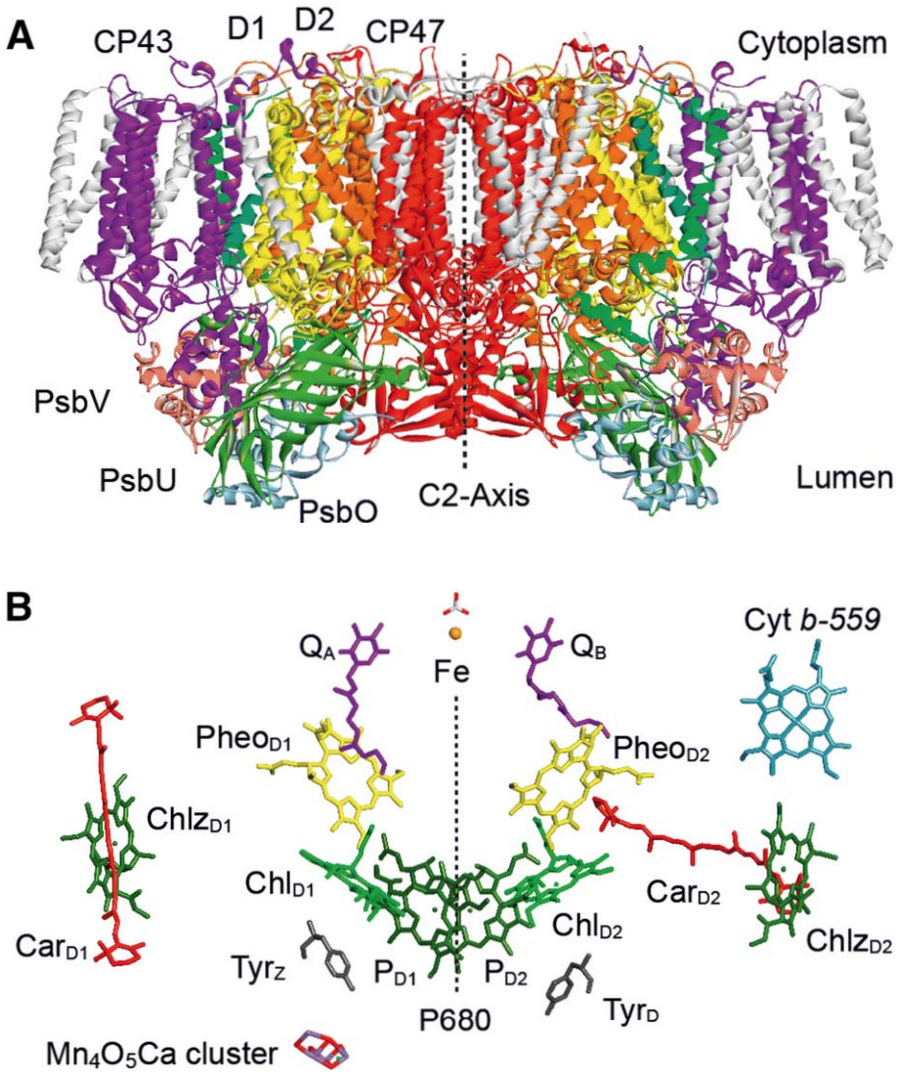

Figure 1.4. PSII structure from 1.9 Å data from X-ray crystallography showing the membrane spanning helices and the extrinsic polypeptides. The location of the cofactors involved in charge separation and the Mn_4CaO_5 cluster in the membrane are shown highlighted against the polypeptide background. The Mn_4CaO_5 cluster is on the lumenal side of the membrane with the acceptor quinones on the stromal cytoplasmic side of the membrane. From ref. [335]

arrangement for OEC [88]. Their assumption was based on the similarity between exchange coupling constants from the EPR signals of the S_2 state of OEC and the EPR signals of certain Fe_4S_4 proteins of known structure.

Berkeley group started investigations of the state of manganese in PSII by X-ray absorption near edge structure (XANES) and Extended X-ray absorption fine structure (EXAFS) using synchrotron radiation that was tuned to the K-edge of manganese and calcium ions. The former gives information on valence states, the latter yields the distance between the primarily excitation and its neighbours. The results of the Berkeley group were presented in a series of reviews [379, 382]. The Mn–Mn distance of 2.7 Å was attributed to di–μ–oxo–linked Mn–Mn and the 3.3 Å one to mono–μ–oxo–linked Mn–Mn, respectively, by comparison with data on Mn-model complexes of known structure (e.g. [61, 374]. The Berkeley group proposed a Mn4-model of two di–μ–oxo–linked Mn-dimers that are linked by one mono–μ–oxo bridge (the dimer of dimers model) [379, 382].

Berlin group first reported the crystallographic structure of PSII from *Thermosynechococcus (T.) elongatus* with 3.8 Å resolution in 2001 [397]. It revealed a dimeric structure of PSII, the relative positions of its large subunits, the transmembrane helices, the position and orientation of cofactors (chlorophylls, Y_z, quinones, cytochromes), and the position and shape of Mn4Ca as a whole, however without detail on the mutual arrangement of the metal ions. But the positions of the atoms in the OEC were not allowed to be determined due to the radiation damage induced by the intense X-ray beam used in X-ray diffraction (XRD) spectroscopy. Jian-Ren Shen and Nobuto Kamiya determined the structure of OEC crystals at 3.7 Å resolution [161]. The results were very close to those from the Berlin group except some new features on metal ligands and certain carotenoids. Eventhough, the detailed structure of the inorganic core was still missed.

James Barber in collaboration with So Iwata obtained a fully refined structural model of PSII at 3.5 Å resolution [109]. "London model" of the metal cluster was proposed in the form of heterometallic cubane structure with the fourth Mn dangling out. The metal ions were bridged by four oxygen atoms and ligated by four H_2O molecules. The inorganic core was ligated by four protein residues with Y_z = D1-Y161 and its hydrogen-bonded partner, D1-H190. In 2005, the Berlin group presented a model at 3 Å resolution with all carboxylate residues being bridging bidentate [208].

The EXAFS studies from Berlin group [85] reported shorter Mn-Mn bond length compared to "London model" which caused serious doubt on the valence-state of the Mn4Ca cluster. This discrepancy has been clearly explained by the work of [387] where they demonstrated that X-ray exposure reduced Mn4 from the expected valence of state S_1 (III,III,IV,IV) to (II,II,II,II). Such an X-ray photoreduction of the metal ions represents a local radiation damage which generates free electrons interacting with high-valent manganese ions with extraordinary electrophilicity. At the same time Wolfgang Lubitz's group determined the valence-set of the four Mn-ions by ^{55}Mn-pulse NMR as (III,III,III,IV) in S_0 and (III,IV,IV,IV) in S_2 [191].

Subsequent work on the atomic structure has been aimed to (a) minimization of radiation damage, (b) improved spatial resolution, (c) selective characterization of the five functional states S_0 to S_4 and (d) time resolution of structural transitions between them. The latter necessitates X-ray diffraction at room temperature.

The first high-resolution structure of PSII at 1.9 Å was published by Jian-Ren Shen and Nobuo Kamiya [349]. It revealed the structure which contained the Mn_3Ca cubane with the dangling Mn from "London model" and the ligand structure of "Berlin model". For the first time, the bridging oxygen atoms and four water molecules were clearly resolved, and former Mn_4CaO_4 became $Mn_4CaO_5(H_2O)_4$, as illustrated in Fig. 1.5. This structural model was obtained by continuous synchrotron radiation (CW-XRD), and at cryogenic temperature. The Mn-Mn distances were still slightly longer than in both, EXAFS experiments and DFT calculations, and hence still indicative of some radiation damage.

Shen and his colleagues also conducted XFEL experiments. In contrast to the former group they used large crystals with volume-per-volume exposure at cryogenic temperature. In 2015 they presented a 'damage-free' structural model at a resolution of 1.95 Å [335]. The Mn–Mn distances were shorter than previously obtained by conventional CW-XRD [109, 349], and they were better compatible with those from EXAFS.

The obvious challenge was now to determine the damage-free structure of the catalytic center at room temperature, in its different oxidation states (S_0, ..., S_4), and, if possible, time resolved. In 2016 the Berkeley–Berlin team published a XFEL-study on structural differences between states S_1 and S_3 of the metal cluster, as function of the temperature, and with and without ammonia bound [391]. With ammonia the authors mapped those water binding sites in the metal-cluster that are not involved in the formation of the O–O bond. While temperature affected some positions of transmembrane α-helices and redox-cofactors, the proper Mn_4CaO_5-cluster was practically invariant to temperature. At a resolution of 2.25 Å the authors did not detect differences between the dark state (S_1) and the 'two flashes advanced' state (mainly S_3) [391].

A detailed understanding of the catalytic process of water oxidation in PSII requires knowledge of the electronic structure, i.e., the distribution of the electrons in the cluster, in all consecutive reaction steps. The oxidation and spin states of the Mn ions, representing the total number and configuration of electrons in the Mn valence orbitals, give a basic description thereof. These together with the magnetic interactions between the spin-bearing Mn ions, depending to a large part on the metal ligands, provide a comprehensive picture of the respective electronic state, which governs the chemical and catalytic properties of each S state. Thus, the spin states provide information about how the structure of the cofactor evolves during the S-state cycle, for a recent review see [189]. For a more extensive and detailed description of photosynthetic water oxidation in PSII the reader is referred to some recent reviews [264, 158, 315, 358, 385].

1.2.2 Kok-Joliot cycle

In 1968 Anne and Pierre Joliot have raised studies of photosynthetic oxygen evolution to a kinetic level by introducing a rapidly responding oxygen electrode [157]. When they excited dark adapted Chlorella cells with a series of short light flashes oxygen production peaked at flash number 3 and continued with damped oscillations of period four [156]. The release of oxygen occurs in 1 ms, i.e. a 10 times shorter time interval than the overall bottleneck of the full electron transport chain [106]. In 1970

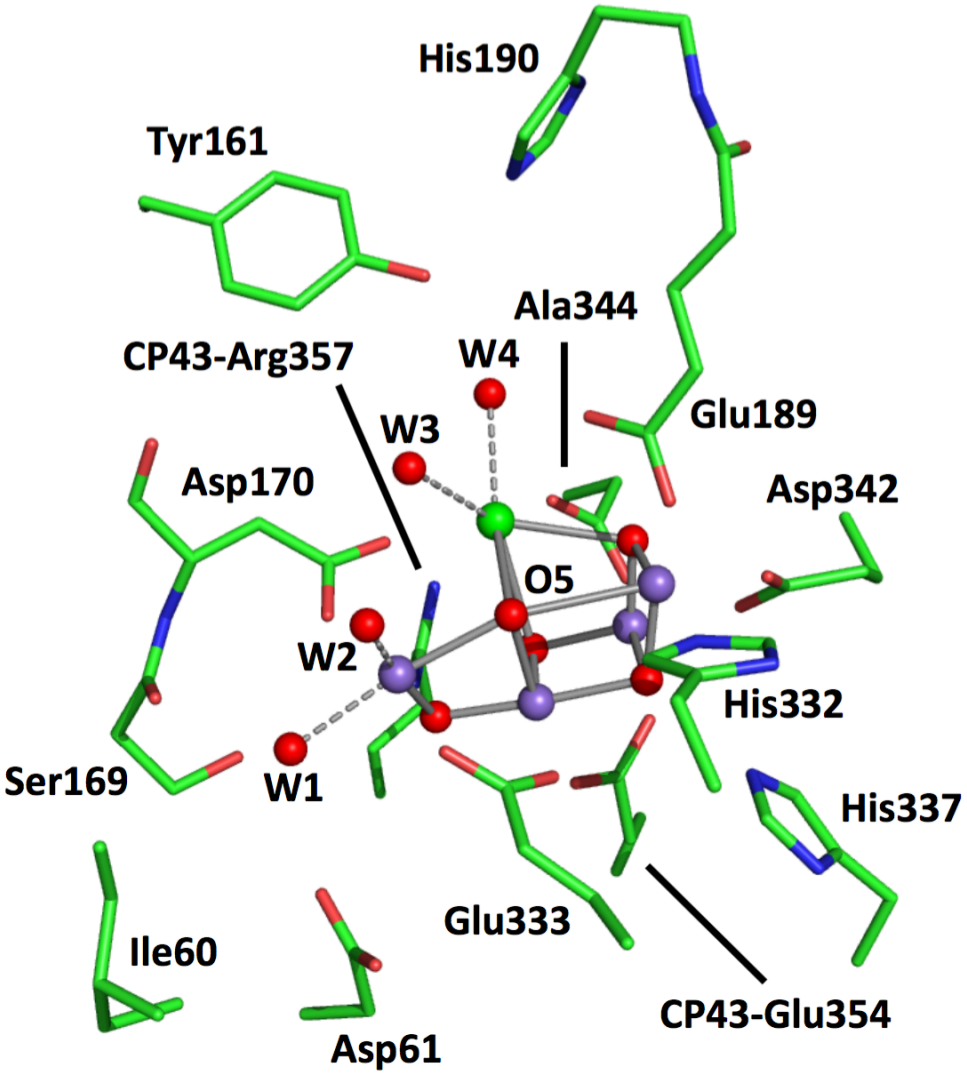

Figure 1.5. Truncated model of the OEC with Mn_4CaO_5 cubane cluster and its closest ligands

Bessel Kok concluded that PSII contains an accumulator of four positive 'charges' that links the one-electron-progression of the photo-physical reaction centre to the four electron/proton-abstraction from two molecules of water to yield dioxygen [182]. From there on, the catalytic centre has been conceived as stepwise progressing in a cycle over five oxidation states, S_0 to S_4. With S1 being the most stable state in dark adapted material, oxygen is only produced after three steps of the cycle during the transition $S_4 \rightarrow S_0$. Two most important features of this four-stepped mechanism were soon recognized (see [290]): (a) the levelling of the energy demand of the four successive one-electron abstractions from water to match the fixed energy input provided by red quanta of light, and (b) the control (by sequestration and/or short lifetime) of potentially harmful intermediates on the way from water to dioxygen ('cryptoradicals' [291]). The cleavage of water to produce dioxygen was expected to liberate protons into the lumen of thylakoids.The stoichiometric H^+/e^--pattern over the four-stepped progression, $S_0 \rightarrow S_1 \rightarrow S_2 \rightarrow S_3 \rightarrow S_4 + O_2$ was 1:0:1:2 [112]. For some time it was controversial between various labs (reviewed in[194]. Different patterns were observed in partially fragmented PSII-preparations. The seeming ambiguity has later been settled in favour of a proton release pattern of 1:0:1:2. It has required the discrimination by kinetic markers between transient electrostatic proton release/uptake at the membrane periphery (membrane Bohr effect) and chemical proton production from the catalytic core of PSII (see review in [159]). It has been early noted that the release of two protons during the terminal, oxygen evolving reaction is kinetically biphasic with one proton appearing at about 100 μs and the other one at 1 ms half rise [112]. The release of a first proton appears as a primer for the terminal reaction cascade involving four electron transfers (see Fig. 1.6).

1.2.3 EPR spectroscopy attempts to unveil the mechanism of water splitting

An experimental method to investigate the electronic structure of transition metal complexes is EPR spectroscopy [123, 2]. It exploits a fundamental property of matter, an intrinsic angular momentum (spin) of electrons (unpaired) which can be excited by microwave radiation in a magnetic field. The unpaired electron spin also interacts with other electron and nuclear spins as well as with local electric field gradients, making it a sensitive reporter of its chemical environment. Since the Mn ions of the OEC inorganic core are open-shell species, i.e., exhibit orbitals with single electron occupancy, whereas most of the electrons of the protein and solvent surrounding are paired, the EPR signals of the Mn_4O_xCa cluster can be detected selectively. It has also been shown that all S states in the Kok cycle can be trapped (except for the elusive S_4 state) and that all exhibit paramagnetism [132].

The first EPR signal observed by Charles Dismukes in 1981 [95] came from the trapped S_2 state. Centered at $g \approx 2$ it included over 20 resolved lines and was thus called "multiline signal". The structure is due to the coupling of the electron spin with the four ^{55}Mn nuclei ($I = 5/2$) via the electron nuclear hyperfine interaction. The EPR signal represents an effective low-spin ground state of $S_{eff} = 1/2$ [29]. The spin state depends on the oxidation state of the Mn ions, their geometry and in particular on the (bridging) ligands which connect the metal ions. These mediate

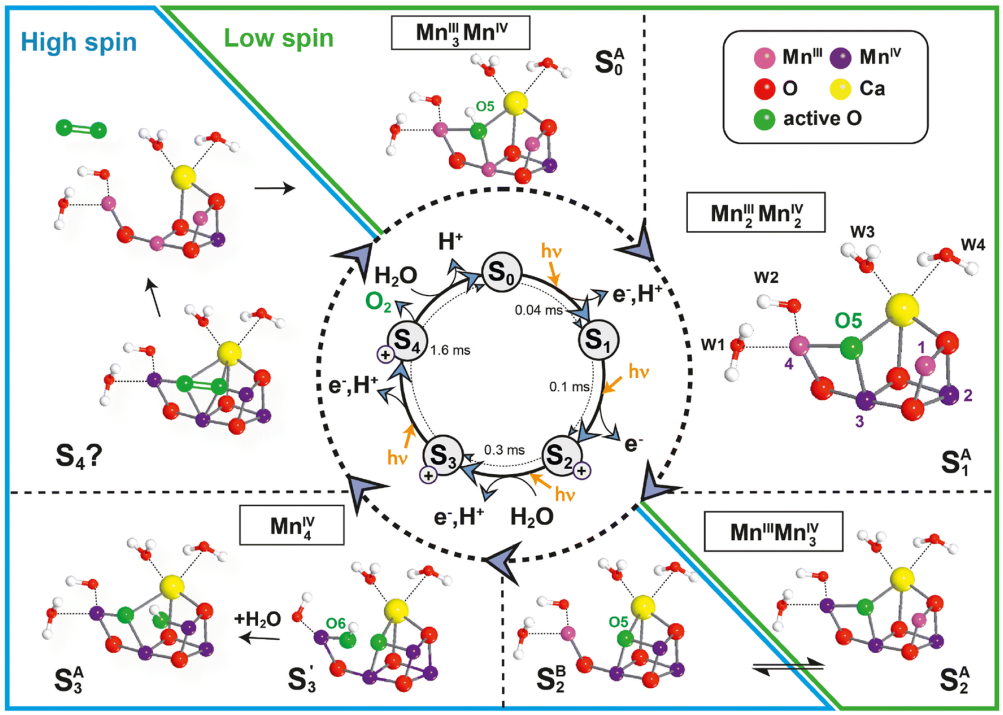

Figure 1.6. Model for the water oxidation cycle in PSII based on spectroscopic and theoretical work [80, 189] detailing the structures of the Mn cluster in the different S states, the water binding events and the O–O bond formation and O_2 release in S_4. The boxes show the determined oxidation states of the Mn ions in the respective S state. A color code is used for the assignment of the MnIII (light purple) and MnIV (dark purple) ions when the OEC is passing through the S states. Note that the oxygens of the waters and μ–oxo bridges are given in red except for the proposed substrate oxygens O5 and O6 (green). Figure is adapted from [189]

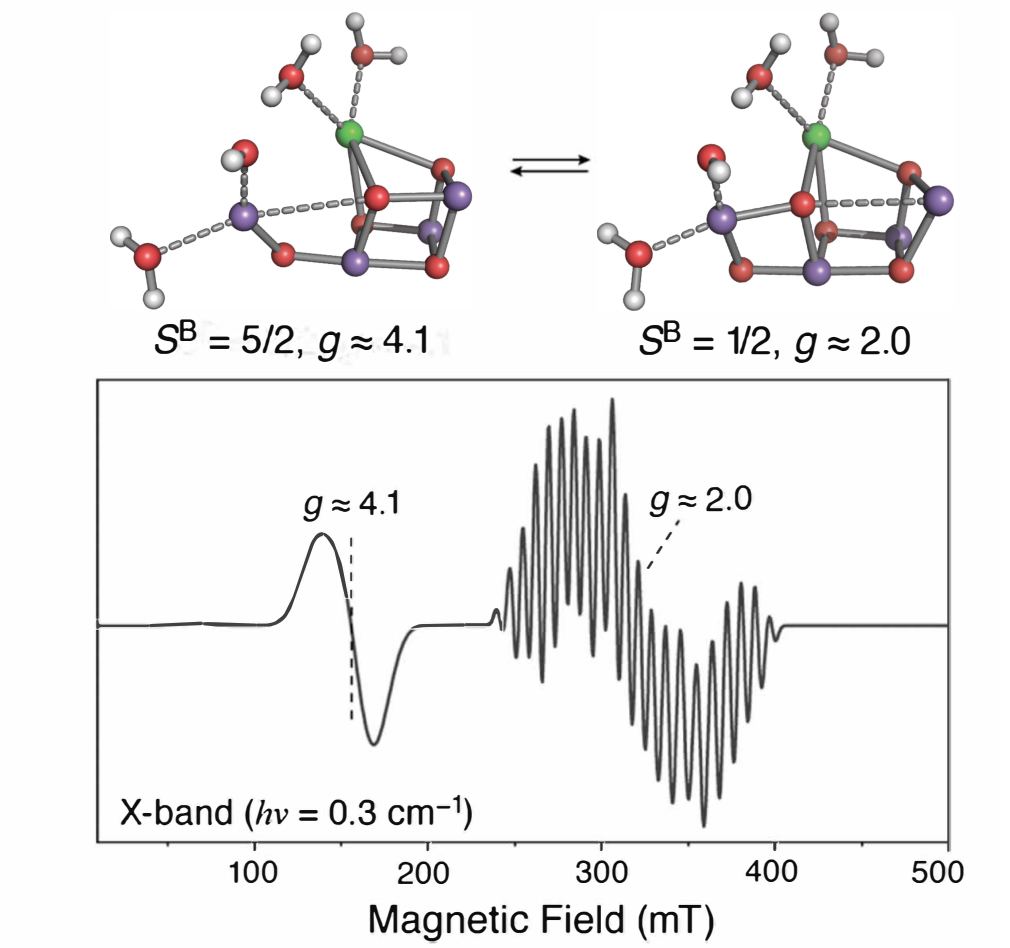

Figure 1.7. Optimized DFT structures of the Mn_4O_5Ca cluster in the S2 state. Model A (right) exhibits a spin $S = 1/2$ effective ground state (EPR "multiline" signal at $g = 2$), and Model B (left) a $S = 5/2$ ground state (EPR signal at $g = 4.1$). Manganese ions are indicated in purple, calcium in green, oxygen in red and hydrogen in white. From ref. [266]

antiferromagnetic or ferromagnetic exchange interactions between the Mn ions leading to either a low-spin state, minimizing the number of unpaired electrons, or a high-spin state, maximizing the number of unpaired electrons. The studies of the groups of Ono and Kusunoki on oriented PSII membranes and theoretical investigations [180, 181] and subsequent advanced EPR studies from the Britt (UC Davis) [50, 49, 275] and Lubitz (MPI Mülheim) laboratories [81, 191, 192, 207, 206, 334] further constrained all four ^{55}Mn hyperfine tensors in the S_2 state and allowed the spin coupling in the tetranuclear manganese cluster to be probed. These data together with results collected on the S_0 state, which also resolves a multiline signal [3, 191, 192, 205, 222], and density functional theory calculations allowed the local oxidation states and set of coupling pathways to be determined [7, 186, 188, 189, 265, 267]. The oxidation state assignment for the S_2 state, which comes from this analysis is Mn4(III, IV, IV, IV). According to the low oxidation scheme S_0 includes a MnII [183, 263, 344], but this was excluded by the ^{55}Mn ENDOR experiments and analysis of the S_0 state [191, 192, 205]. The reader interested in details on how the electronic configuration of a polynuclear Mn cluster, especially the Mn_4CaO_5, can be probed by EPR spectroscopy and double resonance techniques in relation with calculations of magnetic properties by quantum mechanical methods is referred to the following review [206]. Additional support for the high oxidation state scheme has come from the detection of ^{14}N ($I = 1$), ^{2}H ($I = 1$) and ^{13}C ($I = 1/2$) hyperfine couplings of the S_2 state using ESEEM and ENDOR techniques performed by the group of R. D. Britt [48, 217, 280, 261, 328, 332]; see also [205, 280]. X-ray spectroscopies also agree with this assignment [57, 394, 392]. These studies rule out the alternative lower oxidation state models for the manganese cluster [183, 263] that are, however, still discussed in the literature [59, 344].

In the S_2 state, in addition to the low-spin $S_{eff} = 1/2$ form showing the characteristic multiline signal around $g \approx 2$, the cluster can also be found in a high-spin $S_{eff} = 5/2$ state under certain conditions. This is evident from an EPR signal around $g = 4.1$ (see Fig. 1.7), which has been observed earlier by several research groups [39, 193, 133]. Pantazis et al. [266] could show computationally that the two electronic structures are a direct consequence of two different spatial conformations of the manganese cluster, namely a "closed cubane" ($S_{eff} = 5/2$) and an "open cubane" ($S_{eff} = 1/2$) form, which have almost the same energy

It is important to note the concept of the Jahn-Teller distortion considering its role in the interpretation of OEC structures. The Jahn-Teller (JT) effect is formally described as the geometrical distortion of molecules and ions that are associated with certain electron configurations. When a molecule exhibits a spatially degenerate electronic ground state, it will undergo a geometrical distortion that removes this degeneracy to lower the overall energy of the species [153]. Various octahedral complexes with nine d electrons, low-spin d^7 and high-spin d^4 metal electrons, can show the JT effect, but the distortion is more pronounced when the degeneracy occurs in the e_g orbital group, as these orbitals point directly toward the ligands.

In OEC, the terminal Mn1 and Mn4 ions have clearly defined Jahn-Teller elongation axes, the structural signatures of high-spin d^4 Mn(III) ions with occupation of the metal-ligand σ-antibonding d_z^2 orbital. This feature enabled Suga et al. [335] to assign the two terminal Mn ions as Mn(III) and the orientation of JT axes as almost collinear along W1-Mn1-O5-Mn4-D342.

Computational results [166, 319], as well as large-scale QM/MM simulations

shoji2015adv, shoji2016qmmm, have elucidated that the JT effects of Mn1 and Mn4 ions play important roles for subtle structural deformations of the $CaMn_4O_5$ cluster in OEC of PSII, particularly the Mn4-O5 and Mn1-O5 distances revealed by the high-resolution XRD, XFEL and EXAFS experiments. When the O5 site is oxygen dianion (O^{2-}), the JT elongation axis became perpendicular to the Mn4-O5-Mn1 bond, regarding O^{2-} as a strong ligand field for Mn4. Hence, for the protonated dianion case JT axis was almost parallel to W1-Mn1-O5-Mn4 bond. Thus, the Mn-O bond lengths are variable, depending on the JT effect on Mn(III) ion.

Modifications of the Mn_4O_5Ca cluster, such as exchange of Ca^{2+} with Sr^{2+} [40, 38, 67, 81, 184, 360], its complete removal [42, 207, 333, 362] and the binding of small molecules [23, 280, 261, 262, 294, 334], provided further insight into the conformation and number of ligands of individual Mn ions (coordination geometry) and substrate access in the S_2 state. Upon Ca depletion water oxidation functionality is lost, but the S_2 state (S_2') is still formed [42, 43]. Interestingly, the EPR and ^{55}Mn ENDOR data of S_2' show that the calcium has no substantial effect on the magnetic parameters of the S_2 state; this ion is thus not crucial for maintaining the electronic structure of the tetranuclear Mn cluster [207]. Instead, it might serve as stage for the delivery of water molecules to the reaction site [236, 312, 148], affect the function of Y_Z, [223, 293] and introduce some structural flexibility allowing the cofactor to toggle between the different motifs of the open and closed cubane structures (see Fig. 1.7). The interactions of small molecules which mimic the substrate water (methanol, ammonia) also support this potential role for Ca^{2+}. These molecules associate with the Ca^{2+} and D61 water channels that lead to the Mn_4O_xCa cofactor [217, 280, 262, 294, 308]. In addition, both of these molecules reduce turnover efficiency; these results implicate that at least one (or possibly both) of these channels are involved in substrate delivery. The EPR measurements have been extended to the S_3 state. These results are of particular importance since this is the last metastable state prior to O–O bond formation and O_2 release. The EPR signal of the S_3 state has first been reported to originate from a ground state with an integer spin of $S_{eff} = 3$ by the groups of Petrouleas [302] and Boussac [41]. Recent pulse high field (W-band) EPR experiments by Cox et al. corroborated this assignment and directly proved that the effective spin state is indeed $S_{eff} = 3$ by measuring the Rabi oscillations via a spin nutation experiment [80]. In addition ^{55}Mn ELDOR-detected-NMR (EDNMR) experiments at W-band could successfully be performed showing that in the S_3 state all Mn ions are in the MnIV state Mn4 (IV,IV,IV,IV) and octahedrally coordinated. The results also show that a sixth ligand is binding to the open coordination site of the MnIII present in the S_2 state when it is oxidized. This ligand is most probably the second substrate water molecule which also loses a proton in the $S_2 \rightarrow S_3$ transition. The magnetic resonance experiments described above together with theoretical calculations allowed a reliable characterization of the S_0, S_2 and S_3 states with respect to oxidation and spin states of individual ions and their spin coupling in the tetranuclear Mn cluster summarized by Krewald et al. [188, 189]. Together with information about binding of the two substrate water molecules described below spatial models of the S states could be obtained that form the basis for developing a catalytic mechanism for the OEC (Fig. 1.6).

EPR spectroscopy proved to be an extremely powerful tool for investigations on

PSII and the OEC, as the latter exhibits paramagnetic character that is retained throughout the Kok cycle. Therefore, all identifiable S-states exhibit EPR signals, with the S_0 and S_2 state providing half-integer ground state spin (S=1/2) that is readily accessible by standard continuous-wave (CW) and pulse EPR techniques. A summary of the signals and EPR parameters obtained for the different S-states can be found elsewhere [132]. Here, the focus is on the S_2 state, which has received the most attention of all states of the Kok cycle in EPR studies.

1.2.4 FTIR spectroscopy attempts to unveil the mechanism of water splitting

Infrared (IR) spectroscopy, particularly light-induced Fourier transform infrared (FTIR) difference spectroscopy [216, 361, 33], has been used extensively to study the mechanism of photosynthetic water oxidation [65, 248, 246, 89, 63, 91, 247]. Flash-induced FTIR difference spectra have been measured upon individual transitions in the S-state cycle ($S_1 \rightarrow S_2$, $S_2 \rightarrow S_3$, $S_3 \rightarrow S_0$ and $S_0 \rightarrow S_1$) [254, 142], and data regarding the structures and reactions of the proteins and water molecules during water oxidation have been obtained.

The following chapter is an attempt to review the current knowledge on PSII IR difference spectra in the region between 450 and 1800 cm^{-1}. Much of the information stems from the great work of the above mentioned authors.

The width of IR bands of amino acids in solution are reported to be between 8 cm^{-1} (for the tyrosine ring vibration) and 30–50 cm^{-1} (form most other side chains) (full width at half maximum, [355]).

Mid-frequencies region

An overview of the approximate positions of the vibration of different chemical groups can be found in figure 1.8. This scheme only shows the group frequencies' approximate positions. Their actual position in a protein spectrum depends on their close environment. Some examples will be given below.

Protein backbone vibration The backbone vibration is classified into numerous groups. Relevant to this thesis are the amide I and II vibrations. Amide I includes mainly the $\nu(C=O)$ and weakly the CN out-of-phase stretching, the NH in-plane bending as well as the CCN deformation of the peptide bond. It is very sensitive to the secondary structure. The amide II vibrations consists mainly of the out of phase combination of the CN stretching and the NH in plane bending. It is not straightforward assignable to the secondary structure ([22]).

1250 to 1800 cm^{-1}: Carboxylates When they are protonated, the $\nu(CO)$ absorbs between 1710 and 1760 cm^{-1}, a region that is free of other aminoacid vibrations ([21]). These vibration are very sensitive to H-bonding (detailed study by [341]). The (COO^-) vibration is split into an asymmetric and a symmetric band, which are found around 1570 and 1400 cm^{-1}, respectively ([21]). Upon ligation of a metal ion, the band position may shift considerably (for ν_s down to 1270 cm^{-1} [176]). The wavenumber difference between ν_{as} and ν_s was found by: $\Delta\nu = \nu_{\nu(COO^-)_{as}} - \nu_{\nu(COO^-)_s} \approx 200$ cm^{-1}: unidentate coordination, ≈ 160 cm^{-1}: ionic, ≈ 160 cm^{-1}: bridging bidentate structure, ≈ 100 cm^{-1}: chelating bidentate

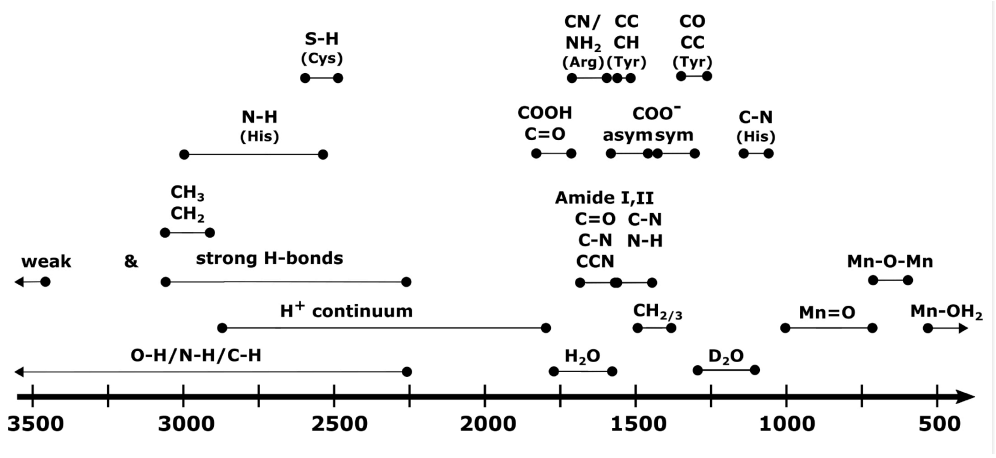

Figure 1.8. Position of chemical group frequencies relevant to PSII. Only the most prominent vibrations are shown. The positions are taken from various literature presented in this chapter.

coordination [317]. However, in PSII studies many ligands of Mn atoms, that undergo oxidation, are silent. [325] found, that the charge of the cluster is strongly delocalized and no straightforward correlation of the ligating carboxylates and the oxidation state of the cluster can be drawn, unless the carboxylate is coordinated along the Jahn-Teller axis.

Proton continuum band A delocalized proton gives rise to a broad continuum band and can be found in many proteins, also in PSII. It can be found in between 1000-3000 cm^{-1} ([22]) and depends on the number of sharing molecules and their 3d conformation ([82]).

Other amino acids The guanidyl group of arginines absorbs at 1630-1690 cm^{-1} in their protonated state and at 1550-1600 cm^{-1} in their deprotonated state [316]). The IR modes of lysine are very weak with two modes around 1625 and 1525 cm^{-1} ([21]). The ν(C = O) modes of asparagine and glutamine are located around 1680 cm^{-1} but depend on the H-bonding. The amino groups absorb weakly around 1610 cm^{-1} ([21]). The absorption modes of serine and threonine are located between 1000 and 1420 cm^{-1}. Their ν(CO) contributes mainly around 1075 to 1150 cm^{-1} ([21]).

Lipids The $\nu_{s/as}(CH_2)$ of lipids absorbs around 2900 cm^{-1}. Methyl vibration absorb in between 1300 and 1500 cm^{-1}. Carbonyl stretching modes are expected from 1720 to 1750 cm^{-1}. The phosphate $\nu_{as}(PO^{2-})$ modes appear around 1220 to 1240 cm^{-1} and the $\nu_s(PO^{2-})$ modes around 1080 and 1090 cm^{-1} and both are sensitive to H-bonding and cation bonding. Lipids possessing carboxyl groups absorb additionally around 1600 to 1650 cm^{-1} [342].

[**First shell ligands**] Mid-frequency S_2-minus-S_1 FTIR difference spectra of PSII core complexes free of contributions from the quinone electron acceptors were first reported between 1992 and 1999 [251, 253, 252, 249, 64, 250]. The first mid-frequency S_3-minus-S_2 FTIR difference spectrum was reported in 2000 [67]. The first sets of complete mid-frequency S_{n+1}-minus-S_n FTIR difference spectra were reported in two back-to-back publications in 2001 [254, 142]. Numerous signals are found in the mid-frequency region of 1800–1000 cm^{-1}, where protein bands mainly appear

Ligand	Mutation/ Isotope labelling	Assignment	Reference
A344	L-[(1-^{13}C]-Ala	1355 (S1) $\nu_{asym}(COO^-)$ in ^{12}C 1339/1320 (S2) $\nu_{aym}(COO^-)$ in ^{12}C 1339/1320 (S1) $\nu_{asym}(COO^-)$ in ^{13}C 1302 (S2) $\nu_{sym}(COO^-)$ in ^{13}C	[66, 176]
E354	E354Q	1525 (S1) $\nu_{asym}(COO^-)$ in WT 1394 (S1) $\nu_{sym}(COO^-)$ in WT 1502 (S2) $\nu_{asym}(COO^-)$ in mutant 1431 (S2) $\nu_{sym}(COO^-)$ in mutant	[317]
	E354Q with ^{15}N	1502 (S2) amide II	[314]
E189	E189Q	1417 (S1); 1435 (S2) in WT 1421 (S1); 1441 (S2) in mutant	[176, 329]
	E189R	S1-S0: no significant changes	[313]
E333	E333Q	S1-S0 : no significant changes	[313]
D342	D342N	S2-S1: no significant changes	[331]
D170	D170H	S1-S0: no significant changes	[65, 92]

Table 1.1. Overview of FTIR studies by side-directed mutagenesis and isotope labelling in the region of carboxylate stretching frequencies of OEC first-shell ligands

[83, 84], which is indicative of drastic protein movements during water oxidation.

Global isotope labelling with ^{13}C or ^{15}N lead to the assignment of the feature between 1700 - 1600 cm^{-1} to amide I modes. Significant bands also appear in the region of 1600–1500 cm^{-1}, where the amide II and asymmetric COO^- stretching bands overlap [83, 84]. Essentially, all of the prominent bands in the 1450–1300 cm^{-1} region arise from the symmetric COO^- stretching vibrations of carboxylate groups coupled to the Mn_4CaO_5 cluster [83, 84, 149].

[A344] Spectra were analyzed using site-directed mutants of putative carboxylate ligands and/or isotopic substitutions. Two independent FTIR studies showed that the incorporation of L-[1-^{13}C]alanine altered the wild-type S_2-minus-S_1 mid-frequency FTIR difference spectrum in the symmetric carboxylate stretching region [66, 176]. The ^{12}C-minus-^{13}C double difference spectrum of this region showed that the alterations represent the ^{13}C-induced shift of a single vibrational mode. In the S_1 state, this mode appears at ∼1355 cm^{-1} and is shifted by ^{13}C to either ∼1339 or ∼1320 cm^{-1}. In the S_2 state, this mode appears at either ∼1339 or ∼1320 cm^{-1} and is shifted by ^{13}C to 1302 cm^{-1}. The reason that the $\nu_{sym}(COO^-)$ mode of D1-A344 downshifts during the S_1 to S_2 transition is not known. Perhaps the reason is related to one conclusion of a polarized attenuated total reflection FTIR study [147], that D1-A344 may significantly change its orientation during the S_1 to S_2 transition.

[E354] The S_2-minus-S_1 FTIR difference spectrum of CP43–E354Q PSII core complexes shows alterations throughout the amide II, $\nu_{asym}(COO^-)$ and $\nu_{sym}(COO^-)$ regions [330, 317, 314]. These data show that the CP43–E354Q mutation perturbs multiple carboxylate groups in the vicinity of the Mn_4CaO_5 cluster. In one study

[317], negative features at 1525 cm^{-1} and 1394 cm^{-1} in the S_2-minus-S_1 FTIR difference spectrum of wild-type PSII were assigned to the $\nu_{asym}(COO^-)$ and $\nu_{sym}(COO^-)$ modes of CP43–E354 in the S_1 state, respectively, and the positive features at 1502 cm^{-1} and 1431 cm^{-1} were assigned to the $\nu_{asym}(COO^-)$ and $\nu_{sym}(COO^-)$ modes of CP43–E354 in the S_2 state, respectively [317]. Based on this assignment the authors concluded that CP43-E354 changes its coordination mode from bridging bidentate in S_1 state to chelating in S_2 state. However, in another study [314], the positive feature near 1502 cm^{-1} was assigned to an amide II mode on the basis of its downshift by 14–15 cm^{-1} after global labeling with ^{15}N (although the presence of the $\nu_{asym}(COO^-)$ mode at the same frequency could not be excluded because of the feature's breadth). In agreement with [317], this study assigned a negative feature at 1524 cm−1 to the $\nu_{asym}(COO^-)$ mode of CP43–E354 in the S_1 state and concluded that CP43–E354 serves a as a bridging ligand between two Mn ions in the S_1 state [314]. However, this study was unable to confirm that the coordination mode of CP43–E354 changes during the S1 to S2 transition because the $\nu_{sym}(COO^-)$ mode of CP43-354 could not be identified unambiguously.

[D170, E189, E333, D342] The mutations D1-D170H [65, 92], D1-E189Q [176, 329], D1-E189R [313], D1-E333Q [313], and D1-D342N [331] produced no significant changes in any of the S_{n+1}-minus-S_n FTIR difference spectra. The changes are not significant in the sense that they are not greater than the changes caused by mutations of the residues located far from the Mn_4CaO_5 cluster (e.g. D2-H189Q, near Y_D) or by differences in handling wild-type samples [329]. Moreover, none of these mutations produced considerable changes in the amide I and amide II regions of the spectra. Such insensitivity of the four out of six OEC's closest carboxylate ligands is totally unexpected. The simplest explanation for this kind of behaviour could be the fact that the positive charge on the Mn_4CaO_5 cluster during S_1 to S_2 transition is highly delocalized at ambient temperatures. Furthermore, mid-frequency S_{n+1}-minus-S_n FTIR difference spectra may correspond to residues located 5-11 Å from the nearest Mn ion and though to participate in proton egress pathways since mutations of these side chains cause the greatest changes [311, 312, 90].

Low-frequencies region

The region between 350 and 650 cm^{-1} is related to the vibrations of inorganic core and its metal-ligand bonds. The first set of complete S_{n+1}-minus-S_n difference spectra in this region appeared in 2005 [176]. As for the mid-frequency region spectra were analyzed by site-directed mutagenesis and/or isotopic substitutions. Among these, the bands at 606/625 cm^{-1} in S_2/S_1 state, respectively, were assigned to a Mn-O-Mn cluster mode in a multiply bridged structure that might include additional oxo or carboxylate bridges [67, 65, 176]. This assignment was based on the facts that bands downshifted in samples exchanged into $H_2^{18}O$ but were unaffected by ^{44}Ca labeling. Global labeling with ^{13}C and/or ^{15}N [174] caused essential shifts of the bands in this region, including the 606 cm^{-1}, and were proposed to include Mn-COO^- bending modes or Mn-nitrogen-containing groups modes. A negative band at 577 cm^{-1} was shifted by neither ^{13}C nor ^{15}N (nor ^{18}O [67]) and was attributed a skeletal vibration of the Mn_4CaO_5 cluster or to a Mn-O vibrational mode involving a non-^{18}O-exchangeable oxygen atom [174]. The 606 cm^{-1} band in the S_2 state

appeared to change sign and intensity during the S state cycle [176], implying S state-dependent changes in the core structure of the Mn_4CaO_5 cluster.

Other prominent bands between 638 and 594 cm^{-1} appeared to change the sign and intensity during the S state cycle [176], implying S state-dependent changes in the core structure of the Mn_4CaO_5 cluster. Some of these were also assigned to Mn_4CaO_5 cluster modes on the basis of their sensitivity to $H_2^{18}O$ substitution and insensitivity to D_2O substitution [176]. Other low-frequency bands were sensitive to D_2O substitution, but were insensitive to $H_2^{18}O$ substitution [176]. These were assigned to modes from amino acid side chains and polypeptide backbones associated with exchangeable hydrogen in hydrophilic environments. The 606 cm^{-1} band in the S_2 state shifts to ∼618 cm^{-1} when Ca is replaced with Sr [67, 65, 176], shifts to ∼613 cm^{-1} in the mutants D1-D170H [62] and D1-A344G [224], and shifts to ∼623 cm^{-1} in the mutant D1-E189Q [173]. These observations show that D1-D170 and D1-E189 are coupled structurally to the Mn_4CaO_5 cluster, despite the absence of changes in the mid-frequency region produced by the mutations D1-D170H [65, 92] and D1-E189Q [176, 329].

1.3 Water splitting in artificial photosynthetic systems

It is vital to develop technology which can derive energy from renewable resources. This idea was presented as far back as in 1912 by Giacomo Ciamician [70], when he stated:"Solar radiation may be used for industrial purposes ... Photochemistry will artificially put solar energy to practical uses. To do this it would be sufficient to be able to imitate the assimilating processes of plants".

Nowadays Ciamician's idea for production of 'solar fuel' from inexpensive and abundant material such as water that could be split into oxygen and hydrogen is highly attractive. Often hydrogen is called fuel of the future since its combustion generates pure product as water. A promising way for the light driven water splitting in newly made device would be to mimic the molecular and supramolecular organization of the natural photosynthetic system, i.e. "artificial photosynthesis". Today the concept of solar energy conversion as alternative to fossil fuels is an important field of research and artificial photosynthesis is considered as a highly promising scientific direction ([177, 211, 86, 245, 372]).

Figure 1.9 gives a basic overview of artificial photosynthesis. Artificial photosynthesis includes both oxidation and reduction reactions in which water molecules are directly involved (Equation 1.2). Similar to natural photosynthesis, the reaction starts with absorption of light by photoactive species (A and D), which reach their excited states (A^* and D^*). A^* act as a strong oxidant (by releasing an electron) in its excited state and D^* yields a reduced state (by capturing an electron). Generated electron and electron holes can be transferred to water oxidizing catalyst (Cat_{ox}) and to a catalyst forming hydrogen by proton reduction (Cat_{red}), respectively. Water oxidation and proton reduction reactions are linked by a relay molecule R that transfers a charge between the PSII-like and the PSI/hydrogenase-like units (Figure 1.9).

$$2H_2O \rightarrow O_2 + 4H^+ + 4e^- 4H^+ + 4e^- \rightarrow 2H_2 \tag{1.2}$$

Thus, artificial photosynthesis (AP) has the same principle of electron flow as

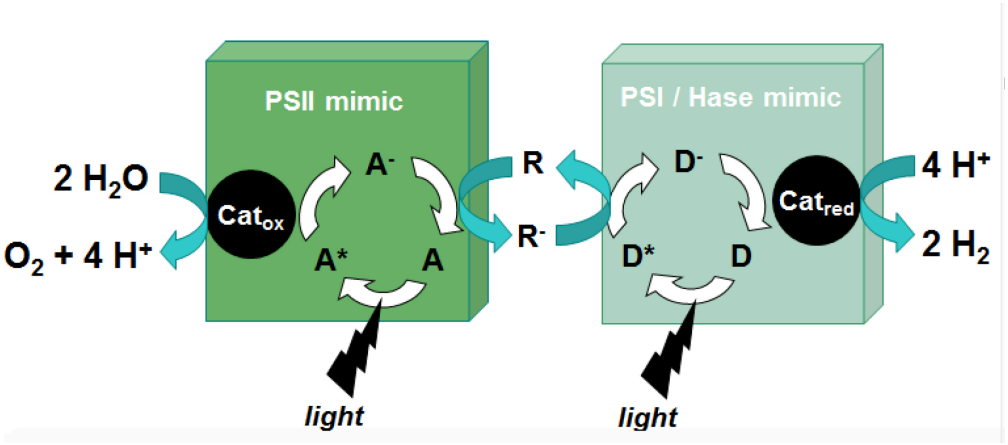

Figure 1.9. The scheme of Artificial Photosynthesis device

natural photosynthesis: The reduction equivalents obtained by PSII during water oxidation are transferred through the redox carriers to PSI and are then used to produce "natural fuel" – NADPH.

1.3.1 Concept of artificial photosynthetic devices

Light absorption results in the formation of high-energy charge separated states in both molecular donor-acceptor systems and semiconductor particles. Semiconductors are able to excite electrons into higher energy levels and overcome the band gap. Today there are two approaches for the light driving water splitting by semiconductor partials: (i) water splitting by single semiconductor partial (one step photo-excitation system), where catalyst partialy acts as Cat_{ox} and Cat_{red} without need of electron retransfer ([214]) and (ii) two different types of semiconductors (two step photo excitation system) for water splitting and proton reduction, respectively ([190]).

Nowadays, commercially available electrolyzers typically have efficiencies of up to 80% [87]. However, major drawbacks of current electrocatalytic water-splitting devices are the expensive metals (Ir and Ru) as well as their complex constructions. Hydrogen production by water electrolysis is expensive today and only used to generate hydrogen of high purity [87]. In order to make electrolyzes more affordable and attractive for alternative energy production, one needs to find more cost-effective approaches. One way to optimize electrolyzers is to couple them to photovoltaic cells (PVs) ([272, 338]). Here sunlight is converted in to electric energy by a photovoltaic cell to provide the required redox potential for water oxidation and proton reduction.

The artificial leaf is solar water-splitting cell including earth-abundant elements that operate in near-neutral pH conditions, both with and without connecting wires [245]. The cell is based on triple junction, amorphous silicon photovoltaic interfaced to Co catalyst (Cat_{ox} as oxygen evolving catalyst), and $NiMoZn$ catalyst (Cat_{red} as hydrogen evolving catalyst). Efficiency of water splitting reaction is 4.7% for a wired configuration and 2.5% for a wireless configuration.

The light harvesting efficiency can be increased by immobilizing molecular dyes at the semiconductor's surface. When the dye is excited by solar light, it can inject one electron into the conduction band of the semiconductor, generates a charge

at the semiconductor-dye interface. In dye-sensitized solar cells, dye-sensitized semiconductor particles are immobilized at a conducting surface like indium doped tin oxide or fluorine doped tin oxide as anodes [134].

Being the primary light-harvesting pigments in photosynthesis, porphyrins have great potential in view of developing devices for solar energy conversion, due to their strong visible absorbance (namely a strong Soret band centered between 400-500 nm and a moderate Q band in the 550-650 nm spectral region) and synthetic tunability. Furthermore, the photophysical and electrochemical properties of porphyrins can be tuned upon metalation or the introduction of tailored substituents [232, 144, 384], making them excellent candidates for dye-sensitized regenerative solar cells [388, 378], as well as for water splitting (when combined with suitable catalysts) [225, 218]. In the same way as chlorophylls in plants, a monolayer of porphyrin dye sensitized solar cells (DSSC) absorbs the incident light and generates positively and negatively charged carriers. The photoconversion of light energy into electric energy is based on the competition between the charge separation process and the deactivation processes occurring in the porphyrin dye molecules because of the (non)-radiative deactivation of the dye excited states.

The studies preformed up to 2010, showed that the energy conversion efficiency for DSSC based on porphyrinic dyes was lower than those based on ruthenium complexes. This situation was changed by the use of organic dyes with high extinction coefficients such as push-pull Zn porphyrins or of co-sensitized organic dyes and the replace of I^-/I_3^- with cobalt complexes as redox mediators [169, 114], increased the efficiencies over 13% [219, 113]. New concepts in hole transport materials associated to environment and cost friendly systems paved the way to more stable full solid-state devices to provide efficiencies over 20% that is a must for deployment to commercialization [299].

Earth-abundant transition-metal-based water oxidation catalysts (WOC) have been considered as promising candidates. Nocera and coworkers reported that a perfluorinated "hangman" porphyrin complex could electrochemically catalyze water oxidation and the hangman carboxylic group was essential in that it functioned as a secondary coordination site [96]. Subsequently, many different Co-based complexes, e.g. Co porphyrins and Co salophenes, have been studied [197, 237, 146, 198, 60, 282, 97]. Several Ni complexes based on well-known non-heme-iron ligands have been synthesized and used to assess the performance of catalytic water oxidation [366, 212, 160, 365]. Because of the fewer redox states of Ni ions, development of Ni-based WOCs with low overpotentials remains challenging. Fe-based complexes are considered as ideal candidates for WOC as the metal is the most abundant, non-toxic and has a rich redox chemistry. Studies of several classes of Fe complexes [105, 73, 371, 234, 268, 204, 74, 259, 110] have suggested that binuclear Fe-based complexes can generate more efficient molecular catalysts for water oxidation.

Many Mn-based catalysts have been explored for oxygen evolution [167, 235, 16, 119], starting from the first dimeric manganese triphenylporphyrin complexes linked by an *o*-phenylene bridge [239] with a turnover number (TON) of 9.2 and turnover frequency (TOF) 0.0018 s^{-1} and other complexes with improved catalytic properties, as the complex which can catalyze water oxidation without involving oxygen transfer reagents by Akermark and coworkers [168] by using $[Ru/bpy)_3](PF_6)_3$ oxidant with a TON of 25 and an initial TOF of 0.027 s^{-1}. The studies on mimicking the key

structural motif of the Mn_4CaO_5 cluster are discussed in the following subsection.

1.3.2 Synthetic OEC Model Coordination Complexes

Water oxidation to molecular oxygen is a four-electron four-proton reaction that requires an overall redox potential of 1.23. To be capable to drive this reaction by visible light one needs to avoid high energy species such $HO^{\bullet}$ that would be formed by a one-electron oxidation of water. As such, transitions metals, or clusters thereof, that are able to support multi-electron reduction steps are most suitable as water oxidation catalysts. It is also highly important that the catalysts operate with low overpotentials. A comparison of almost 20 different transition metals oxides by Harriman et.al. [137] revealed that IrO_2, Co_3O_4, RuO_2, Mn_2O_3 function most efficiently as O_2-evolving catalyst. Up to now situation has not changed very much and the most successful catalysts for water oxidation are made from the above mentioned oxides [226, 165, 99, 78, 154, 233, 98]. Oxides of noble metals are the most efficient water oxidation catalysts reported so far. However, these oxides are no promising catalytic components for artificial photosynthetic devices for large scale solar fuel generation due to the low abundance and high costs of Ru and Ir.

Mn and Co are favored by many chemists for synthesis of "PSII like" artificial photosynthetic systems for water splitting since they are relatively abundant (especially Mn). Mn is found as free element in nature, for example at the ocean floor and the bottoms of many freshwater lakes, as well as in many minerals. Moreover, Mn has the ability to attain a large number of different oxidation states. Both are likely reasons why it was chosen by nature as active center for water splitting [12]. The structure of this center is in higher plants, algae, and in cyanobacteria. Artificial complexes that mimic the WOC, with multinuclear Mn connected through μ–oxo bridges were found to act as highly active water oxidation catalyst [47, 233, 372]. The metal centers of artificial Mn-complexes are cycling between MnIII and MnIV oxidation states during water oxidation process and that is why multinuclear species, at least 4 Mn, are required.

Both synthetic Co and Mn oxides are very promising candidates for large scale applications of artificial water oxidation chemistry, since they are abundant, inexpensive and non toxic catalysts. One condition for this is, however, that their activity (turnover number and turnover frequency) can be improved. More detailed information about synthetic OEC models can be found in following subsections.

Early models

Synthetic control over the coordination chemistry of manganese and its oxidation states has advanced significantly over the past few decades, allowing isolation of highly complex clusters. As structural understanding of the OEC has improved, increasingly accurate synthetic mimics have been prepared. These homo- and heterometallic manganese oxido complexes have been used to study the physical properties and structure–activity relationships of clusters relevant to the OEC.

Synthetic model complexes of the OEC can be useful spectroscopic benchmarks when studied in conjunction with the biological cluster, as the structure and oxidation states of these complexes can often be unambiguously identified. Reactions of

these complexes, including oxygen-atom transfer, water exchange, and cluster rearrangement, have been used to support key mechanistic proposals for how dioxygen is formed at the OEC. These model complexes have also demonstrated activity as artificial WOCs.

It is useful to keep the above mentioned evolution of structural ideas and models in mind when reviewing the efforts of synthetic chemists to create structural analogues of the OEC, because for a long time these efforts were inspired by models that eventually proved to be inaccurate or of only indirect relevance to the current detailed view of the OEC.

Targets for structural biomimetic chemistry:

- The stoichiometry of four manganese and one calcium ions.
- Incorporation of Ca^{2+} within an oxo-bridged metal framework.
- A Mn_3CaO_4 substructure that may or may not be present as a fully bonded unit in some of the S_i states depending on the Mn oxidation states.
- A fourth Mn ion ("dangling Mn") external to the above cuboidal unit, connected with it via oxo bridges.
- Almost exclusively carboxylate and water-derived ligands.
- In addition to the above structural features, a model should contain the physiologically relevant oxidation states of Mn ions (exclusively III and IV) and the ligand framework would ideally support access to multiple oxidation states.

All of the above structural features have important implications for the electronic structure of the cluster, its magnetic and spectroscopic properties, and ultimately for its catalytic function, although the latter cannot be meaningfully considered in isolation from the protein matrix of the OEC and the rest of the PSII machinery.

In the following section, selected examples of manganese oxide clusters will be discussed, with emphasis on tetramanganese complexes and heterometallic complexes as they are particularly relevant to the structure of the Natural Complex.

Monometallic complexes

Although the OEC contains four manganese centers, EPR studies of the S_2 state of the OEC showed a multiline signal at $g = 2$, as well as a broad signal at $g = 4.1$ [50]. The latter EPR signal was initially proposed to arise from a magnetically uncoupled MnIV center,[136] motivating studies of monomanganese(IV) complexes as simplified OEC models. These synthetic monomanganese(IV) complexes have provided important insights into the chemistry of high-valent manganese, particularly with respect to tuning the redox potentials of manganese. Figure 1.10 shows selected examples of monometallic complexes with MnIV centers. The syntheses of these different MnIV complexes permit comparison of ligand effects on the electrochemical properties of the compounds.

EPR and XAS measurements first determined that the OEC contains multiple manganese centers. The multiline g=2 EPR signal of the S_2 state arises from

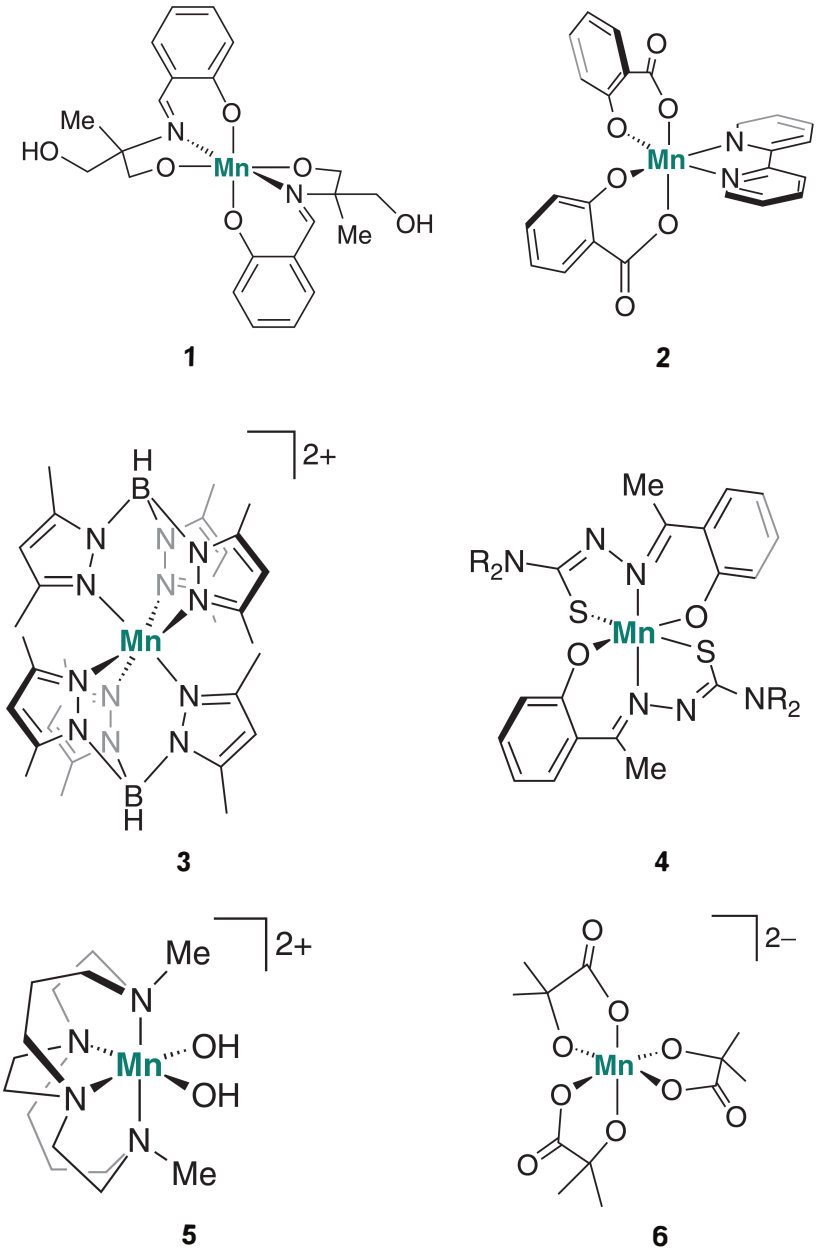

Figure 1.10. Selected examples of monometallic Mn(IV) compounds. From ref. [271, 55, 297, 389, 301]

coupled Mn ions, and short Mn–Mn distances (2.7 Å) consistent with di–μ–oxo–bridged dimanganese clusters as well as a longer Mn–Mn distance (3.3 Å) were measured by XAS [380, 303]. Following these spectroscopic measurements, synthetic multimanganese complexes have been used to model these Mn–Mn interactions [228, 229]. The mixed-valent dimanganese complex $[(bpy)_2MnIII(\mu\text{–}O)_2MnIV(bpy)_2]^{3+}$ (1.11a), shown in Figure 1.11, was one of the earliest such multimanganese compounds studied.[79] Compound (1.11a) has been extensively studied as a model of the OEC because its oxido-bridged Mn centers are magnetically coupled and display a hyperfine-coupled multiline EPR signal similar to that of the OEC S_2 multiline signal at g=2. The 2.7 Å Mn–Mn distance of (1.11a) also matches the short Mn–Mn distance of the OEC [228].

To account for the longer 3.3 Å Mn–Mn distance of the OEC, a "dimer-of-dimers" structure was proposed, in which two dimanganese di(μ–oxo) complexes are bridged by a fifth oxido ligand (Figure 1.11) [382]. A polypyridyl supported tetrametallic manganese complex was prepared as a model of such a structure (1.11c),[56] and other complexes with dimer-of-dimers structures were also isolated [228]. A dimer-of-dimers structure of the OEC was later ruled out as a possibility based on EPR studies that suggested a [3+1] arrangement of the manganese centers, however [274].

Synthetic tetramanganese complexes display considerable structural diversity and have been used to demonstrate the accessibility of several previously proposed tetramanganese structures of the OEC prior to the publication of the high-resolution single-crystal XRD structure [274]. One such example is the "double-pivot"mechanism proposed by Christou and coworkers in which a $[Mn_4O_4]$ cubane structure releases O_2 to form a [Mn4O2] "butterfly" complex [357]. This mechanism was later ruled out for reasons discussed earlier.

Figure 1.12 shows examples of tetramanganese complexes studied as models to support these early mechanistic proposals. A $[Mn_4O_3Cl]$ partial cubane complex supported by bridging acetates and terminal pyridine and chloride ligands (1.12a) was the earliest prepared example of a synthetic tetramanganese cubane structure,[201] although other related $[Mn_4O_4]$ cubane clusters were later isolated [229]. "Butterfly" structures as models of the more open $[Mn_4O_2]$ intermediates of the "double-pivot" mechanism were also isolated (1.12b) [357].

Another mechanism has been proposed in which tetramanganese cubane structures rearranged to form adamantane-like clusters [229, 51]. Wieghardt and coworkers synthesized the first $MnIV_4$ complex, a $(Mn_4O_6)^{4+}$ adamantane stabilized by three chelating 1,4,7-triazacyclononane ligands (Figure 1.13a) [150]. With this precedent, the adamantane/cubane mechanistic proposal for the OEC invoked access to such a high oxidation state cluster.[187] Each MnIV displays a pseudo-octahedral coordination environment with three μ_2–oxido and three terminal N donors. Armstrong and coworkers further studied the Mn_4O_6 adamantane core structure, evaluating the effect of altering the chelating N_3 ligand on the basicity of the μ_2–oxido moiety and on the pH dependent reduction potential [294]. An all–μ–oxo bridged $Mn(III)_2Mn(IV)_2$ cubane complex was reported by Dismukes and co-workers (Fig. 1.13b) [300]. An exciting feature of the Dismukes cubane is that it can undergo photo-rearrangement to yield O_2 and a diarylphosphinate ligand and ultimately decays to a butterfly-shaped product. The idea of a reversible cubane/butterfly rearrangement was actually one of the early proposed mechanisms for the catalytic cycle of the OEC and the

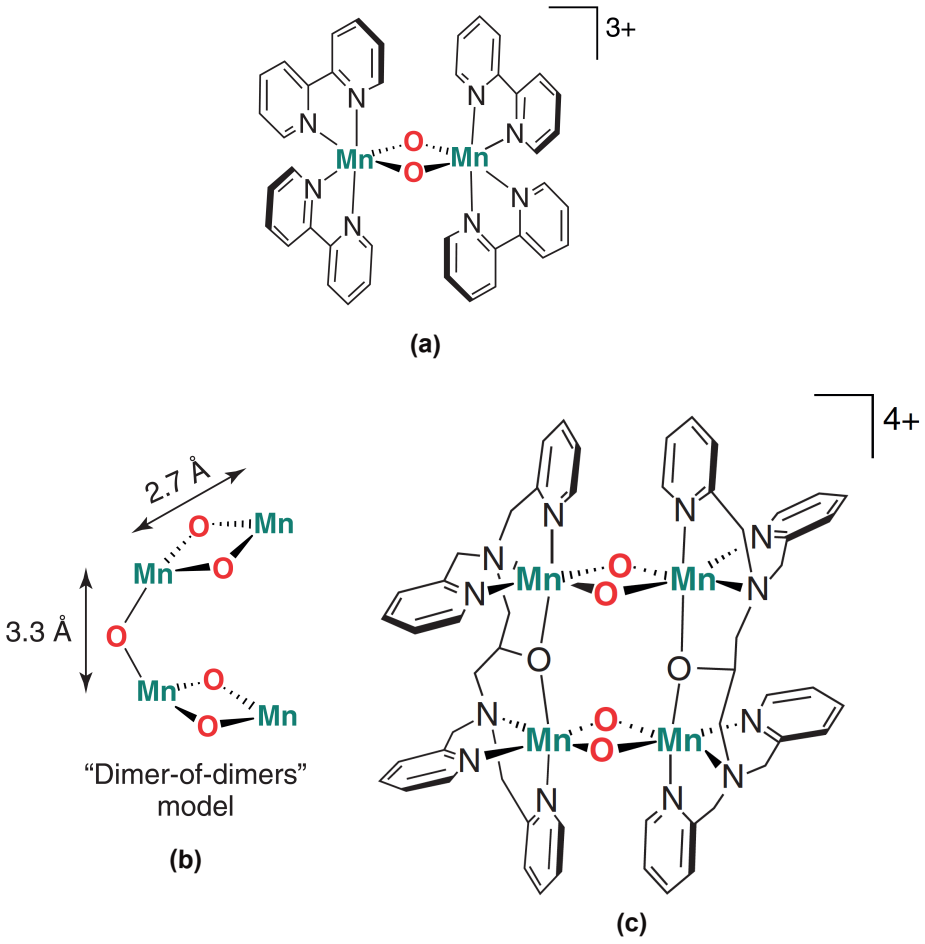

Figure 1.11. Drawings of [(bpy)2MnIIIO2MnIV(bpy)2]3+ (a), the proposed "dimer-of-dimers" structure of the OEC (b), and a "dimer-of-dimer" compound. From ref. [382, 79, 56]

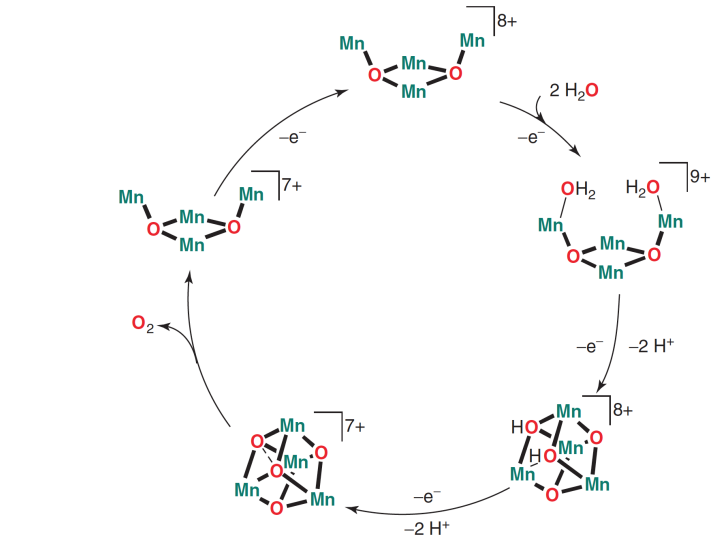

Diagram of "double-pivot mechanism"

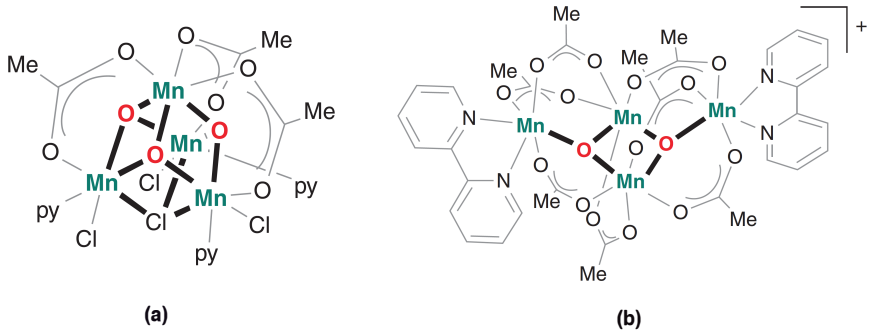

(a) (b)

Figure 1.12. Synthetic tetramanganese models of proposed OEC intermediates in the "double-pivot" mechanism. From ref. [357, 201]

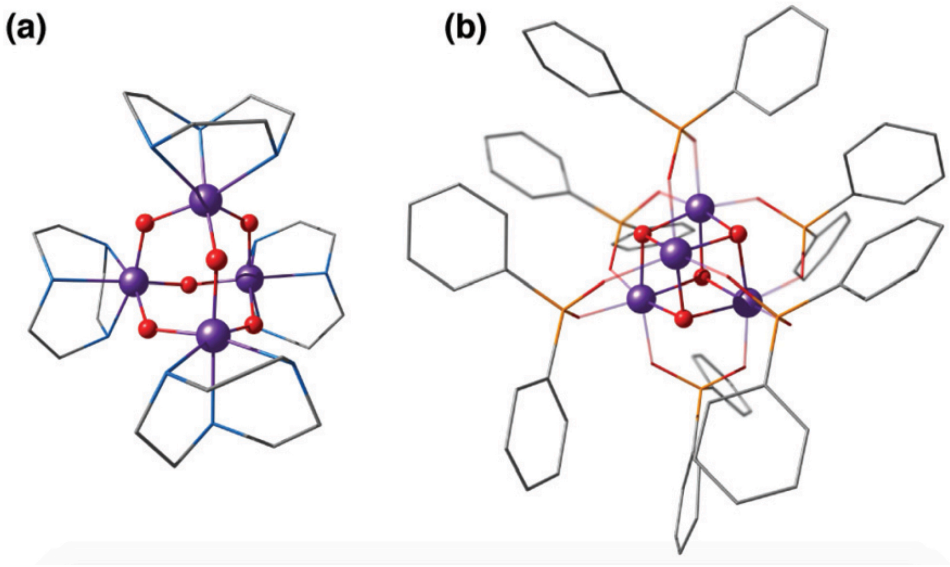

Figure 1.13. Synthetic tetramanganese models of proposed OEC intermediates with adamantane-like structure. From ref. [229, 51]

butterfly-shaped structure was one of the suggested structural models for the lower S_i states [356, 357].

In a different approach from the self-assembly methods discussed earlier, Agapie and coworkers used a multinucleating pseudo-$C3$-symmetric hexapyridyl tri-alkoxy-1,3,5-triarylbenzene ligand framework ($L3^-$) to support a series of related multi-manganese clusters [347]. Unlike the previously described self-assembled manganese complexes, these compounds are site-differentiated; the apical metal center is different from the three basal manganese centers that are coordinated by the trinucleating ligand framework. This property allowed greater control over structure composition and connectivity. The first Mn_4O_4 complexes obtained by this method demonstrated that the multinucleating ligand framework strategy allows synthetic access to intricate clusters in a number of oxidation states and that these clusters can interconvert through multiple redox changes, a key feature in modeling the steps of the Kok cycle of the OEC.

All of the complexes described above are characterized by a high degree of symmetry and the presence of predominantly N-donor ligands, whereas the core of the OEC is in fact asymmetric and ligated by carboxylates and only one N-donor. In the following we describe how the efforts to introduce calcium to the cluster led to more diverse structures and eventually to the synthesis of carboxylate-bridged Mn_3CaO_4 cubanes.

Heterometallic complexes

The redox-inactive Ca^{2+} is an essential component for photosynthetic water oxidation, but its role in catalysis remains unclear. It is likely that the role of Ca^{2+} is not simply structural, as addition of Cd^{2+}, a divalent ion of similar ionic radius to Ca^{2+}, inhibits OEC activity [390]. Within the series of studied redox-inactive metal ions,

only Sr^{2+}, an ion of similar Lewis acidity to Ca^{2+}, has been shown to retain water oxidation activity (ca. 40%) upon substitution for Ca^{2+}. Proposed nonstructural functions of Ca^{2+} have included coordination of water or hydroxide involved in nucleophilic mechanisms of O-O bond formation,[390] participation in hydrogen-bonding interactions with nearby redox-active tyrosine residues,[273, 363, 362] or modulation of the reduction potential of the manganese sites of the OEC [347]. Synthetic heterometallic models have been used to test some of these proposals.

Isolated and structurally characterized heterometallic cluster mimics of the OEC with incorporated Ca^{2+} or Sr^{2+} ions have been achieved only in recent years, as they are more synthetically challenging than the homometallic analogs [347, 120, 162, 227, 395]. Oxides have the propensity to bridge multiple metal centers, often in an uncontrolled fashion, resulting in clusters of high nuclearity. This tendency also reduces control over the position and number of Ca^{2+} ions within the cluster.

The first distinct cuboidal $Mn(IV)_3CaO_4$ unit was synthesized by Agapie and co-workers (Fig. 1.14).[163] In subsequent work, the Ca^{2+} ion of this heterometallic oxomanganese cubane cluster was replaced by different metals such as Mn^{3+}, Sr^{2+}, Zn^{2+}, Sc^{3+}, Y^{3+}, Gd^{3+}, Ln^{3+} to investigate the role of redox inactive metal in tuning the redox potentials of the clusters.[346, 162, 203] In all compounds the approximately octahedral environment of Mn ions is stabilized by coordination of three alkoxide groups and three pyridine groups attached to an appropriately designed 1,3,5-triarylbenzene spacer. In the lanthanoid series, the crystal structure of Dy^{3+} substituted cubane also shows two water molecules coordinated to Dy^{3+}, reminiscent of the two Ca-bound water molecules in the OEC [203].

A complex with a unique dangling Ca^{2+} ion attached to a distinct Mn_3Ca cubane was first reported by Mukherjee et al. (Fig. 1.15) [227]. The complex is composed of an asymmetric $Mn(IV)_3CaO_4$ core where the metal ions are bridged exclusively by carboxylate/carboxylic acid ligands. The external seven-coordinate Ca^{2+} is connected to one of the oxo bridges and to six carboxylates, three of which bridge it to Mn ions of the cubane. Dominant ferromagnetic coupling results in a high spin, $S = 9/2$ ground state. The magnetic and spectroscopic (EPR) properties of this molecule have been carefully characterized, [227] and thus the complex served as an invaluable reference in quantum chemical analysis of the electronic properties of manganese–calcium cubanes.[186]

Agapie and co-workers described a rational way to increase the basicity of μ_3–oxo ligands by modulating ligand scaffolds and desymmetrizing the Mn3CaO4 cluster.[162] In this way they could obtain a Ag–Mn_3CaO_4 complex, where the dangling Ag^+ is linked to the cubane via a μ_4–oxo, a μ_2-alkoxide, and a pyridine (Fig. 1.16).[162] Thus, the synthesis of $[Mn(IV)_3CaAgO_4]$ from $[Mn(IV)_3CaO_4]$ provided an example of a systematic approach for the synthesis of the asymmetric pentanuclear core structure of the OEC.

The latest addition in this series came from Zhang's laboratory; it contains a manganese ion attached to a Mn_3CaO_4 cubane complexes and represents currently the closest mimic of the OEC.[395] This is the first complex to contain a manganese ion attached to the Mn_3CaO_4 cuboidal unit, thus correctly reproducing the metal stoichiometry of the biological cluster (Fig. 1.17). Importantly, it was synthesized with a $Mn(III)_2Mn(IV)_2$ oxidation state distribution that mirrors that of the S_1 state of the OEC and exhibits similar redox properties as the OEC, being able to

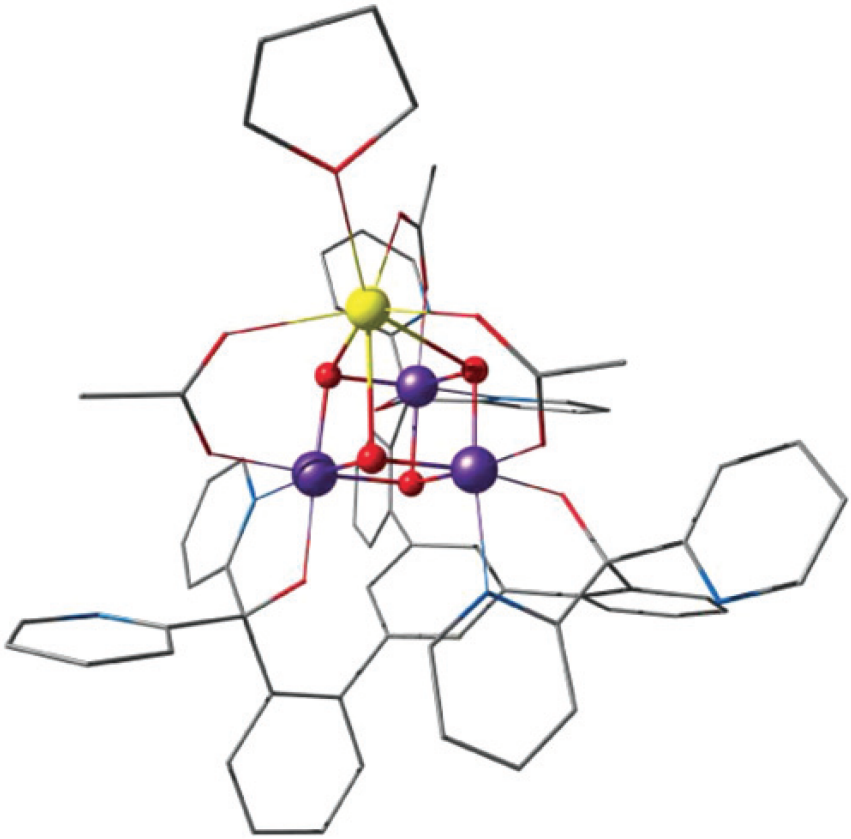

Figure 1.14. First synthetic tetramanganese models of proposed OEC intermediates with cubane-like structure. From ref. [163]

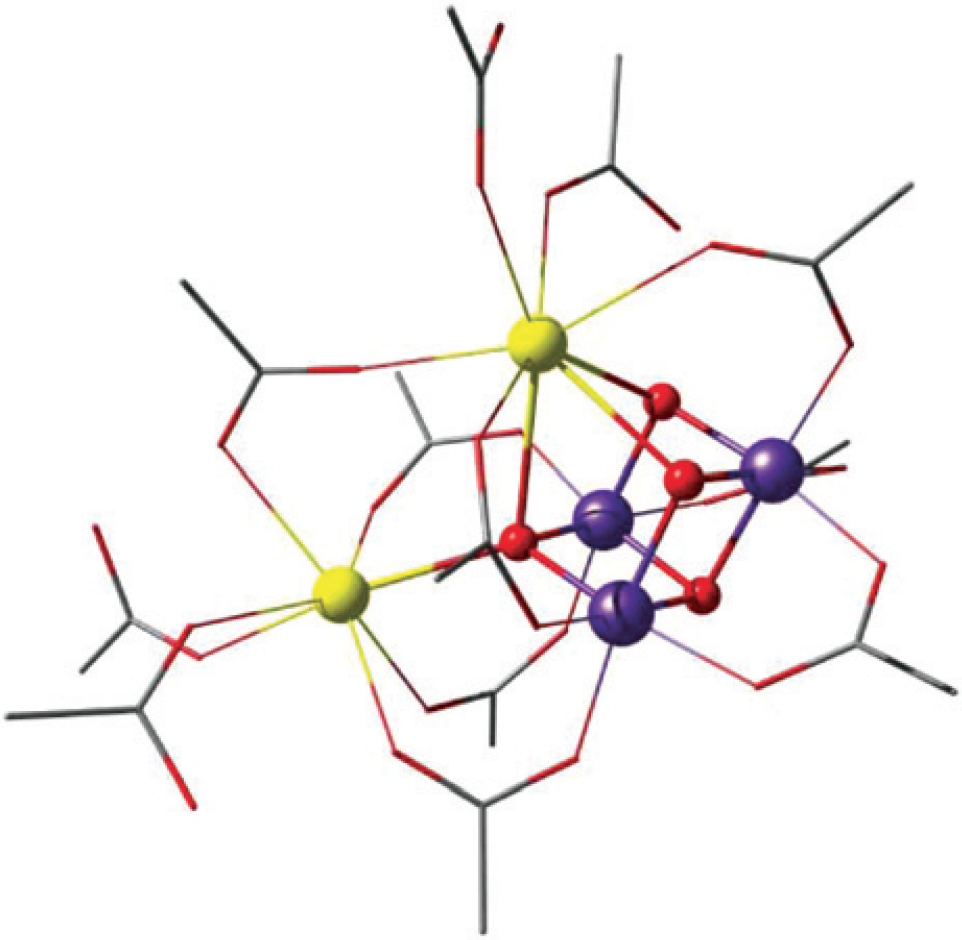

Figure 1.15. Mn3CaO4 cubane complex with attached Ca^{2+} ion, by Mukherjee et al.[227] (tert-butyl groups on carboxylate ligands simplified for clarity).

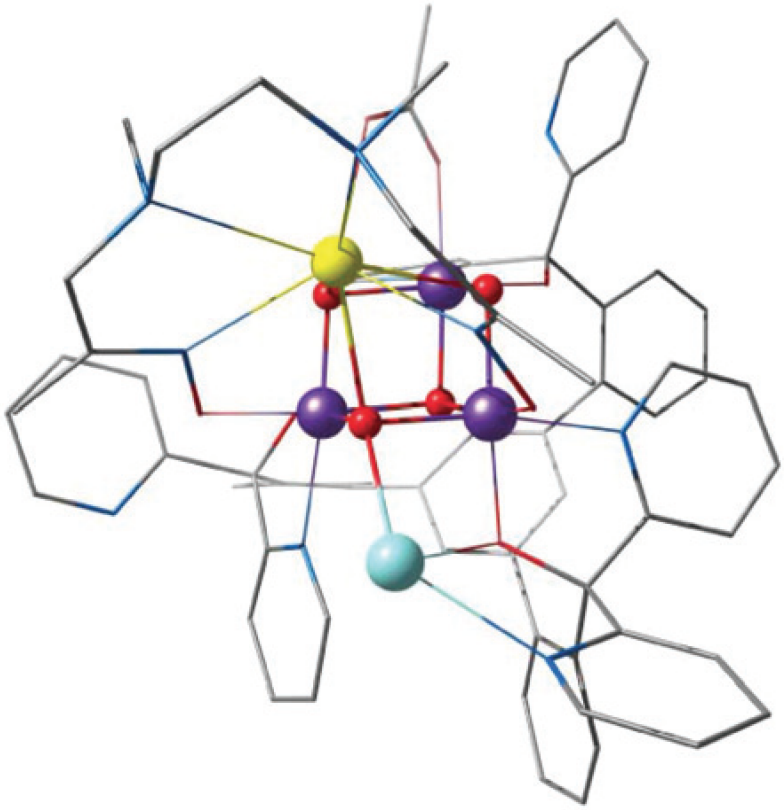

Figure 1.16. Mn3CaO4–Ag complex by Kanady et al. [162]

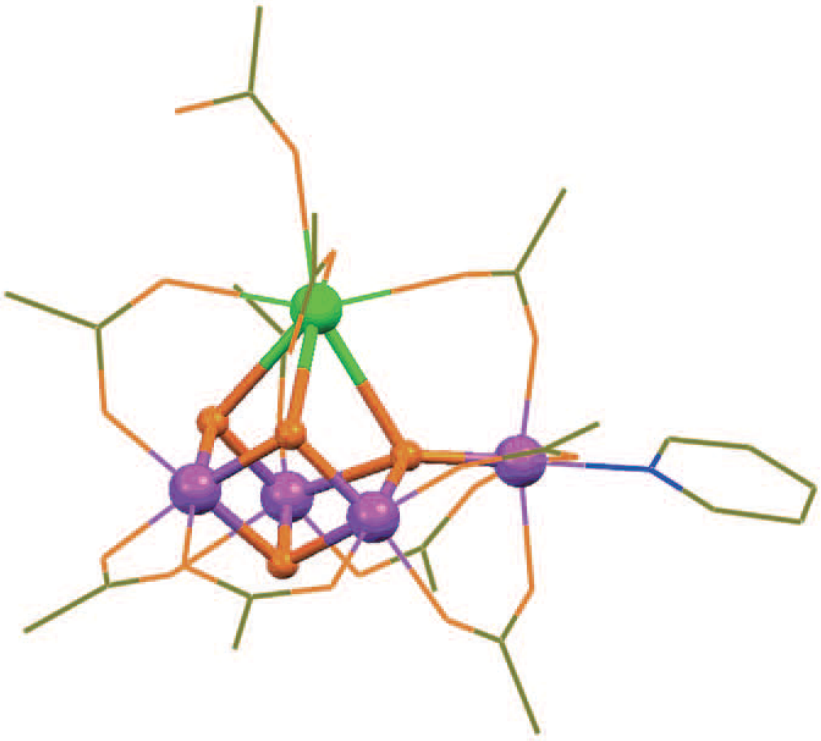

Figure 1.17. Mn3CaO4–Mn complex by Zhang et al. [395]

span several oxidation states. This is a key feature that differentiates this complex from the other cubane-incorporating complexes. In the one electron oxidized state, the complex by Zhang et al. shows two simultaneous EPR signals, a major one at $g \approx 4.9$ and a secondary multiline signal at $g \approx 2$, which are reminiscent of the two signals in the S_2 state of the OEC.

1.4 Summary and Perspectives

Fundamental understanding of the $CaMn_4O_5$ OEC has advanced significantly through ongoing and increasingly sophisticated spectroscopic, structural, and theoretical studies. Synthetic OEC models have mirrored this progress. Using both self-assembly and polydentate ligand templating methods, complicated homo- and heterometallic manganese–oxido clusters have been accessed. These models have allowed the development and evaluation of a number of mechanistic proposals regarding water exchange and oxidation at the OEC.

Overall, the interplay of synthetic, structural, spectroscopic, mechanistic, and computational work has led to tremendous insight into the chemistry and properties of manganese clusters relevant to the OEC. Despite these advances, the mechanism

of water oxidation remains debated. The development of more accurate models, including the full OEC, is a direction that will likely provide exciting new insight toward understanding not only the function of the biological system, but also toward delineating the design elements for improved catalysts for artificial photosynthesis.

Obtaining insights from the synthetic models has often been inseparable from a theoretical analysis of their properties and has relied to a large extent on deciphering the fundamental electronic structure basis of geometry–property correlations using modern quantum chemistry that focuses on spectroscopic properties. These cubane-incorporating complexes have already served as sources of insight in this respect, in themselves and in comparison to models of the OEC, as showcased by numerous studies on magnetism, spectroscopy, and redox behavior.

The exact Mn_4CaO_5 stoichiometry with the correct bridging modes, a more open connectivity pattern, and a potentially more flexible/bistable core constitute therefore part of future biomimetic challenges. Beyond these points, synthetic models that attempt to mimic the structure are still short of mimicking functionality.

Chapter 2

Theoretical background

This chapter aims to give a brief overview of computational chemistry, the chief subdivisions of the field, and the situation of methods relevant to the publications presented in this thesis within the field as a whole. Particular focus will be directed to Density Functional Theory (DFT), key principles and vocabulary of the theory, and the features of contemporary practical computational chemistry implementations.

Computational chemistry is the discipline of solving chemical problems by means of computational algorithms. Multiple distinct subdisciplines exist, although a wide degree of overlap can exist between these disciplines due to the desirability of coupling differing levels of computational abstraction together for a variety of real-world problems. A principal distinction between computational methods in chemistry is whether or not explicit treatment of electronic structure is undertaken. This is to say that computational chemistry can be divided into classical models, which neglect explicit treatment of electronic structure, and quantum mechanical (QM) models, which explicitly solve approximations of the Schrödinger wave equation.

The drawbacks of computer simulations can be summarized as follows: 1. they can be only as good as the underlying theory; 2. they must be validated to be sure that no programming error affects the results; 3. even with the newest computers the systems that one can simulate are smaller, and can be simulated for much less time than one would like, thus the approximations due to finite system size or time of simulation should be checked.

A fruitful way to look at simulations is to see them as an experiment of a theory: they look at some consequences of a theory by performing a virtual experiment. Like any experiment the result of a simulation can be affected by experimental error both systematic and random.

In the present work we focus on atomistic simulations, i.e. simulations in which atoms are explicitly present, and furthermore where the nuclei are treated classically, which is an approximation that is valid in the vast majority of cases. Then to specify the state of the system one has to give the positions of all the nuclei, volume, temperature, or the other thermodynamic quantities of interest.

2.1 Schrödinger equation

One of the most important goals of chemistry and physics in the past century has been to understand and predict the properties of many-particle systems using the quantum mechanical laws of the nature. The behaviour of such systems is governed by the non-relativistic and time-independent Schrödinger equation 2.1, 2.2

$$\hat{\mathcal{H}} \left|\Psi\right\rangle = E \left|\Psi\right\rangle \tag{2.1}$$

where $\hat{\mathcal{H}}$ is the Hamiltonian operator, Ψ is a time-independent wavefunction, and E is the observable energy. The Hamiltonian operator $\hat{\mathcal{H}}$ of the Equation 2.1 for molecular systems can be described as a sum of kinetic energy and potential energy operators:

$$\hat{\mathcal{H}} = \hat{\mathcal{T}}_e + \hat{\mathcal{T}}_n + \hat{\mathcal{V}}_{ne} + \hat{\mathcal{V}}_{ee} + \hat{\mathcal{V}}_{nn} \tag{2.2}$$

The first two terms of the above equation represent the kinetic energy operator of electrons ($\hat{\mathcal{T}}_e$) and nuclei ($\hat{\mathcal{T}}_n$), while the third term is the nuclear-electron Coulomb attraction between the M nuclei and N electrons ($\hat{\mathcal{V}}_{ne}$). The last two expressions are the Coulomb repulsion in electron-electron ($\hat{\mathcal{V}}_{ee}$) and nuclear-nuclear ($\hat{\mathcal{V}}_{nn}$) operators. Then the Hamiltonian operator $\hat{\mathcal{H}}$ for a molecular system with M nuclei and N electrons can be written as (in atomic units) [340, 221]:

$$\hat{\mathcal{H}} = -\frac{1}{2}\sum_{i=1}^{N}\nabla_i^2 - \frac{1}{2}\sum_{A=1}^{M}\frac{1}{M_A}\nabla_A^2 - \sum_{i=1}^{N}\sum_{A=1}^{M}\frac{Z_A}{r_{iA}} + \sum_{i=1}^{N}\sum_{j>i}^{N}\frac{1}{r_{ij}} + \sum_{A=1}^{M}\sum_{B>A}^{M}\frac{Z_A Z_B}{R_{AB}} \tag{2.3}$$

where M_A mass, Z_A is atomic number of nuclei A, $r_{iA} = |r_i - R_A|$, $r_{ij} = |r_i - r_j|$, and $R_{AB} = |\mathrm{R}_A - \mathrm{R}_B|$

The observable energy E of the Schrödinger equation is as an expectation value of the Hamiltonian $\hat{\mathcal{H}}$:

$$E = \langle\hat{\mathcal{H}}\rangle = \frac{\langle\psi|\hat{\mathcal{H}}|\psi\rangle}{\langle\psi|\psi\rangle} \tag{2.4}$$

The solution of the Schrödinger equation includes $3N$ spatial variables and N spin variables of electrons and $3M$ spatial variable of the nuclei (ignoring nuclear spin), and therefore finding an exact solution is impossible even for small molecules. One way to circumvent the complete solution is to construct approximations. Such approximate methods have been most successful in explaining a large range of chemical and physical phenomena ranging from bonding, mechanisms in chemistry, magnetism, conductivity, and etc.

2.2 The Born-Oppenheimer approximation

The motion of the electrons can be considered to be significantly faster than the movement of the atomic nuclei as a result of the large difference in their respective masses; the Hamiltonian operator can be simplified if we assume that any change to the nuclear positions is instantly followed by a subsequent change in the electron

positions.[199] This approximation is termed the Born-Oppenheimer approximation and results in the electronic Hamiltonian:

$$\widehat{\mathcal{H}} = -\frac{1}{2}\sum_{i=1}^{N}\nabla_i^2 - \sum_{i=1}^{N}\sum_{A=1}^{M}\frac{Z_A}{\boldsymbol{r}_{iA}} + \sum_{i=1}^{N}\sum_{j>1}^{N}\frac{1}{\boldsymbol{r}_{ij}} = \widehat{\mathcal{T}} + \widehat{\mathcal{V}}_{Ne} + \widehat{\mathcal{V}}_{ee} \tag{2.5}$$

The first term in Eq. 2.5 describes the kinetic energy of each of the N electrons whilst the second and third terms describe the attractive electrostatic interactions between the N electrons and M nuclei and the repulsive potential due to the electron-electron interactions respectively. Exact solutions to the Schrödinger equation presented in Eq. 2.1 may only be found for one-electron systems. Finding approximate solutions to the Schrödinger equation for many electron cases remains the central goal of modern quantum chemistry. The first and most fundamental of the approaches to solve this problem stems from the work of Hartree,[138] later adapted by Fock [111] and Slater [321]. Within the Born-Oppenheimer approximation and neglecting all relativistic and electrostatic effects, the exact N body wavefunction of the system can be approximated by a single Slater determinant (Φ_{SD}). The use of a Slater determinant confirms the application of another fundamental postulate of quantum mechanics, the Pauli Exclusion Principle, arising from the fermionic nature of electrons as elementary particles with a non-integer spin of 1/2. A correct description of these systems requires the wavefunction to be antisymmetric (change sign) with respect to the interchange of two electrons. Mathematically this condition can be fulfilled by the introduction of a normalised Slater determinant.

$$\Phi_{SD}\left(\boldsymbol{r}_1, \boldsymbol{r}_2, \ldots, \boldsymbol{r}_N\right) = \frac{1}{\sqrt{N!}}\begin{bmatrix} \psi_1\left(x_1\right) & \psi_2\left(x_1\right) & \ldots & \psi_N\left(x_1\right) \\ \psi_1\left(x_2\right) & \psi_2\left(x_2\right) & & \psi_N\left(x_2\right) \\ & \vdots & \ddots & \vdots \\ \psi_1\left(x_N\right) & \psi_2\left(x_N\right) & \cdots & \psi_N\left(x_N\right) \end{bmatrix} \tag{2.6}$$

The Slater determinant (Φ_{SD}) is the antisymmetric product of N one-electron wave functions $\Psi_N(\boldsymbol{x}_N$ also known as spin orbitals, which are constructed from spatial orbitals $\phi(\boldsymbol{r})$ and spin functions $\sigma(s)$.

$$\psi_N\left(\boldsymbol{x}_N\right) = \phi(\boldsymbol{r})\sigma(s) \tag{2.7}$$

With s denoting either α (spin up) or β (spin down) spin. Spatial orbitals are usually calculated under the constraint of being orthonormal, while spin functions are orthonormal by definition, i.e. $\langle\alpha|\alpha\rangle = \langle\beta|\beta\rangle = 1$ and $\langle\alpha|\beta\rangle = \langle\beta|\alpha\rangle = 0$

2.3 Density Functional Theory

2.3.1 The Hohenberg-Kohn Theorems

The fundamental quantity of DFT is the electron density ρ, which can in principle be used to determine all properties of the system of interest. For a system with N electrons it is defined by:

$$\rho(r) = N \int \dots \int \left|\Psi\left(\boldsymbol{r}_1, s_1, \boldsymbol{x}_2 \dots, \boldsymbol{x}_N\right)\right|^2 ds_1 d\boldsymbol{x}_2 \dots d\boldsymbol{x}_N \tag{2.8}$$

The physical footing for employing the electron density as the unique variable was established by Hohenberg and Kohn [145] The first Hohenberg-Kohn theorem proves that the ground state energy is a functional of the electronic density ρ. The electronic energy of a given system can therefore be expressed as a functional of the density:

$$E[\rho] = T[\rho] + V_{ee}[\rho] + V_{Ne}[\rho] = F[\rho] + \int \rho(\boldsymbol{x}) v(\boldsymbol{x}) dr \tag{2.9}$$

where $T[\rho]$ is the kinetic energy, $V_{ee}[\rho]$ the electron-electron and $V_{Ne}[\rho]$ the nucleus-electron interaction energy. The Hohenberg-Kohn functional $F[\rho]$ is a system-independent universal functional of ρ:

$$F[\rho] = T[\rho] + V_{ee}[\rho] = \left\langle \Psi \left| \hat{\mathcal{T}} + \hat{\mathcal{V}}_{ee} \right| \Psi \right\rangle \tag{2.10}$$

where the electron-electron repulsion term $V_{ee}[\rho$ can be further partitioned into the classical Coulomb repulsion energy $J[\rho]$ and a non-classical term E_{ncl}.

$$V_{ee}[\rho] = J[\rho] + E_{ncl} = \frac{1}{2} \iint \frac{1}{r_{12}} \rho\left(\boldsymbol{x}_1\right) \rho\left(\boldsymbol{x}_2\right) d\boldsymbol{x}_1 d\boldsymbol{x}_2 + E_{ncl} \tag{2.11}$$

The second Hohenberg-Kohn theorem allows use of the variational principle in DFT. The energy $E[\tilde{\rho}(x)]$ determined by a trial density $\rho(x)$ is always an upper bound to the exact energy E_0

$$E_0 \leq E[\tilde{\rho}(x)] \tag{2.12}$$

The exact form of the Hohenberg-Kohn functional is still unknown, especially due to the fact that a proper handling of $T[\rho]$ is very hard to achieve. Otherwise, an exact solution to the Schrödinger equation could be provided within the DFT framework. This gives rise to the ongoing challenge of finding approximate forms of $F[\rho]$ that are required for accurate implementations of DFT.

2.3.2 The Kohn-Sham methodology

In 1965 Kohn and Sham developed a cleverly devised approach to the kinetic energy functional by introduction of a (hypothetical) non-interacting reference system, which offers exactly the same electron density as the real system.[179] While the kinetic energy of this non-interacting system $T_S[\rho]$ is of course not equal to the true kinetic energy of the real interacting system $T[\rho]$, it is still able to account for the largest part of it employing so-called Kohn-Sham (KS) orbitals.

The Hohenberg-Kohn functional can be rewritten in the following form:

$$F[\rho] = T_S[\rho] + J[\rho] + E_{XC}[\rho] \tag{2.13}$$

The quantity $E_{XC}[\rho]$ is called exchange-correlation energy and contains the difference between T and T_S and the nonclassical part of $V_{ee}[\rho]$.

$$E_{XC}[\rho] = T[\rho] - T_S[\rho] + V_{ee}[\rho] - J[\rho] \tag{2.14}$$

Combining Equations 2.9 and 2.14 one arrives at the Kohn-Sham energy expression:

$$E[\rho] = \int \rho(\boldsymbol{x}) v(\boldsymbol{x}) d\boldsymbol{x} + T_S[\rho] + J[\rho] + E_{XC}[\rho] \tag{2.15}$$

The wavefunction of a system of N non-interacting electrons can be expressed via a Slater-Determinant built from M KS orbitals Ψ_i, where the sum of the squares of the KS orbitals yields the true electron density. These orbitals obey HF-like one-electron equations of the following form:

$$\hat{f}_{\mathrm{KS}} \psi_i = \epsilon_i \psi_i \tag{2.16}$$

employing the Kohn-Sham operator:

$$\hat{f}_{\mathrm{KS}} = -\frac{1}{2}\nabla^2 + v_{\mathrm{eff}}(x) \tag{2.17}$$

The effective Kohn-Sham potential is defined by:

$$v_{\mathrm{eff}}\left(x_1\right) = v\left(x_1\right) + \int \frac{\rho\left(x_2\right)}{x_{12}} dx_2 + v_{XC}\left(x_1\right) \tag{2.18}$$

with the exchange-correlation potential:

$$v_{XC}\left(\boldsymbol{x}_1\right) = \frac{\delta E_{XC}[\rho]}{\rho\left(\boldsymbol{x}_1\right)} \tag{2.19}$$

Only knowledge of the exact exchange-correlation energy functional $E_{\mathrm{XC}}[\rho]$ would in principle provide the exact density. A brief summary of approximations to use for $E_{\mathrm{XC}}[\rho]$ with an overview of ongoing research and progress in the field is given in the next section. In any case, the KS approach includes exchange and correlation, unlike the HF method, while retaining the crucial advantage of one-electron approaches being computationally much less expensive than correlated post-HF methods.

2.3.3 Exchange Correlation Functionals

As the true form of the exchange-correlation energy functional is unknown, a number of approximations have been developed and applied. The probably most widely used approaches will be explained here briefly.

In the Local Density Approximation (LDA) it is assumed that the local density can be treated like a uniform electron gas. The exact analytical form of the exchange energy functional for the uniform electron gas is known [322] and the correlation energy can be obtained from highly accurate quantum Monte Carlo simulations[54]. Although working surprisingly well when considering the differences between the uniform electron gas and real chemical systems, the LDA approximation usually overestimates bond strengths, resulting in too short bond lengths. These facts limit its use in quantum chemistry.

$$E_{\mathrm{XC}}^{\mathrm{LDA}}[n] = \int d^3 r n(\boldsymbol{r}) \tag{2.20}$$

While the LDA depends only on the density itself, its derivatives are used in the Generalized Gradient Approximation (GGA). The first gradient corrected functionals were developed in 1986, resulting in exchange functionals by Becke,[24] or Perdew and Wang,[279] and a correlation part by Perdew [276]. Functionals commonly in use are the exchange functional by Becke [25] supplemented by the correlation functional of Perdew [276] (BP86) or Lee, Yang and Parr [195] (BLYP) or PBE, including the exchange and correlation parts by Perdew, Burke and Ernzerhof [277]. Calculations performed with GGA methods usually yield good results for thermochemistry and bond lengths, which makes them a suitable pick in chemistry. Incorporation of higher derivatives of the density and the kinetic energy density is realized in so-called meta-GGAs, like TPSS [321, 279, 94, 343] or τHCTH [37].

Combination of the exact exchange of the HF scheme with the DFT approach results in hybrid functionals. They benefit from the fact that the exact (HF) exchange is self-interaction free and shows the correct asymptotic behavior, while the DFT exchange partly provides for non-dynamical correlation:

$$E_{\mathrm{XC}}^{\mathrm{hybrid}} = a E_{\mathrm{X}}^{\mathrm{exact}} + (1-a) E_{\mathrm{X}}^{\mathrm{DFT}} + E_{\mathrm{C}}^{\mathrm{DFT}} \tag{2.21}$$

Functionals exhibiting a well-balanced form between these two contributions have been shown to perform remarkably well, especially for transition metal systems, where the influence of the exact exchange is crucial [269, 230, 231]. Admixture of exact exchange affects the total and spin density for such systems in basically three different ways: (i) the metal-ligand bond becomes more ionic as compared to the GGA or LDA level,[269, 230, 289, 323, 170, 71] (ii) an enhancement of valence-shell spin polarization in covalent bonds can be observed,[230] and (iii) the core-shell spin polarization is improved as well. However, it should be mentioned, that the usage of Hartree-Fock exchange term is computationally more expensive particularly for certain basis sets (e.g. plane waves) as the formal scaling is with the fourth power of the number of orbitals. Furthermore, it is not clear how much exact exchange should be included in the calculation thus resulting in further complications.

The probably most popular hybrid exchange-correlation functional is the B3LYP [27, 327] functional with 20% of exact exchange, which has been employed for the majority of calculations in this thesis:

$$E_{\mathrm{XC}}^{\mathrm{B3LYP}} = a E_{\mathrm{X}}^{\mathrm{exact}} + (1-a) E_{\mathrm{X}}^{\mathrm{Slater}} + b \Delta E_{\mathrm{X}}^{\mathrm{B88}} + E_{\mathrm{C}}^{\mathrm{VWN}} + c \Delta E_{\mathrm{C}}^{\mathrm{LYP}} \tag{2.22}$$

Empirical parameters b and c are 0.72 and 0.81, respectively, $E_{\mathrm{X}}^{\mathrm{Slater}}$ is the LDA exchange energy, $E_{\mathrm{X}}^{\mathrm{B88}}$ is the gradient corrected exchange energy by Becke, and $E_{\mathrm{C}}^{\mathrm{VWN}}$ and $E_{\mathrm{C}}^{\mathrm{LYP}}$ are the LDA and gradient corrected correlation terms. Although performing very well, hybrid functionals, as a whole, are still suffering from self-interaction errors. Beside that, they also struggle with accurate handling of long-range interactions, e.g. dispersion effects.

In addition to mixing the HF-exchange into a given density functional, the extended hybrid functionals developed by Grimme and co-workers are composed of

a fraction of the MP2 correlation energy calculated with hybrid DFT orbitals, and that can be expressed as:

$$E_{\mathrm{XC}} = aE_{\mathrm{X}}^{\mathrm{HF}} + (1-a)E_{\mathrm{X}}^{\mathrm{DFT}} + (1-c)E_{\mathrm{C}}^{\mathrm{DFT}} + cE_{\mathrm{C}}^{\mathrm{MP2}} \tag{2.23}$$

They recommend the B88 exchange functional, the LYP correlation functional and the parameters a = 0.53 and c = 0.27, which gives rise to the B2PLYP functional [126, 30]. The mPW2PLYP double hybrid functional is also well-known [309, 310].

The description above of the three types of functional suggests that there has been constant development of more and more accurate functionals. However, some problems remain that affect the accuracy of DFT. These problems have been widely discussed in many reviews so it will be only briefly presented here.

The first problem is that pure dispersion interactions between unbound chemical species are not well reproduced by common functionals. A pragmatic way of dealing with the problem is to use a normal functional, which does not describe dispersion, but to include additional molecular mechanics terms to treat this effect. This approach was developed most systematically by Grimme and coworkers [126], especially leading to their D3 damped dispersion term [127] (which is damped to a constant at short range). Although the method has been found useful for the systems with thorough parametrization, it still has two main disadvantages: (i) the add-on terms are unphysical and hence they are different for each XC functional; (ii) like all molecular mechanics methods, they can suffer from lack of transferability.

The second is that the most approximate functionals give a convex interpolation of the energy as a function of fractional charge. This deviation causes an artificial tendency towards the delocalization of the electrons, which leads to incorrect densities, molecular properties, barrier heights, band gaps, and excitation energies. The incorrect treatment of static/strong correlation is among the most challenging problems in DFT. It is generally recognized that static correlation arises from (near-)degeneracy of the reference Slater determinant with other low-energy configurations, while dynamic correlation is from the mixing of higher-energy excited configurations. Unlike the short-range feature of dynamic correlation, being multicenter in range makes it difficult to model static correlation with (semi)local functionals. It is known, that for systems with fractional spins, the constancy condition [75, 76, 77] requires the energy of a system with fractional-spin states to equate that of the comprising degenerate pure-spin states.

Thus, perspectives should be based on understanding the errors of functionals in terms of violations of requirements of the exact XC functional. The quest for a universal XC functional continues.

2.4 Hubbard Correction to DFT

In the DFT approach (and in Hartree-Fock too) a single Slater determinant has been employed. In more accurate approaches a combination of several Slater determinants is applied, ensuring additional degrees of freedom in the fitting procedure at the (big) price of an increased computational cost, like complete active space self-consistent field (CASSCF) [298], in which fixed doubly occupied and unoccupied orbitals are excluded from the active space, and the restricted version RASSCF [215], which

breaks the active space into three subspaces. Among the same family of methods, it is also worth mentioning the generalized active space SCF (GASSCF) method [213], the occupation restricted multiple active space (ORMAS) method [152], generalized valence bond (GVB) [36], and the separated pair (SP) approximation [258]. In these approaches different constraints are followed to divide the active space into subspaces and control the number of configuration state functions in the configuration interaction expansion. Even larger active spaces may be treated using density matrix renormalization group theory (DMRG) [368, 369, 370]. DMRG restates the full configuration interaction (FCI) wave function in terms of orbital occupation numbers and decomposes the corresponding FCI tensor into a contracted matrix product state. Alternative options for recovering dynamical correlation at low cost are in development, including multiconfigurational pair-density functional theory (MC-PDFT) [115, 202]. MC-DFT recovers both static and dynamic correlation through use of an on-top density functional that takes for its arguments the density and on-top pair density (associated with the probability of finding two electrons in a given location) matrices from a multireference wave function calculation such as CASSCF.

The inaccuracy in the description of the electronic behaviour that originates from this fact may be neglected in most of the practical applications, but not for instance in case of systems with a strong electronic correlation, in which the energy required for an electron transfer has the same order of magnitude of the width of the valence band: in this case a small error on the electronic energies might provoke electron transfers which do not actually occur.

In order to reach a solution for this problem, it has to be observed from a different perspective, analyzing where the DFT fails in describing the electrons behaviour. A relevant difference between the DFT description of the system and the reality is that DFT energies smoothly varies with respect to the occupations of the molecular orbitals, because also these fractional occupied molecular orbitals are described by a single wavefunction, and this is not reflected in a discontinuity in the sequence of energy minima. In reality, instead, a system with a fluctuating number of particles is not described by partially filled molecular orbitals, but rather by a statistical mixture of wavefunctions of fully occupied molecular orbitals, and therefore the energy is a weighted average of their energy values [72]

$$E = (1 - W)E_N + WE_{N+1}; \quad W \in [0, 1] \tag{2.24}$$

This is shown in Fig. 2.1, where the difference between these two approaches is drawn too.

A simple idea to fill this discrepancy, then, is trying to reproduce this difference and implement it in the DFT approach as a corrective term of the Hamiltonian. This term is usually called Hubbard correction and the approach as DFT+U approach[72, 143]. It is another ingredient added to KS-DFT as a subshell-dependent correction to on-site Coulomb repulsions (intra-atomic Coulomb and exchange interactions).

This difference is usually reproduced by computing an “exact” contribution and an “average contribution”, and subtracting the latter from the former to avoid double counting.

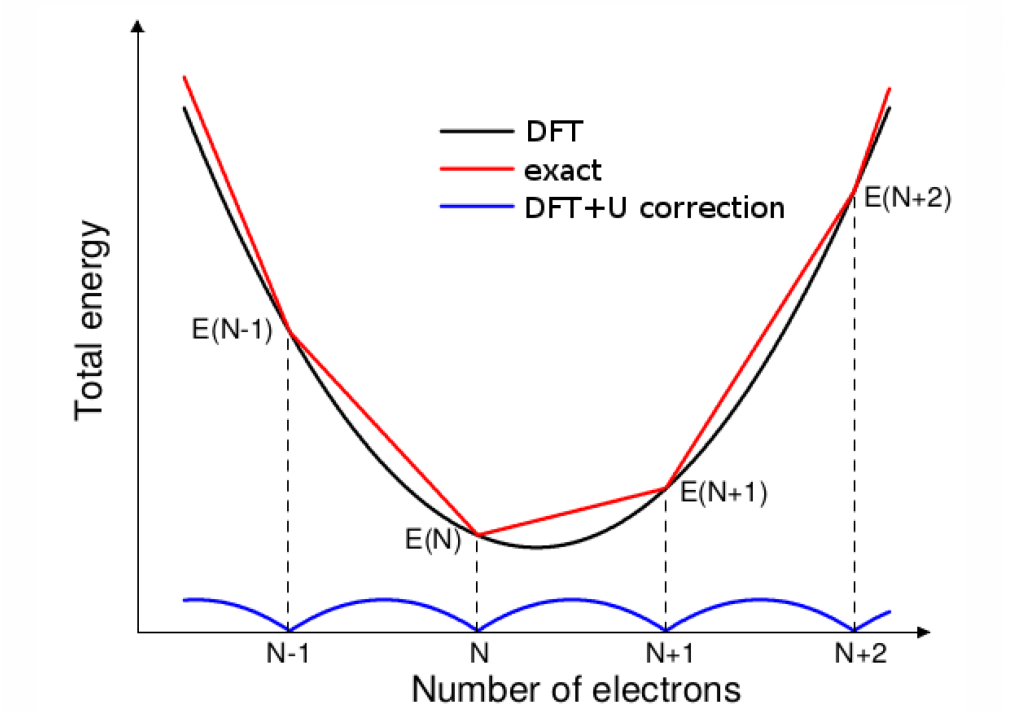

Figure 2.1. The difference (bottom curve) between the "real" energy and the DFT energy is the target result to obtain as a correction term. Adapted from ref. [72]

$$E_{DFT+U}[\rho(r)] = E_{DFT}[\rho(r)] + E_{Hub}\left[n_I^{m\sigma}\right] - E_{ave}\left[n_I^{\sigma}\right] \tag{2.25}$$

where $\rho(r)$ is the electron density; I is the index of the I-th atoms on which Hubbard correction is applied (not span all the atoms necessarily); m is the angular momentum of the orbital; σ is the quantum spin number; $n_l^{m\sigma}$ is the orbital occupation and $n_I^{\sigma} = \sum_m n_I^{\sigma}$.

The reference formalization for these terms have been done by Anisimov et al. [10, 9, 324] as follows:

$$E_{Hub}\left[n_I^{m\sigma}\right] = \frac{U}{2}\sum_I \sum_{m'\neq m}\sum_{\sigma\neq\sigma'} n_I^{m\sigma} n_I^{m'\sigma'} \quad E_{\text{ave}}\left[n_I^{\sigma}\right] = \frac{U}{2}\sum_I \left[\sum_\sigma n_I^{\sigma}\left(\sum_\sigma n_I^{\sigma} - 1\right)\right] \tag{2.26}$$

where U is the parameter which tune the entity of the electron interaction.

Replacing these quantities in Eq. 2.25 we get:

$$E_{DFT+U}[\rho(r)] = \frac{U}{2}\sum_I \left\{\sum_{m'\neq m}\sum_{\sigma\neq\sigma'} n_I^{m\sigma} n_I^{m'\sigma'} - \left[\sum_\sigma n_I^{\sigma}\left(\sum_\sigma n_I^{\sigma} - 1\right)\right]\right\} \tag{2.27}$$

and deriving with respect to the atomic orbital occupation $n_I^{m\sigma}$ we obtain the energy of the orbital, $\epsilon_I^{m\sigma}$

$$\epsilon_I^{m\sigma} = \frac{\partial E_{DFT+U}[\rho(r)]}{\partial n_I^{m\sigma}} = \underbrace{\frac{\partial E_{DFT}[\rho(r)]}{\partial n_I^{m\sigma}}}_{=:\epsilon_{0I}^{m\sigma}} + U\left(\frac{1}{2} - n_I^{m\sigma}\right) = \epsilon_{0I}^{m\sigma} + U\left(\frac{1}{2} - n_I^{m\sigma}\right) \tag{2.28}$$

where $\epsilon_{0I}^{m\sigma}$ is the DFT orbital energy.

The Eq. 2.27 can be re-adapted in many different forms [72, 143] including different additional contribution: here is presented in the one proposed by Dudarev et al. [103, 102]:

$$E_{DFT+U} = E_{DFT} + \frac{U}{2}\sum_k \sum_{\mu,\nu,\mu\neq\nu} \int \frac{\theta_\mu(\boldsymbol{r})\rho\left(\boldsymbol{r}'\right)\theta_\nu(\boldsymbol{r})}{|\boldsymbol{r}-\boldsymbol{r}'|} d\boldsymbol{r}d\boldsymbol{r}' \tag{2.29}$$

where k index span the valence orbitals (usually d orbitals); $\omega_{\mu,\nu}^k$ elements are given by $\omega_{\mu,\nu}^k = \int \frac{\theta_\mu(\boldsymbol{r})\rho(\boldsymbol{r}')\theta_\nu(\boldsymbol{r})}{|\boldsymbol{r}-\boldsymbol{r}'|} d\boldsymbol{r}d\boldsymbol{r}'$

It is worth to mention in the end of this paragraph that the U constant value is often matter of debate. Some elegant approaches for its computation can be found in [281, 72], but in light of the heterogeneity of the applications and of the implementations they can scarcely be assumed as general methods, and so the value is usually tuned with respect to the electronic properties that are needed to be fitted.

Several works [34, 266, 241, 45, 17, 7, 46, 244, 25, 195] have demonstrated the capability of the DFT+U in reproducing electron and magnetic properties of strongly correlated systems. For fully ab-initio predictions of the electronic properties, the parameter U should be calculated by self-consistent methods based, for example, on the linear response theory. An alternative way is the empirical approach, in which the effective U is calculated using an interpolation between data calculated at different U values with the aim of experimental or other theoretical results. In this work we used the latter approach to define a suitable DFT+U framework that can be employed in molecular dynamics simulations. Since it has been shown that the magnetic properties of the Mn4Ca cluster calculated by hybrid functionals are consistent with experimental data, we will use them to define our choice of U. In particular U was chosen using a fitting procedure that minimizes the distance between the coupling constants J_{ij} calculated with DFT+U and the J_{ij}^{B3LYP} evaluated by hybrid functional.

2.5 Molecular Dynamics

Within the Born–Oppenheimer approximation, the nuclei obey the nuclear Schrödinger equation, which was given in its time-independent form in equation 2.1. The time-dependent form reads as:

$$\left(-\sum_{A=1}^{M}\frac{\hbar^2}{2M_A}\nabla_A^2 + E_k(\mathrm{R})\right)\chi_k(\mathrm{R},t) = \mathrm{i}\hbar\frac{\partial}{\partial t}\chi_k(\mathrm{R},t) \tag{2.30}$$

For basic cases such as, e. g., the harmonic oscillator, it can be solved analytically. For larger systems, it can be simplified by approximating the nuclei as classical point particles. For this purpose, the complex nuclear wave function is rewritten as:

$$\chi_k(\mathrm{R},t) = B_k(\mathrm{R},t)\exp\left(\mathrm{i}\frac{S_k(\mathrm{R},t)}{\hbar}\right) \tag{2.31}$$

with real functions $B_k(\mathrm{R},t)$ (amplitude) and $S_k(\mathrm{R},t)$ (phase). Applying this ansatz to equation 2.30 and separating the real and imaginary parts results in two coupled equations for amplitude and phase:

$$\frac{\partial}{\partial t}B_k(\mathrm{R},t) + \sum_{A=1}^{M}\frac{1}{M_A}\left(\nabla_A B_k(\mathrm{R},t)\nabla_A S_k(\mathrm{R},t) + \frac{1}{2}B_k(\mathrm{R},t)\nabla_A^2 S_k(\mathrm{R},t)\right) = 0 \tag{2.32}$$

$$\frac{\partial}{\partial t}S_k(\mathrm{R},t) + \sum_{A=1}^{M}\frac{1}{2M_A}\left(\nabla_A S_k(\mathrm{R},t)\right)^2 + E_k(\mathrm{R}) = \hbar^2\sum_{A=1}^{M}\frac{1}{2M_A}\frac{\nabla_A^2 B_k(\mathrm{R},t)}{B_k(\mathrm{R},t)} \tag{2.33}$$

Equation 2.32 can be interpreted as a continuity equation that ensures the conservation of the probability density $|\chi_k(\mathrm{R},t)|^2$. In equation 2.33, the right-hand side vanishes in the classical limit $\hbar \to 0$, and the Hamilton–Jacobi equation of classical mechanics remains:

$$\frac{\partial}{\partial t}S_k(\mathrm{R},t) + \sum_{A=1}^{M}\frac{1}{2M_A}\left(\nabla_A S_k(\mathrm{R},t)\right)^2 + E_k(\mathrm{R}) = \frac{\partial}{\partial t}S_k(\mathrm{R},t) + H_k(\mathrm{R},\mathrm{P}) = 0 \tag{2.34}$$

with the momenta $\mathbf{P} = \{\mathbf{P}_A\}, \mathbf{P}_A(t) = \nabla_A S_k(\mathbf{R},t)$ and the Hamilton function $H_k(\mathrm{R},\mathrm{P}) = T(\mathrm{P}) + E_k(\mathrm{R})$, where $T(\mathrm{P})$ is the kinetic energy. This can be transformed to the Newtonian equations of motion:

$$\frac{\mathrm{d}}{\mathrm{d}t}\mathrm{P}_A(t) = M_A\frac{\mathrm{d}^2}{\mathrm{d}t^2}\mathrm{R}_A(t) = -\nabla_A E_k(\mathrm{R}(t)) \tag{2.35}$$

This means that the nuclei move according to classical mechanics in the potential that is provided by the electronic energy $E_k(\mathrm{R})$, suggesting the following procedure to study the time evolution of a molecular system: the nuclei are propagated according to equations 2.35, and at any particular time t , the electronic energy and its gradient are obtained by solving the time-independent electronic Schrödinger equation 2.1 for the current nuclear configuration $R(t)$. This approach is called Born–Oppenheimer molecular dynamics (BOMD). The AIMD simulations performed in the course of this thesis are BOMD simulations.

The Newtonian equations 2.35 of motion are usually solved by numerical methods that introduce a discrete timestep Δt . In the Verlet algorithm [209], the nuclear coordinates are expanded in Taylor series up to third order:

$$\mathrm{R}_A(t+\Delta t) = \mathrm{R}_A(t) + \Delta t\frac{\mathrm{d}}{\mathrm{d}t}\mathrm{R}_A(t) + \frac{1}{2}\Delta t^2\frac{\mathrm{d}^2}{\mathrm{d}t^2}\mathrm{R}_A(t) + \frac{1}{6}\Delta t^2\frac{\mathrm{d}^3}{\mathrm{d}t^3}\mathrm{R}_A(t) + O\left(\Delta t^4\right) \tag{2.36}$$

$$\mathrm{R}_A(t-\Delta t) = \mathrm{R}_A(t) - \Delta t\frac{\mathrm{d}}{\mathrm{d}t}\mathrm{R}_A(t) + \frac{1}{2}\Delta t^2\frac{\mathrm{d}^2}{\mathrm{d}t^2}\mathrm{R}_A(t) - \frac{1}{6}\Delta t^2\frac{\mathrm{d}^3}{\mathrm{d}t^3}\mathrm{R}_A(t) + O\left(\Delta t^4\right) \tag{2.37}$$

Adding these two equations and rearranging the terms leads to:

$$\mathrm{R}_A(t+\Delta t) = 2\mathrm{R}_A(t) - \mathrm{R}(t-\Delta t) + \frac{1}{M_A}\Delta t^2\mathrm{F}_A(t) + O\left(\Delta t^4\right) \tag{2.38}$$

where the forces $\mathrm{F}_A(t) = M_A\ddot{\mathrm{R}}(t) = -\nabla_A E_k(\mathrm{R}(t))$ are introduced. The nuclear velocities $\mathrm{V}_A(t) = \dot{\mathrm{R}}_A(t)$ are eliminated in this derivation, but it is often desirable to know them, e. g., to calculate the kinetic energy. Therefore, it is more convenient to apply the velocity form of the Verlet algorithm [339], where coordinates and velocities are given by:

$$\mathrm{R}_A(t+\Delta t) = \mathrm{R}_A(t) + \Delta t\mathrm{V}_A(t) + \frac{1}{2M_A}\Delta t^2\mathrm{F}_A(t) \tag{2.39}$$

$$\mathrm{V}_A(t+\Delta t) = \mathrm{V}_A(t) + \frac{1}{2M_A}\Delta t\left(\mathrm{F}_A(t) + \mathrm{F}_A(t+\Delta t)\right) \tag{2.40}$$

It can be shown that this formulation is equivalent to the original Verlet method, making also velocities available in each step of the simulation. The complete BOMD procedure starting from certain initial coordinates R(0) and velocities V(0) now reads as follows: The coordinates R(t) are used to calculate the forces F(t) by solving the time-independent electronic Schrödinger equation for these coordinates, the new coordinates R($t+\Delta t$) are calculated by equation 2.39, they are used to obtain the new forces F($t+\Delta t$) by solving again the electronic Schrödinger equation, and the new velocities V($t+\Delta t$) are finally given by equation 2.40. This procedure has to be repeated until a reasonable part of the nuclear phase space is sampled.

2.6 CP2K program

Computer simulation can advantageously take a place between theory and experiment. With it the consequences of theory can be explored in a novel way and one can look at details that can be extremely difficult or impossible to look at in experiment. This can help at getting a better insight at the mechanisms that govern a property or a chemical reaction. In the present work all the simulations have been carried out using the CP2K package [354]. CP2K is an open-source project hosted at http: //cp2k.berlios .de/ and is written in Fortran 90. I firmly believe that the development of open-source software is very useful for scientific progress: this way others can easily reproduce your data, and control how the simulation was performed.

2.6.1 Gaussian and plane waves method

All the calculations in the actual work have been performed in the framework of *QUICKSTEP* part of the program using the Gaussian and plane waves (GPW) method [353]. The method uses an atom-centered Gaussian-type basis to describe

the wave functions, but uses an auxiliary plane wave basis to describe the density. With a density represented as plane waves or on a regular grid, the efficiency of Fast Fourier Transforms (FFT) can be exploited to solve the Poisson equation and to obtain the Hartree energy in a time that scales linearly with the system size. Such a dual representation allows for an efficient treatment of the electrostatic interactions, and leads to a scheme that has a linear scaling cost for the computation of the total energy and Kohn-Sham matrix with respect to the system size. The first representation of the electron density $n(r)$ is based on an expansion in atom centered, contracted Gaussian functions :

$$n(\boldsymbol{r}) = \sum_{\mu\nu} P^{\mu\nu} \varphi_\mu(\boldsymbol{r}) \varphi_\nu(\boldsymbol{r}) \tag{2.41}$$

where $P^{\mu\nu}$ is a density matrix element, and $\varphi_\mu(\boldsymbol{r}) = \sum_i d_{i\mu} g_i(\boldsymbol{r})$ with primitive Gaussian functions $g_i(\boldsymbol{r})$ and corresponding contraction coefficients $\mathrm{d}_{i\mu}$.

The second representation employs an auxiliary basis of plane waves, and is given by:

$$\tilde{n}(\boldsymbol{r}) = \frac{1}{\Omega} \sum_{\boldsymbol{G}} \tilde{n}(\boldsymbol{G}) \exp(i\boldsymbol{G} \cdot \boldsymbol{r}) \tag{2.42}$$

where Ω is the volume of the unit cell, and $\boldsymbol{G}$ are the reciprocal lattice vectors. The expansion coefficients $\tilde{n}(\boldsymbol{G})$ are such that $\tilde{n}(\boldsymbol{r})$ is equal to $n(\boldsymbol{r})$ on a regular grid in the unit cell. The difference $|n(\boldsymbol{r}) - \tilde{n}(\boldsymbol{r})|$ goes to zero as the cutoff energy E_{cut} goes to infinity. This choice allows for a rapid conversion between $n(\boldsymbol{r})$, $\tilde{n}(\boldsymbol{r})$ and $\tilde{n}(\boldsymbol{G})$ using an efficient mapping procedure and fast Fourier transforms (FFT).

Using this dual representation, the Kohn-Sham DFT energy expression [145, 179] as employed within the GPW framework is defined as:

$$\begin{aligned}
E[n] =& E^{\mathrm{T}}[n] + E^{\mathrm{V}}[n] + E^{\mathrm{H}}[n] + E^{\mathrm{XC}}[n] + E^{\mathrm{II}} \\
=& \sum_{\mu\nu} P^{\mu\nu} \left\langle \varphi_\mu(\boldsymbol{r}) \left| -\frac{1}{2}\nabla^2 \right| \varphi_\nu(\boldsymbol{r}) \right\rangle \\
&+ \sum_{\mu\nu} P^{\mu\nu} \left\langle \varphi_\mu(\boldsymbol{r}) \left| V^{\mathrm{PP}}_{\mathrm{loc}}(r) \right| \varphi_\nu(\boldsymbol{r}) \right\rangle \\
&+ \sum_{\mu\nu} P^{\mu\nu} \left\langle \varphi_\mu(\boldsymbol{r}) \left| V^{\mathrm{PP}}_{\mathrm{nl}}(\boldsymbol{r}) \right| \varphi_\nu\left(\boldsymbol{r}'\right) \right\rangle \\
&+ 2\pi\Omega \sum_{\boldsymbol{G}} \frac{\tilde{n}^*(\boldsymbol{G}) \tilde{n}(\boldsymbol{G})}{G^2} \\
&+ \int e^{\mathrm{XC}}(\boldsymbol{r}) d\boldsymbol{r} \\
&+ \frac{1}{2} \sum_{I \neq J} \frac{Z_I Z_J}{|\boldsymbol{R}_I - \boldsymbol{R}_J|}
\end{aligned} \tag{2.43}$$

where $E^{\mathrm{T}}[n]$ is the electronic kinetic energy, $E^{\mathrm{V}}[n]$ is the electronic interaction with the ionic cores, $E^{\mathrm{H}}[n]$ is the electronic Hartree energy and $E^{\mathrm{XC}}[n]$ is the exchange-correlation energy. The interaction energies of the ionic cores with charges

Z_A and positions R_{Aa} is denoted by E^{II}. $E^{\mathrm{V}}[n]$ is described by norm-conserving pseudopotentials with a potential split in a local part $V_{\mathrm{loc}}^{\mathrm{PP}}(r)$ and a fully non-local part $V_{\mathrm{nl}}^{\mathrm{PP}}$.

2.6.2 Pseudopotentials

Normally the core electrons affect in negligible way the electronic properties, and most physical and chemical properties are mainly given by the valence electrons. This means that an accurate description of the core electrons is not necessary for many applications (including bond breaking and formation). An accurate description of the valence electrons can be obtained using a pseudopotential description of the nuclei. A technique that is well established in the plane wave community. The idea of the pseudopotential is to describe explicitly only the valence electrons, and replace the effect of the core electrons with a suitably modified potential. The valence electrons should have the same behavior (eigenvalues) as in the all-electron case, pseudopotential should be as smooth as possible, and it should be transferable (i.e. applicable to many different situations). For the GPW method we take advantage of the experience with the pseudopotential scheme, and implement it using the pseudopotential of Goedecker, Teter, and Hutter (GTH) [122]. The norm-conserving, separable, dual-space GTH pseudopotentials consist of a local part including a long-range (LR) and a short-range (SR) term:

$$\begin{aligned} V_{\mathrm{loc}}^{\mathrm{PP}}(r) =& V_{\mathrm{loc}}^{\mathrm{LR}}(r) + V_{\mathrm{loc}}^{\mathrm{SR}}(r) \\ =& -\frac{Z_{\mathrm{ion}}}{r}\,\mathrm{erf}\left(\alpha^{\mathrm{PP}} r\right) + \sum_{i=1}^{4} C_i^{\mathrm{PP}} \left(\sqrt{2}\alpha^{\mathrm{PP}} r\right)^{2i-2} \exp\left[-\left(\alpha^{\mathrm{PP}} r\right)^2\right] \end{aligned} \tag{2.44}$$

with
$\alpha^{\mathrm{PP}} = \frac{1}{\sqrt{2} r_{\mathrm{loc}}^{\mathrm{PP}}}$
and a non-local part:

$$V_{\mathrm{nl}}^{\mathrm{PP}}\left(\boldsymbol{r}, \boldsymbol{r}'\right) = \sum_{lm} \sum_{ij} \left\langle \boldsymbol{r} | p_i^{lm} \right\rangle h_{ij}^{l} \left\langle p_j^{lm} | \boldsymbol{r}' \right\rangle \tag{2.45}$$

with Gaussian-type projectors:

$$\left\langle \boldsymbol{r} | p_i^{lm} \right\rangle = N_i^l Y^{lm}(\hat{\nabla}) r^{l+2i-2} \exp\left[-\frac{1}{2}\left(\frac{r}{r_l}\right)^2\right] \tag{2.46}$$

where N_i^l are normalization constants and Y^{lm} spherical harmonics. The small set of GTH pseudopotential parameters $r_{\mathrm{loc}}^{\mathrm{PP}}$, C_i^{PP}, r_l, and h_{ij}^l have been optimized with respect to atomic all-electron wave functions as obtained from fully relativistic density functional calculations using a numerical atomic program. The optimized pseudopotentials include all scalar relativistic corrections via an averaged potential,[139] and improve therefore the accuracy for applications involving heavier elements.

2.6.3 Basis set

The electron density, and all the operators to be representable in the computer simulations need to be expanded on a finite basis. This obviously introduces an error, and the exact form and amount of the error depend on the basis set used. Plane waves, or any representation that treats all the points of the space in the same way has a very natural way to control the error: the grid spacing (or energy cutoff).

The density changes a lot more close to the core of the atom, so it make sense to use a basis that has more variability close to the core. The Gaussian orbital functions that we use in the GPW method are such a basis. Having a non-uniform spatial dependence, actually a localized atom centered basis that can be integrated analytically as we do has many advantages, but together with the advantages there are also drawbacks. The error is not anymore controlled by just one easy parameter. Even if the variational principle guarantees that the error in absolute energy will always decrease increasing the basis set, one can get worse relative energies and forces.

For this reason care is needed in the construction of basis sets of increasing accuracy. Significant experience exists with Gaussian basis sets and there are a number of formats. Whereas polarization and diffuse functions can normally be adopted from published basis sets, the valence part of the basis has to be generated for the usage with the GTH pseudopotentials. A systematically improving sequence of basis sets for use with the GTH pseudopotentials was optimized by Matthias Krack for all first- and second-row elements.

Primitive Gaussian functions were contracted using the coefficients of the respective pseudo atomic wave functions. In addition, a split valence scheme was applied to enhance the flexibility of the valence basis part. The splitting was increased in line with the number of primitive Gaussian functions employed from double- (DZV) over triple- (TZV) up to quadruple-zeta valence (QZV). For instance, the basis set sequence for oxygen starts with four primitive Gaussian functions on the DZV level, uses five functions for TZV, and finally six on the QZV level. Moreover, these basis sets were augmented by polarization functions which were taken from the all-electron basis sets cc-pVXZ (X = D, T, Q) of Dunning [104, 377], but only the first p or d set of polarization functions was used depending on the actual element. In that way a new sequence of basis sets was created with an increasing number of primitive Gaussian functions and polarization functions for each first- and second-row element. The basis sets were labeled DZVP, TZVP, TZV2P, QZV2P, and QZV3P due the applied degree of splitting and the increasing number of provided polarization functions.

2.6.4 Wave function optimization

The calculation of the electronic ground state corresponds to the minimization of the electronic energy (Eq. 2.5) with respect to the orthonormal one-particle orbitals which are used to construct one-particle density matrix of the system. One of most commonly used method for this kind of optimization is diagonalization combined with a direct inversion (DIIS) [135]. DIIS requires often only 10 to 20 Kohn–Sham matrix constructions and hence has become the method of choice for many electronic

structure calculations. However, in some cases diagonalization–DIIS might not converge to any solution. Methods with guaranteed convergence are therefore the best choice for the accurate SCF calculation of medium and large systems. The method that we have used to minimize the total ground state energy of a system by an iterative self-consistent field (SCF) procedure is an efficient orbital transformation (OT) method [352]. The OT method is based on a minimization of the energy functional using the new set of variables to perform orbital transformations. Using available preconditioners with different computational cost and efficiency, one can achieve the number of iterations that is very similar to the DIIS approach with guaranteed convergence.

Diagonalization of the Kohn–Sham matrix can be avoided and the sparsity of the overlap and Kohn–Sham matrix can be exploited. If sparsity is taken into account, the method scales as $O(MN^2)$, where M is the total number of basis functions and N is the number of occupied orbitals. The relative performance of the method is optimal for large systems that are described with high quality basis sets, and for which the density matrices are not yet sparse.

2.7 Vibrational Spectroscopy

For a deep understanding of molecules, the knowledge of their precise atomic structure and dynamics is required. In particular, to understand the reaction mechanism, structural insights at the sub-Å level are essential, since such changes are crucial for catalysis. Changes in molecular structure are monitored at atomic resolution by vibrational spectroscopy. A change in bond length of 0.001 Å corresponds to a shift of the vibrational frequency of 1 cm^{-1} in the case of phosphates. However, the overlay of many geometrical changes and the coupling between vibrations prevent obtaining the structural details directly from the vibrational spectrum without a thorough theoretical analysis. Therefore, complementary vibrational spectroscopy and quantum mechanical calculations are frequently used in literature, in particular for small molecules.

Since IR spectroscopy is sensitive to molecular vibrations inducing appreciable oscillations of the molecular dipole moment, and a molecule's set of vibrational frequencies and associated IR intensities are unique to that molecule, a molecule's IR spectrum provides a "signature" or "fingerprint" that can aid identification. This thesis is a theoretical work in that all original IR spectra presented were calculated based on various computational techniques. Emission or absorption of radiation by molecules in the IR region of the electromagnetic spectrum is primarily due to molecular vibrations, not overall rotations of the molecule or transitions between electronic states. As the atomic nuclei are displaced from their equilibrium positions by vibration of the molecule, the distribution of electric charge in the molecule changes accordingly. In classical electromagnetic theory, charges undergoing oscillations in position will emit radiation at the same frequency as the oscillation.

Although, computational vibrational spectroscopy is a mature field, yet two broad challenges can be identified. It is certainly a challenge to compute numerically exact IR spectra, but a complementary one is to compute spectra for systems of ever increasing size and complexity. First of all, the ground-state potential energy

surface must be obtained in the limit of taking into account full electron correlation in the complete basis set limit. Secondly, on top of that comes the requirements to solve the nuclear Shrodinger equation quasi-exactly either using time-dependent (propagation) or time-independent (diagonalization) methods. Thus, the curse of all the theoretical methods for the exact final answer for spectroscopy yields the fact that in practice the number of fully coupled degrees of freedom must be "sufficiently small".

The main method for predicting molecular vibrations is Normal Mode Analysis (NMA). This method considers vibrations involving small displacements of the atomic nuclei away from their equilibrium positions. In order to do NMA, one must have a way to calculate the total potential energy of the molecule as a function of the atomic displacements. More specifically, it is necessary to know all the mixed second derivatives of the potential energy with respect to the atomic displacements before one can proceed with this analysis.

For small molecules ($>$ 500-1000 atoms) it is possible to directly calculate the total potential energy of the molecule based on quantum theory using quantum chemistry software. Once equilibrium positions of the atomic nuclei are known, the software can calculate the second derivatives of the energy with respect to the atoms displacements from their equilibrium positions. Normal modes of vibration are found by diagonilizing the matrix of mass-weighted second derivatives. Finally, the IR intensity associated with a given normal mode of vibration may be calculated based on the change in the molecule's electric dipole moment when the atomic nuclei are displaced according to that normal mode. For larger molecules such as proteins, ab initio calculations are not practically possible with modern computers because they would require too much time. In this case, it is necessary to switch to approximate potential functions ("force fields") that have been developed for the purpose of performing MD simulations. Regardless of the method used to calculate the potential energy - ab initio or force field - once the normal mode frequencies and associated IR intensities are known, the IR spectrum may be simulated by giving the IR lines finite width through convolution with a Lorentzian peak profile.

Infrared spectroscopy is a powerful technique to unravel the structure and dynamics of molecular systems of ever increasing complexity. For isolated molecules in the gas phase theoretical approaches that directly rely on solving the Schrödinger equation, either approximately or quasi-exactly, are well established. A distinctly different approach to compute infrared spectra can be based on advanced molecular dynamics, itself being based on classical Newtonian dynamics, in conjunction with concurrent first principles electronic structure calculations.

AIMD simulations are particularly appealing in that they allow conformational sampling in phase space, while treating the electornic structure of the molecular system within Born-Oppencheimer approximation. This becomes particularly important for molecules with internal rotations that create multiple, thermally-accessible minima on the potential energy surface.The traditional calculation of normal mode-dependent dipole and polarizability derivatives to simulate infrared and Raman spectra in the static approach or frequency domain is replaced by Fourier transforms of the dipole and polarizability correlation functions in the time domain dynamics simulations. Since no approximations are invoked to approximate the shape of the potential energy landscape in AIMD simulations, vibrational spectra evaluated from

these simulations are inherently more physical than their harmonic analogues that are evaluated at a minimum.

The general philosophy underlying any MD based approach to vibrational spectroscopy is not to compute the numerically exact IR spectrum in order to compare to high-resolution spectroscopy, but to extend theoretical spectroscopy in a meaningful way to "large" and "complex" molecular systems. Consequently, there are two kinds of the methods applied for the calculation of IR spectra: static methods (harmonic and anharmonically corrected) and dynamical methods (which are intrinsically anharmonical). The detailed description of these methods, their respective advantages and disadvantages is given in the following subsections.

2.7.1 Static Harmonic spectra calculations

The general procedure of the NMA approach is as follows: Starting from a reasonable guess of the molecular structure, a minimum on the potential energy surface (PES) is approximated by a quadratic function, implicating that the molecule behaves like a harmonic oscillator (harmonic approximation). Under this assumption, the vibrational frequencies are readily given by the diagonalized Hessian of the potential energy at the minimum, and the intensities can be obtained as derivatives of the dipole moment and the polarazibility for IR and Raman spectra, respectively. This approach will be called here static (harmonic) since no information about large scale dynamical evolution of the system is taken into account, as for instance a jump over a potential barrier resulting in a change of the molecular conformation, or intermolecular interactions that occur in condensed phases.

In usual cases, the harmonic approximation performs very well to reproduce the peak positions and the intensity ratios of the fundamental transitions in a vibrational spectrum. This is often sufficient to interpret experimental data in terms of specific molecular vibrations. For more accurate results, however, the anharmonicity effects that lead, e. g., to a shift of peaks and the occurrence of overtones and combination bands have to be included. To some extent, the shift of the peaks can be taken into account by empirical scaling factors, which are very common due to their simple applicability. More sophisticated techniques to overcome the harmonic approximation are, e. g., vibrational perturbation theory, the vibrational self-consistent field method, vibrational configuration interaction, vibrational coupled cluster theory, the multiconfigurational vibrational self-consistent field method, and multi-reference vibration correlation methods . Although these techniques can yield very accurate results, they are computationally demanding, so they can hardly be used for molecular systems in the order of 100 atoms or more, and the harmonic approximation remains as the primary approach to study large biomolecules.

It is quite evident that the static approach has some intrinsic weaknesses, which we summarize here:

- When more than one minimum on the intramolecular PES exists, we need to take into account each of the equilibrium structures (or at least the lower energy ones). to compute their IR spectra and then possibly generate an average spectrum to be compared with the experimental one;

- If the size of the molecule investigated exceeds the capability of the computational resources, suitable smaller molecular models should be chosen, taking into account the relevant effects occuring in the real molecule;
- Intermolecular interactions are hardly explicitly included (namely solvent effects, crystal field effects, formation of intermolecular clusters);
- The information about the external variables (temperature, pressure, external forces) cannot be taken into account;
- Spectra are usually computed in double harmonic approximations and thus anharmonic effects are lacking. Perturbative methods can be applied, but they are usually limited to rather small systems;
- The spectrum profile is obtained from the computed IR transition probabilities (i.e. from the set of $|\frac{\delta\mu}{\delta Q_i}|^2$ values), assuming that each absorption band is characterized by a Lorentzian (or Gaussian) shape with the fixed band width, described through a Γ_i parameter arbitrarily selected in order to obtain a good fit to the experimental features. Moreover, the description of vibrational motions in terms of small atomic displacements around some well-defined equilibrium geometry may become inadequate when large amplitude torsional motions occur, as indeed it happens in the case of flexible molecles at high temperatures.

Advantages and disadvantages of vibrational anharmonic calculations over the dynamical method in accounting for vibrational anharmonicities can be roughly summarized as follows. The anharmonic methods are still based on geometry optimizations (0 K structures), therefore not including temperature, whereas MD does include temperature in the final spectrum. This is obviously an important attractive argument in favor of MD when the objective of the computations is the interpretation of finite temperature spectroscopy as in IR-MPD and IR-PD experiments.

Moreover, some of the limitations of the NMA method discussed above (e.g. correct sampling of the configuration space, description of intermolecular interactions in assemblies of large systems, dependence on temperature and pressure, effects of the anharmonicity) could be overcome by means of an ab initio or first principles molecular dynamics approach (AIMD). AIMD simulations have been shown to be extremely successful for the prediction of vibrational properties [118].

2.7.2 Dynamic spectral analysis from MD trajectory

In contrast to a single static calculation of a molecular cluster, an AIMD simulation is not connected to a particular minimum on the potential energy surface, but it samples all molecular configurations accessible in the phase space at a certain temperature (though the sampling is restricted by the simulation times and the system sizes that can be afforded, and special algorithms might be necessary to overcome large barriers and to study chemical reactions).

Our methodology consists of DFT-based molecular dynamics simulations, performed within the Born-Oppenheimer (BOMD) framework (using the CP2K package).

In our dynamics, the nuclei are treated classically and the electrons quantum mechanically within DFT formalism. Dynamics consist of solving Newton's equations of motion at finite temperature, with the forces acting on the nuclei deriving from the Kohn-Sham energy. In BOMD the Schrödinger equation for the electronic configuration of the system is solved at each time step of the dynamics (i.e at each new configuration of the nuclei). The knowledge of the evolution with time of the molecular dipole moments is mandatory for the calculation of IR spectra with MD simulations. In the modern theory of polarization, the dipole moment of the (periodic) box cell is calculated with the Berry phase representation, as implemented in the CPMD and CP2K packages.

The average times easily affordable with DFT-based MD are of the order of a few tens of picoseconds for systems composed of a few hundred of atoms, running on massively parallel machines. This is the timescale on which stretching, bending and torsional motions can be properly sampled. One has keep in mind that the length of time has to be commensurate with the investigated vibrational motions. Hence, trajectories around 5 ps are just enough to sample stretching motions in the high frequency domain of 3000-4000 cm^{-1}, provided that several trajectories starting from different initial conformations (structure and/or velocities) are accumulated and averaged for the final IR dynamical spectrum. In the mid-IR domain, trajectories of at least 10 ps each are needed to sample the slower stretching and bending motions of the 1000-2000 cm^{-1} domain. In the far-IR below 1000 cm^{-1}, much longer trajectories are needed to sample properly the much slower motions typical of that domain, i.e. torsional motions, opening/closure of structures, etc. These delocalized and highly coupled motions require trajectories of 20-50 ps on average to be safely sampled, again with a final average over a few trajectories.

All investigations presented in this work have employed BOMD. We apply no scaling factor of any kind to the vibrations extracted from the dynamics. The sampling of vibrational anharmonicities, i.e., potential energy surface, dipole anharmonicities, mode couplings, anharmonic modes, being included in our simulations, by construction, application of a scaling factor to the band-positions is therefore not required. Any remaining discrepancies between dynamical and experiment spectra are likely due to the choice of the DFT/PBE (+dispersion) functional, as DFT-based dynamics are only as good as the functional itself allows. Conformational sampling might be another source of discrepancy: sampling is limited by the length of the trajectories we can afford. It is also clear that vibrational anharmonic effects probed in molecular dynamics are intrinsically linked to the temperature of the simulation. The average conformation at room temperature differs from the frozen 0 K well defined structures.

The AIMD approach misses a number of important quantum effects, such as zero-point energy (ZPE). Also, since it generally is applied "on-the-fly", it must be used with a computationally efficient electronic method, and so DFT is the universal choice. Both the classical treatment of the nuclei and the DFT treatment of the electrons might raise some doubts about the quantitative accuracy of the approach. However with many applications and extensive experience, this approach has evolved into a very useful post-harmonic model with wide applicability. Moreover, for large systems it is the only rigorous enough method for the description of IR spectra.

2.7.3 Effective Normal Mode Analysis

An accurate calculation of anharmonic infrared spectra is one goal to achieve, the assignment of the active bands into individual atomic displacements or vibrational modes is another. In molecular dynamics simulations, interpretation of the infrared active bands into individual atomic displacements is traditionally and easily done using the vibrational density of states (VDOS) formalism. The VDOS is obtained through the Fourier transform of the atomic velocity auto-correlation function:

$$\mathrm{P}(\omega) = \sum_{i=1}^{N} \mathrm{P}_i^{\mathrm{r}}(\omega) = \sum_{i=1}^{N} \int_{-\infty}^{\infty} dt \, \left\langle \vec{\mathrm{r}}_i(t) \cdot \vec{\mathrm{r}}_i(0) \right\rangle \exp\{(i\omega t)\}$$

where P_i^r is the VDOS for the i-th atom of the system (N atoms) in the position $\vec{r_i}$. In this way we can determine the contribution from each atom of the system to the total spectrum [240]. The band assignment from VDOS is limited since the VDOS are delocalized in frequency. The Effective Normal Mode Analysis (ENMA) method then provide us with q_k modes which are the linear combinations of the internal coordinates $q_k(t) = \sum_i Z_k i^{-1} \zeta_i$ and can have VDOS as localized as possible in frequency.

Using the power spectrum function of mode k:

$$\mathrm{P}_k^{\mathrm{q}}(\omega) = \int_{-\infty}^{\infty} dt \, \left\langle \vec{\mathrm{q}}_k(t) \cdot \vec{\mathrm{q}}_k(0) \right\rangle \exp\{(i\omega t)\}$$

the modes are localized in frequency by minimizing the functional:

$$\Omega^{(n)} = \sum_k \left[\frac{\beta}{2\pi} \int_{-\infty}^{\infty} d\omega |\omega^{2n}| P_k^q(\omega) - \right.$$
$$\left. - \left(\frac{\beta}{2\pi} \int_{-\infty}^{\infty} d\omega |\omega^n| P_k^q(\omega) \right)^2 \right]$$

with respect to linear transformation Z. The effective modes are calculated from the equation for the matrix Z^{-1} which is generated from the minimization $\delta\Omega^{(m)}/\delta Z^{-1} = 0$ with the following normalization constraint,

$$\frac{1}{2\pi} \int_{-\infty}^{\infty} d\omega P_k^{(q)}(\omega) = k_B T \delta_{kl}$$

The effective normal modes are effective in the sense that they include temperature, anharmonicities and isomerization sampled along the dynamics.

Chapter 3

Electronic structure and properties of Inorganic Complex Mn_4CaO_4 by Zhang group

3.1 Electronic structure of Synthetic CaMn4O4 complex by Zhang group

The research efforts to unveil the main traits about the process of water oxidation in OEC of PSII has been developed in a multitude of works using various approaches, from spectroscopic techniques like EXAFS [129], ENDOR [188], EPR [80] and X-ray crystallography [335, 14]; to theoretical model studies [325, 320, 206, 52]. There are still plenty of questions related to the water oxidation process that remain totally unclear, like the details of the proton and electron releases along the S states. Nevertheless, the interest in PSII is not only related to a deeper understanding of the biophysics of photosynthesis, but may also be of great inspiration in the research for sustainable energy sources and solar fuels.

On the basis of current crystallographic research on the structure of OEC [335, 14], many different clusters mimics have been synthesized, some closer to natural complex than the others. Several amorphous solids show structural and functional analogies to PSII, as for instance manganese oxides [393, 300], which may sometimes contain Ca atoms in layered structures [373, 286].

Molecular biomimetic models made a further step closer to PSII when asymmetric clusters have been synthesized, i.e. when an external manganese with respect to a cubane structure has been observed. Agapie and coworkers gave a fundamental contribution in this direction extensively exploring synthetic model complexes mimicking the native OEC cluster: the asymmetric Mn_3CaO_4 cubane core of the OEC was indeed obtained in some synthetic complexes [164], afterwards refined over several years in order to be more and more similar to the OEC [347, 162] and recently reported a series of cuboidal Mn_4 complexes as spectroscopic models of the S_2 state of the OEC [196]. Mukherjee et al. [227] obtained a synthetic complex containing the $CaMn(IV)_3CaO_4$ core in which one Ca ion is attached to the Mn_3CaO_4 cubane. Zhang et al. [395] have synthesized the core cubane structure Mn_3CaO_4 linked to a dangling Mn via one oxo bridge and structurally mimics the full site of the OEC in

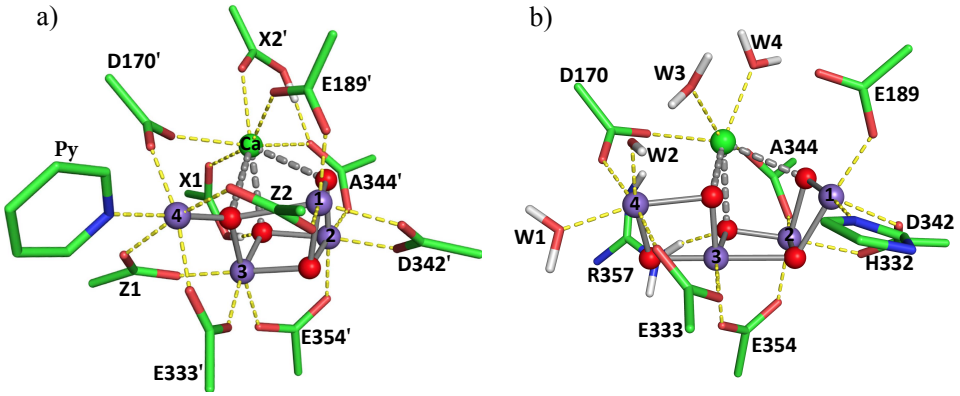

Figure 3.1. a) QM model of the Synthetic catalyst, showing the ligands named as the analogues in the Natural catalyst.The ligands without analogues in the natural structure are named arbitrarily: Z1, Z2 for the carboxylate ligands; X1, X2 for the protonated carboxylic residues. b) QM model of natural complex with the first shell ligands and four water molecules

PSII more closely (Fig. 3.1).

It is important to note that the structural analogy is not exact: the stoichiometry and bonding topology of the core are different because the Complex of Zhang lacks an O bridge between Mn3 and Mn4 compared to the OEC, and hence the "dangler" Mn ion is not a part of a bis(μ–oxo) Mn_2O_2 subunit as it is in the Natural Complex. The more compact inorganic core of Synthetic Complex has a rather rigid bridge between Ca ion and two Mn ions, which cannot work as a semiflexible μ_4–O bridge in the OEC connected either Mn1 and Mn3 or Mn3 and Mn4 ions depending on the open/closed isomeric structure. Bond-valence-sum analysis [395] shows that the Mn oxidation states of Zhang Complex were assigned as $Mn_2^{III}Mn_2^{IV}$, precisely the same as the S_1 state of the OEC.

Despite the absence of water binding sites and the lack of the second μ–oxo bridge between Mn3 and Mn4 in the structure, the artificial cluster can undergo four redox transitions [395, 58] and display two low-temperature EPR signals in its one-electron-oxidized form (S_2 state) at $g \approx 4.9$ and 2, as in the natural OEC. Although the structural resemblance between the two systems is high, recent calculations [270] demonstrate that the EPR signals in S2 state do not arise from the valence isomers hypothesis already proposed for the OEC [45, 266]. A deeper analysis therefore is mandatory for an exhausting comprehension of these compounds.

Full optimization of Synthetic Complex in its neutral state led to the ground state structure with the $Mn1^{III}$-$Mn2^{IV}$-$Mn3^{IV}$-$Mn4^{III}$ spin state, which is clearly indicated by the Mulliken spin populations on the Mn centers, 3.93-3.97 for Mn^{III} ions (local HS d^4 configuration) and 3.03-3.09 for Mn^{IV} ions (local HS d^3 configuration). The model with hydrogen bonding between the carboxylic H and O atoms of carboxylato and oxo ligands is found to be the ground-state structure of the Synthetic Complex. Pantazis et.al [270] have found the same structure in S_1 state as the most stable energetically, among three possible isomers.

Bond	XRD-Zhang	XRD-Umena	UB3LYP-Shoji	B3LYP	PBE
Mn1-O1	1.869	1.8	1.83	1.85	1.84
Mn1-O3	2.014	1.87	2.03	2.01	1.99
Mn1-O5	2.282	2.6	2.40	2.33	2.32
Mn2-O1	1.782	1.82	1.78	1.81	1.81
Mn2-O2	1.876	1.83	1.87	1.9	1.89
Mn2-O3	1.863	2.02	1.85	1.86	1.86
Mn3-O5	1.856	2.4	1.83	1.84	1.84
Mn3-O2	1.84	1.9	1.79	1.83	1.84
Mn3-O3	1.862	2.06	1.85	1.87	1.88
Mn4-O5	1.848	2.5	1.81	1.84	1.83
Mn1-Mn2	2.77	2.68	2.78	2.78	2.74
Mn1-Mn3	3.09	3.2	3.13	3.1	3.09
Mn1-Mn4	3.6	5.0	3.64	3.61	3.6
Mn2-Mn3	2.74	2.7	2.73	2.74	2.7
Mn3-Mn4	3.23	3.0	3.23	3.23	3.22
Ca-Mn1	3.46	3.5	3.57	3.46	3.45
Ca-Mn2	3.36	3.32	3.37	3.38	3.34
Ca-Mn3	3.44	3.4	3.52	3.41	3.4
Ca-Mn4	4.06	3.8	4.19	4.06	4.02

Table 3.1. The inorganic core bond lengths of optimized structures of Synthetic cluster in S_1 state with B3LYP and PBE functionals comparing with the XRD crystal structure of synthetic complex from Zhang *et al.* , XRD of Native OEC from Umena *et al.* and optimized structure of the artificial cluster from Shoji *et al.* at UB3LYP level of theory.

The optimized cluster geometries together with the XRD structure of Synthetic Complex [395], Natural OEC [349] and UB3LYP optimized distances from Shoji [318] are summarized in Table 3.1. The deviation of the model used in the present thesis for the inorganic core is 0.018 Å for B3LYP functional and 0.024 Å for PBE comparing to the Shoji Model [318] with rmsd = 0.056 Å and Pantazis model with TPSSh functional with rmsd = 0.037Å. In particular, it has large deviations in Ca-Mn1, Ca-Mn4 and Mn1-O5 with the deviations of the same bond lengths in our model with B3LYP functional presented in brackets (0.11 (0), 0.13 (0) and 0.12 (0.048) Å, respectively). In view of this, we expect that the present optimized models should also be a more reliable basis for further studying the electronic structure and spectroscopic properties of the synthetic complex in its various states.

The valence-state distribution and ground spin state in the S_1 state are directly analogous to those in the OEC. However, as it was shown in [270], the congruence between the synthetic complex and the OEC in the S_1 and S_3 states holds only partly for the S_2 state. Among all isomeric forms of the one-electron-oxidized state of the synthetic complex, an $S = 5/2$ form emerges as the only energetically accessible isomer. This form explains the appearance of the $g \approx 4.9$ EPR signal, which can be considered analogous to the $g \geq 4.1$ signals associated with the S_2 state of the OEC. However, there is no valence isomer of the synthetic complex that could be identified as the origin of the reported $g \approx 2$ multiline signal, considering both relative energies and spin states. This suggestion is consistent with the experimental observation that the two signals do not interconvert, in conflict with the valence-isomer hypothesis, which implies a negligible valence-shift barrier as a consequence of the structural similarity of the hypothetical valence isomers.

Nevertheless, Zhang Complex is of significant importance to the biological water-splitting field, not only when compared against literature EPR results for the OEC but moreover is essential in the interpretation of FTIR difference spectra of the Natural Complex of PSII as the closest spectroscopic model.

3.2 Vibrational Analysis of Synthetic CaMn4O4 complex by Zhang group

3.2.1 Basis set and functional influence on the IR band positions of single carboxylate residues

In order to analyze IR spectra, probably the most widely-used method is normal mode analysis (NMA), which is based on the expansion of the potential energy surface around the minimum structure of the PES that corresponds to T = 0 K. An excellent accuracy can be achieved when these techniques are applied to small or medium-sized molecules in the gas phase. Static NMA calculations allow us to identify the specific atomic motions within a molecule that are responsible for the various IR peaks. However, effects such as peak broadening, shifts due to anharmonic motions, and temperature effects are neglected by this approach. Thus, methods that enable the decomposition of IR spectra obtained via MD techniques, which fully take into account the aforementioned effects, are called for. There are many DFT methods available at present, the difference between them lies on the choice of

functional form related to the exchange and correlation energy. B3LYP as one of the hybrid DFT methods has become very popular, due to its reliable performance for reasonably large systems along with less expensive computer time cost, at the point that it is considered as a *standard de facto* in quantum chemistry.

In the present chapter, we adopted B3LYP and PBE functionals to study electronic structure and vibrational properties of our model complexes. Through a combination of AIMD simulations and static NMA, we interpret experimental infrared spectra and explore the factors that can affect the stretching frequencies of different groups in our model systems.

First of all, we have been performed static and dynamic calculations of several single molecules (acetate, propionate, pivalate) in order to investigate the influence of such factors as functional, basis set and dispersion correction on the band position of carboxylate stretching vibrations. This also allowed us to reveal the appropriate model of chemistry which is better to use for the vibrational analysis in this region. Secondly this procedure with single molecules helped us to choose the reasonable scaling factor which we used further for artificial and natural oxygen-evolving complexes.

All the isolated molecules exhibit unique infrared vibrations depending on their molecular structure. However, the interpretation of their spectra is focused primarily on the strong asymmetric and symmetric stretching vibrations of the carboxylate group, since these modes show high sensitivity to the coordination geometry of the ligand. These two groups of IR bands are located in the mid-IR region between 1200 cm^{-1} and 1700 cm^{-1}. These vibrations are often coupled with other vibrations of the molecule and are also sensitive to changes in the environment around the carboxylate groups.

The CP2K software package [354] was used to perform quantum chemistry calculations of IR spectra of single carboxylate anions as well as for synthetic and natural water-splitting complexes of Photosystem II. Vibrational modes were calculated for all minimum structures obtained with the different functional/basis set parameters and compared with the experimental IRPMD spectra [260, 326].

Table 3.2 lists the carboxylate stretching frequencies of isolated anions in unscaled form with respect to the functional and basis set choice. Each molecule is considered to be in the gas phase, treated as a single isolated molecule. Starting from the initial molecular structures, the geometry of the molecules was optimized to determine their minimum energy configuration with DZVP and TZVP basis sets and density functional theory (PBE, B3LYP). Vibrational modes of the molecule along with the IR intensities associated with each vibrational mode were calculated using the optimized structure on the same level of theory. The final simulated IR spectrum is constructed by summing Lorentzian spectral line profiles of a specified full width at half maximum (10 cm^{-1}) centered at the frequency of each vibrational mode. This choice for the peak width was based on the combination of the intrinsic width of an individual IR line and experimental broadening.

Figure 3.2 represents the basis set and dispersion correction influence on the COO^- stretching frequencies of propionate molecule calculated with PBE functional. As seen from the figure 3.2 for this kind of small isolated molecule, the dispersion correction role is very low, only about 5 cm^{-1} only for the symmetric stretching region. While the observed basis set influence is appreciable, about 55 cm^{-1} redshift

Anion	DZ B3LYP	TZ B3LYP	TZ B3LYP-D3	DZ PBE	TZ PBE	TZ PBE-D3	Exp.
Propionate	1366	1354	1349	1311	1287	1288	1305
Propionate	1663	1630	1625	1664	1605	1606	1600
Acetate	–	–	1351	–	1324	–	1305
Acetate	–	–	1626	–	1627	–	1590
Pivalate	1343	1319	1324	–	1273	–	–
Pivalate	1668	1627	1630	–	1606	–	–

Table 3.2. Characteristic stretching frequencies of isolated carboxylate anions in the region of 1250-1700 cm^{-1}

Vibration Cut-off	DZ 320	DZ 400	DZ 520	TZ 320	TZ 400	TZ 520	TZV2P 400	TZV2P 520	Exp.
Sym.str.	1314	1306	1306	1299	1299	1300	1296	1297	1305
Asym. str.	1668	1661	1661	1615	1615	1617	1606	1608	1600

Table 3.3. Basis set and cut-off influence on the characteristic carboxylate group stretching frequencies of isolated propionate in the region of 1250-1700 cm^{-1}

with TZVP basis set for the asymmetric carboxylate stretching band and ∼20 cm^{-1} for symmetric region. We assigned the asymmetric and symmetric bending of methyl group at ∼ 1450 cm^{-1} and ∼1340 cm^{-1}, respectively. The scissoring motions of methylene group contribute to the broad band at ∼ 1320 cm^{-1}, while wagging and twisting vibrations of the same group are observed at lower frequencies less than 1300 cm^{-1} and are not presented on Fig. 3.2.

Figure 3.3 shows the same comparison of the frequency shift with respect to the basis set choice for the case of B3LYP functional. The same shift of about 5 cm^{-1} is observed also for this functional with dispersion correction. The TZVP basis set frequencies are shifted to the lower frequencies by ∼40 cm^{-1} and ∼15 cm^{-1} for asymmetric and symmetric regions, respectively.

For both functionals considered above it is seen that better basis set lead to the better agreement with experimental bands. It is worth to mention that the influence of basis set on the frequencies is more prominent for the asymmetric stretching vibrations and PBE functional. Nevertheless, it becomes clear that harmonic frequencies from B3LYP calculations are of similar accuracy as PBE values, but PBE functional is computationally feasible for much larger molecules and spectral decomposition from MD simulations.

The comparison of the IR spectra of Propionate anion with respect to the functional as well as the influence of dynamics on the peak positions of the carboxylate vibrations is shown in Figure 3.4. For the case of TZVP basis set we can find the redshift of the peak positions calculated with PBE functional for ∼60 cm^{-1} and ∼20 cm^{-1} for symmetric and asymmetric stretching, respectively. The first top part the figure demonstrates the IR spectrum derived from MD trajectory as the red solid line and the other parts of the figure demonstrate the results from static

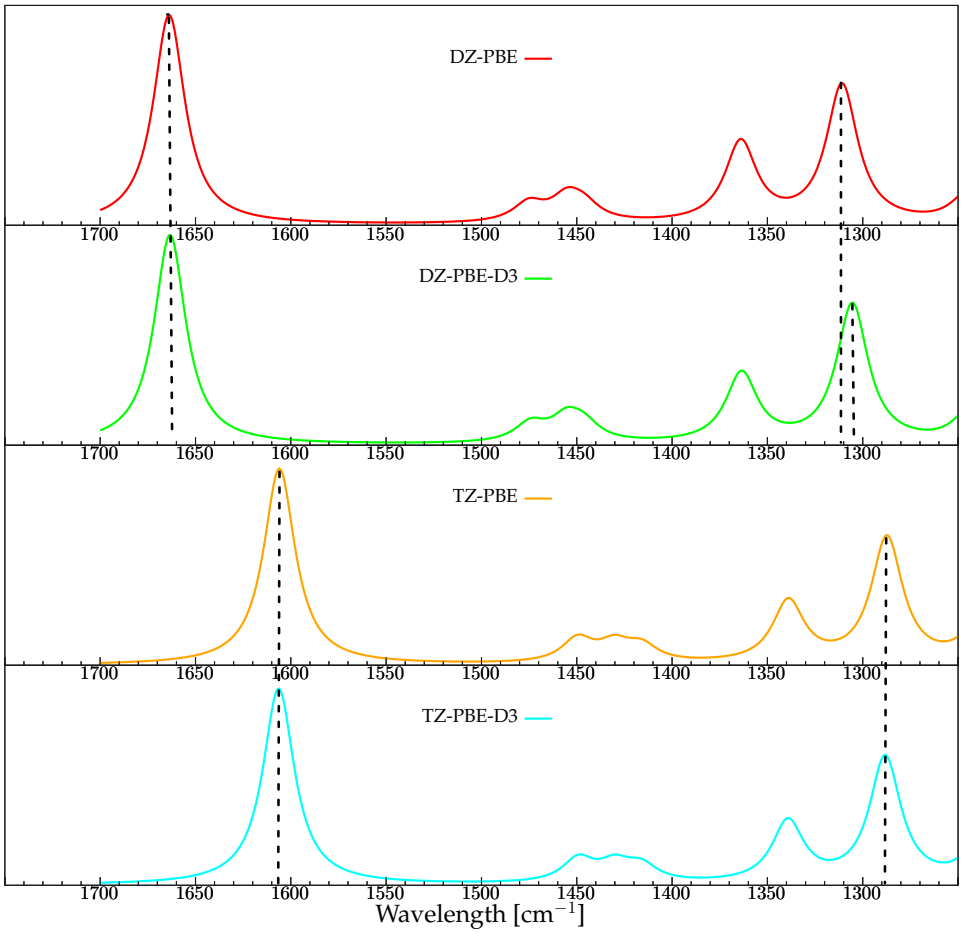

Figure 3.2. Basis set and dispersion correction influence on carboxylate stretching frequency position with PBE functional

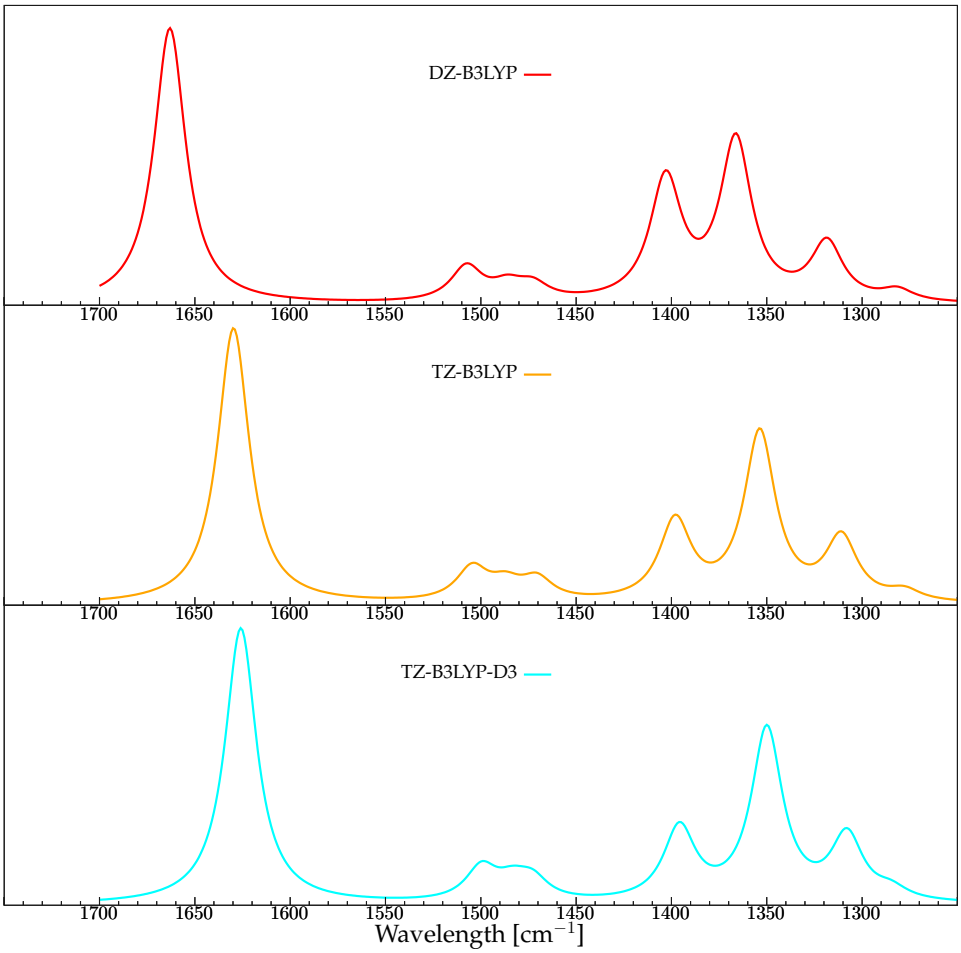

Figure 3.3. Basis set and dispersion correction influence on carboxylate stretching frequency position with B3LYP functional

calculations with different parameters. This is done to display the fact that the position of infrared peaks are strongly dependent on the level of theory used in the MD calculations. Thus, the dynamic frequencies are similar to the carboxylate bands from NMA analysis performed with the same exchange-correlation functional and basis set. At each of these wavenumbers, the dynamic spectrum feature a band of the same intensity in the harmonic case. This is not strictly fulfilled as the bands are slightly blueshifted due to several reasons. First of all, the system is not purely harmonic as the potential of a real molecule is applied. Furthermore, the finite simulation timestep introduces a certain blueshift. The error in the velocity Verlet method makes much smaller timesteps necessary to accurately reproduce vibrational frequencies especially for the high-frequencies region. A common choice for AIMD simulations, which was used for all systems in the present work, is a timestep of 0.5 fs. This is a reasonable compromise between accuracy and computational resources needed for a proper trajectory length. Moreover, the simulation is not fully in equilibrium and some modes carry more energy than others on average.

In particular dynamic spectrum shows that the asymmetric carboxylate stretching vibration carry an excess of energy while the CH_3 bending vibrations are not well resolved. This phenomenon is a general issue of MD simulations of small molecules in the gas phase. If there is only a small number of degrees of freedom and if these groups are not strongly coupled, it takes a long time to exchange energy between them, making it hard to reach equipartition within the time affordable by AIMD.

We additionally have considered the influence of the cut-off value on the position of peak carboxylate stretching frequency. The list of the resulted frequencies for different cut-off values with various basis set is shown in Table 3.3. All the calculations done with PBE functional. The cut-off does not play a significant role on the position of the carboxylate stretching frequency. As it is seen from the Table 3.3, the only difference of about 7 cm^{-1} for both stretching vibrations is found for the case of DZVP basis set. TZVP and TZV2P do not show the sensitivity of the considered frequencies to the increasing cut-off value. As expected, TZV2P basis set shows the closest agreement with experimental value. Although considering the computational cost of such a basis set, it is reasonable to use smaller basis set with appropriate scaling factor.

We then performed the same analysis on the Pivalate anion which closer describes the structure of the tert-butyl ligands in the Synthetic Complex, especially the interaction between three methyl groups and characteristic frequency of this interaction. Figure 3.5 reports the calculated static IR spectra with various functional and basis set choices. The region of the spectra around 1250-1700 cm^{-1} is characterized by symmetric and asymmetric carboxylate stretching at $\sim$ 1320 cm^{-1} and 1630 cm^{-1} for TZ-B3LYP case. The positions of these peaks are red-shifted and blue-shifted from the aforementioned values for TZ-PBE and DZ-B3LYP-D3 levels, respectively. The bands responsible for the methyl bending vibrations are of the same shape and intensity albeit appear at different positions on the spectra. There are two characteristic peaks in the region 1490-1530 cm^{-1} assigned as asymmetric methyl bending vibration. Two peaks appear as well in the region around 1370-1440 cm^{-1} which are assigned to the symmetric bending of methyl group or simply umbrella motions. For the tert-butyl group methyl bending vibrations usually produce splitting of the band because of the vibrational interactions between the several methyl groups of

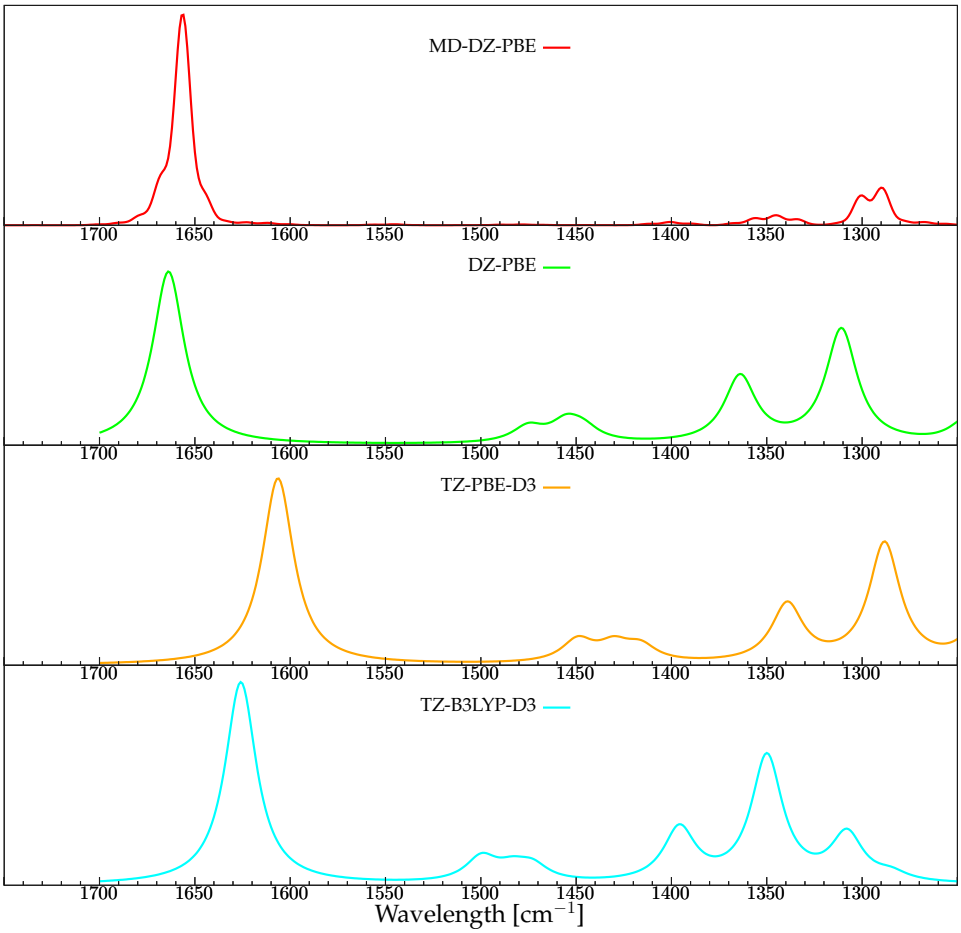

Figure 3.4. Functional influence on carboxylate stretching frequency position comparing to the Spectra decomposition from Molecular Dynamics of Propionate anion

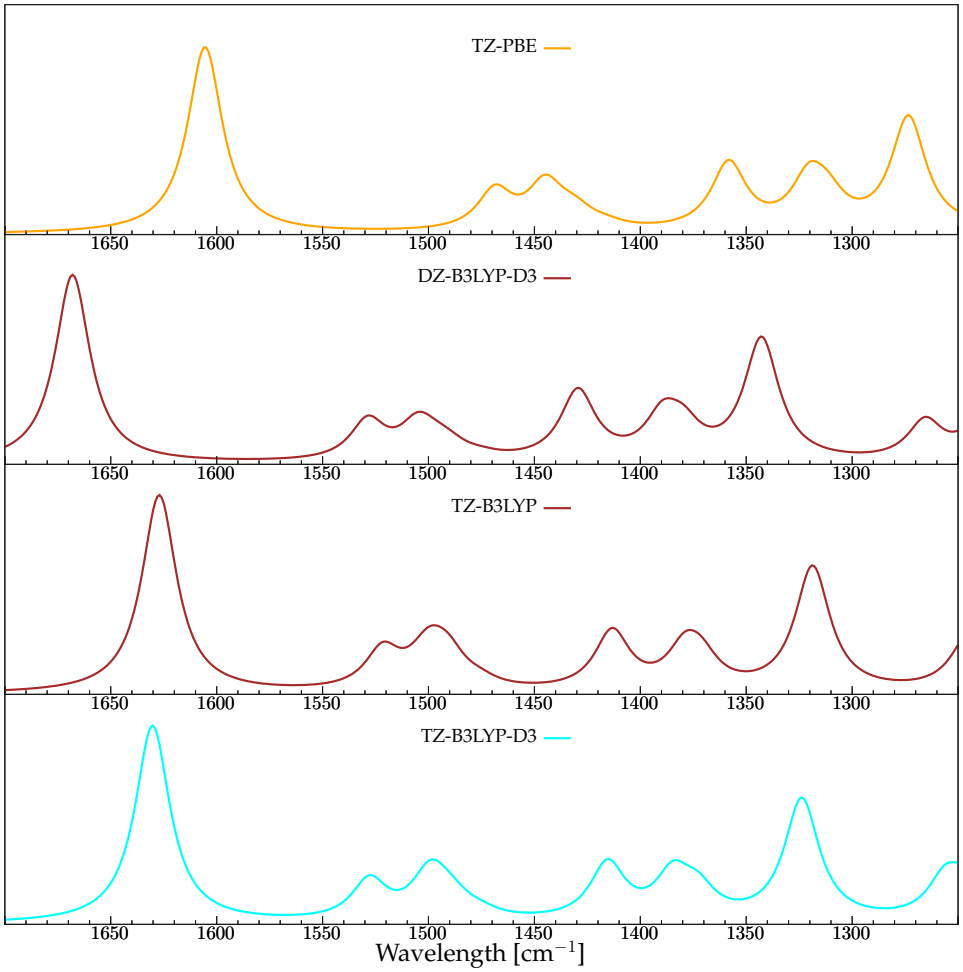

Figure 3.5. Functional and basis set influence on carboxylate stretching frequency position of Pivalate anion

the branch point. The dispersion correction as in the case of Propionate anion did not show significant influence on the spectra, although in this kind of residue the differences are more pronounced.

This systematic study of vibrational frequencies clearly demonstrates that different exchange-correlation functionals may be applied in DFT calculations depending on purposes. It is well known that PBE functional is the best choice for the accurate vibrational analysis [13, 283] and is usually in better agreement with the experimental results than the other popular functionals. Our results for the single carboxylate anions shows that PBE functional actually describes slightly better the frequencies in the considered region especially the asymmetric stretching vibration. But at the same time approaching to better agreement in asymmetric stretching, calculations with PBE functional show the strong underestimation of symmetric frequencies. This lead to the general overestimation of the $\Delta\nu$ value which is one of the important properties for the further interpretation of the results. In accordance with the above conclusions for the vibrational analysis of single carboxylate anions in

gas phase, we have chosen the B3LYP functional with TZVP basis set and dispersion correction as the suitable model chemistry and the best compromise between quality and computational cost for the reliable theoretical interpretation of IR spectra in the region of carboxylate stretching using the NMA analysis. While for dynamic calculations it is rational to use PBE functional with DZVP basis set. The calculated harmonic frequencies for all the systems in present work are scaled by a factor 0.985, which has been found to be appropriate for B3LYP functional and TZVP basis set according to the literature [171, 178, 15].

3.2.2 Carboxylate frequencies region of Synthetic CaMn4O4 complex by Zhang group

An important spectroscopic technique for understanding the behavior of the PSII in the various S_0-S_4 states is the Fourier Transform Infrared (FTIR) vibrational spectroscopy [91]. FTIR difference spectra among the Kok-Joliot cycle states give a picture of the changes occurring between the transitions. Several features can be monitored such as the differences in the H bond network [255], in the Mn oxidation states [92], in their ligands [91, 90], in the O atoms [68, 172] and in the surrounding amino-acids. In this field, a computational approach can be very useful to interpret the experimental spectra and to assign the bands by comparison between experimental peaks and theoretical calculations. [44, 121, 116] The present work aims to interpret and to assign the experimental vibrational peaks of the biomimetic complex and to compare them with the calculated spectra of the natural compound in the S_1 state (Fig. 3.1). In this framework we will perform Normal Mode Analysis (NMA) [284] of the computational model obtained from the crystallographic data shown in Fig. 3.1. The Molden [305, 306] program was used to assign the calculated harmonic frequencies.

Thanks to the availability of the IR spectrum of the Synthetic complex in S1 state at room temperature, we can validate the static and dynamic approaches by means of an accurate interpretation of the vibrational bands. The reliable methods can be then applied to the far more complicated Natural Complex.

As seen from Figure 3.6, the predicted harmonic vibration frequencies and the experimental data are very similar to each other. The most significant discrepancy occurs at symmetric carboxylate stretching vibration, with the largest deviation being 42 cm^{-1} . The spectra presented in Figure 3.6 are calculated at B3LYP-TZVP with D3 dispersion correction level of theory using the constraint on terminal carbons of the carboxylate ligands and a carbon of Pyridine. The fixing of the atoms allowed us to avoid mixing of carboxylate symmetric stretching vibrations with methyl group umbrella motions. In this way, we are able to make the solid assignment of individual peaks for each ligand of the inorganic cluster. In the following section we will show up in details how the spectra are affected by the constraint and compare it with respect to dynamics results. Furthermore, we have compared the vibrational assignments for the harmonic statics and nonharmonic dynamics in order to assess how the modes can be modified by anharmonicities and temperature. In that way, we are able to assess how the harmonic normal modes can be relevant for the interpretation of the vibrational bands that are recorded at finite temperature in the experiment.

In the mid-frequencies spectral region we applied the NMA approach in order to

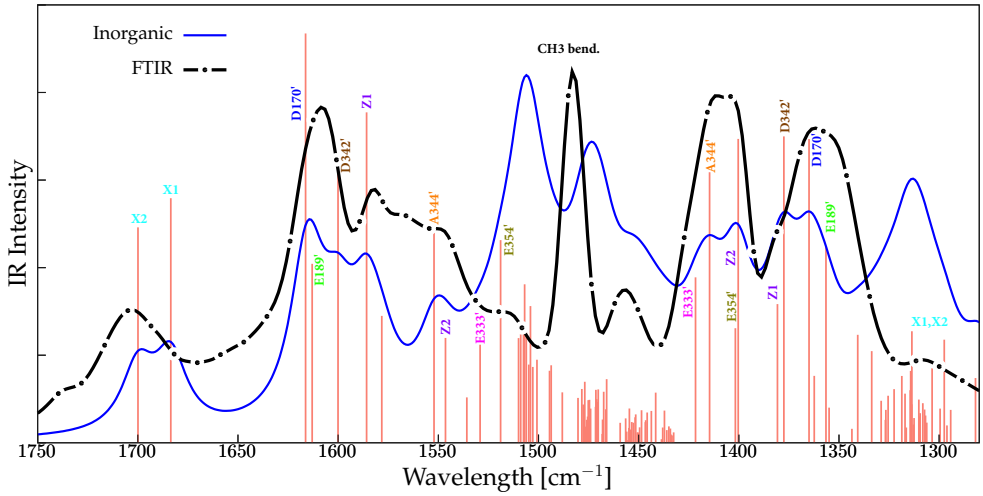

Figure 3.6. Normal Mode Analysis of synthetic CaMn4O4 complex compared to the FTIR data by Zhang et. al.

calculate the molecular vibrations of the models used in present work. In particular, focusing on the modes arising from the cluster ligands for both the Synthetic and Natural complexes, we have been able to identify a specific frequency for each of them. We assigned our calculated normal modes straightforwardly to the measured bands by visual inspection of the calculated Cartesian displacements of the corresponding normal mode for the particular vibrating carboxylate group. Due to intrinsic biases of the theoretical modelling, the computed frequencies are usually shifted with respect to the experimental ones. These systematic discrepancies between the computed and measured frequencies can be compensated by multiply the frequencies by a scaling factor. To choose the proper scaling coefficient for our system we have performed gas phase calculation on several single carboxylate residues (section 3.2). The calculated frequencies for Synthetic complex are scaled by a factor 0.985, which has been found to be appropriate for B3LYP functional and TZVP basis set according to the literature [171, 178, 15].

Specially for the artificial structure we can observe a very good superposition with the experimental data by FTIR on crystallized sample. Looking for an easy comparison with the natural catalyst, in synthetic model the ligands were named after the natural equivalent of binders with primes (see Fig. 3.1). The additional ligands, or the ligands that do not have an analogue in the natural complex were named arbitrarily Z1 and Z2 for the carboxylate ligands, X1 and X2 for the carboxylic residues.

The similar characteristic regimes in intensity and width show up in experiment and calculation. The tentative assignment of the experimental peaks is reported in Table 3.4. Two broad intense infrared bands can be observed extending from 1450 to 1320 cm^{-1}. Variation in the types of carboxylate structures in the sample may be evident as a broadening of the absorption bands, reflecting a sum of individual contributions differing from each other slightly in absorption frequency. Indeed, the stretching bands of the A344' at $\sim$ 1415 cm^{-1}, E333' at $\sim$ 1421 cm^{-1} and Z2 at $\sim$ 1401 cm^{-1} shows up in the experimental peak at $\sim$ 1411 cm^{-1}. Each ligand was

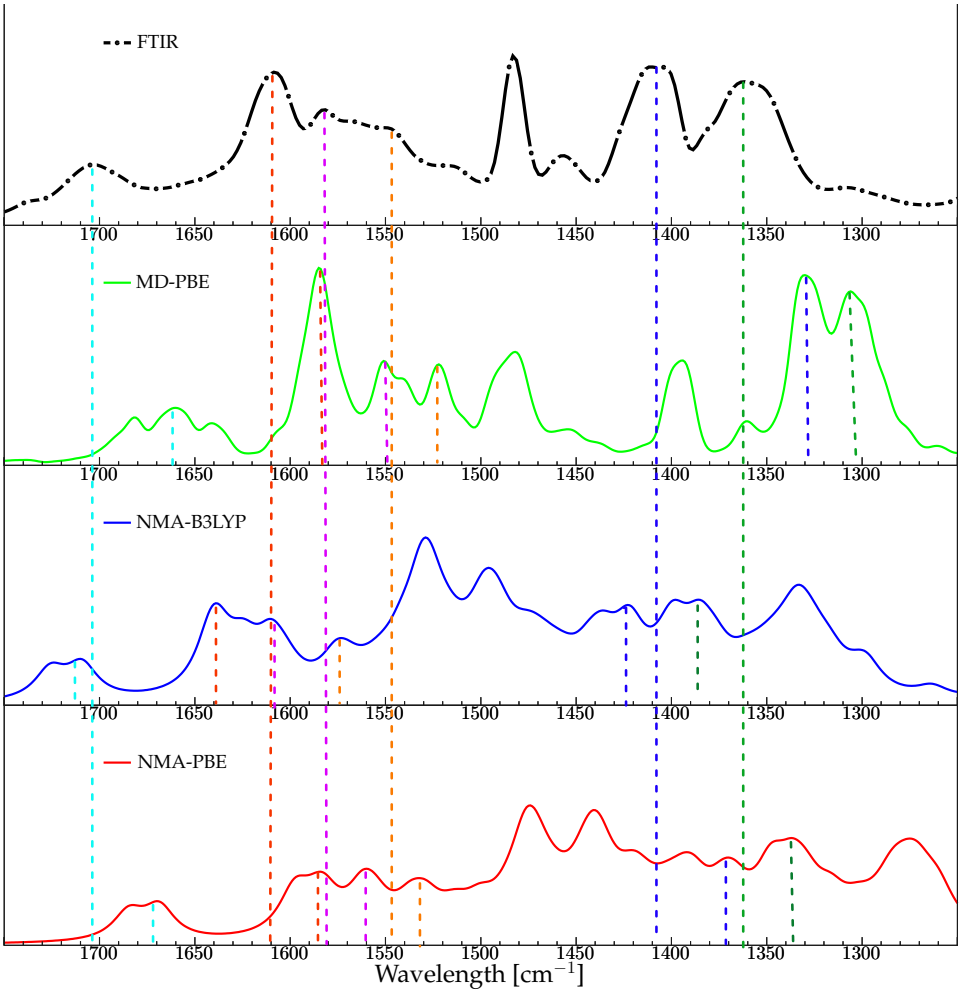

Figure 3.7. Functional influence on carboxylate stretching frequency position comparing to the Spectra decomposition from Molecular Dynamics of synthetic CaMn4O4 complex by Zhang et. al.

Expt.	Assignment
1703	$\nu_{as.}$ (X1, X2)
1608	$\nu_{as.}$ (D170', E189', D342')
1582	$\nu_{as.}$ (Z1)
1548	$\nu_{as.}$ (Z2, A344')
1515	ν_{as} (E354', E333')
1483	σ_{as} (CH_3)
1457	σ_{as} (CH_3)
1411	$\nu_{s.}$ (E333', A344', Z2')
1362	$\nu_{s.}$(D170', A344', Z1, E189', E354')
1306	$\nu_{s.}$ (X1, X2)

Table 3.4. Experimental vibrational frequencies of Synthetic complex [395] with their tentative assignments

assigned to the corresponding peak in the second FTIR band at $\sim$ 1362 cm^{-1} with the contributions from D342' at $\sim$ 1378 cm^{-1}, from Z1 at $\sim$ 1381 cm^{-1}, from E189' at $\sim$ 1356 cm^{-1} and from D170' at $\sim$ 1365 cm^{-1}.

The symmetric methyl bending (umbrella) vibrations occur near $\sim$1375 cm^{-1}, and the asymmetrical bending vibration near $\sim$1450 and $\sim$1483 cm^{-1}. The range of 1375$\pm$10 cm^{-1} is for methyl groups attached to carbon atoms. We can easily observe the splitting of the asymmetric bending band, while the umbrella mode peaks are not well resolved, either due to the modes coupling and/or the lack of conformational sampling in our analysis from the lowest energy isomer.

The region of antisymmetric carboxylate stretching modes is characterized by the presence of the four separated peaks identified in the FTIR spectra: $\sim$ 1515 cm^{-1}, $\sim$ 1548 cm^{-1}, $\sim$ 1582 cm^{-1} and $\sim$ 1608 cm^{-1}. The band at $\sim$ 1515 cm^{-1} was assigned to a superposition of the asymmetrical stretching motions of E354' and E333' ligands, at $\sim$ 1519 cm^{-1} and $\sim$ 1536 cm^{-1}, respectively. The $\sim$ 1548 cm^{-1} band is related to the COO^- stretching of A344' and Z2, while the peak from Z1 ligand could be assigned at $\sim$ 1582 cm^{-1}. The highest intensity band in this region, at $\sim$ 1608 cm^{-1} in our calculation arise from anti-symmetric stretching of D170', E189' and D342' ligands, where the peak at $\sim$ 1616 cm^{-1} is assigned as the antisymmetric stretching of D170' residue, the line at $\sim$ 1600 cm^{-1} comes from the E189' ligand and the carboxylate group of D342' is vibrating at $\sim$ 1586 cm^{-1}. The last peak in this region at $\sim$ 1703 cm^{-1}, as expected, is due to the two protonated carboxylic ligands. Unlike the experimental spectra, the contribution of those two ligands are from two well distinct peaks. The two COOH frequencies are close and appear as a single band in FTIR spectra. The somewhat different arrangements of hydrogen bonds to the carboxylate group could generate some frequency shifts, leading to two distant peaks and consequently splitted band in the calculated spectra. An incomplete resolution of the peak or some symmetric effect of the crystal that is not present in the gas phase model of the system could be another possible reason for appearance of the peaks as two well distinguishable ones.

3.2.3 Effect of mode decomposition from AIMD dynamic trajectory

The advances in computer technology paved the way to employ also ab initio calculations, leading to AIMD with a quantum chemical description of the interatomic interactions. In contrast to a single static calculation of a molecular cluster, an AIMD simulation is not confined to a particular minimum on the potential energy surface, but it samples all molecular configurations accessible in the phase space at a certain temperature.

For the interpretation of the simulated spectra, it is desirable to assign the bands to particular molecular vibrations. While this information is intrinsically available in static calculations within the harmonic approximation as the normal modes of a molecule are the coordinate system in which the Hessian is diagonal, the extraction of normal modes from MD simulations is not straightforward and more complex. Thus we used several different techniques for the mode decomposition directly from MD trajectory, such that the well-known VDOS, ENMA as well as a new IR mode decomposition from dipole autocorrelation function proposed by our group. The latter decomposition approach is based on the correlation function between the i-th dipole and the total dipole. With this approach we were able to reach a clearer assignment of the bands. However, it is worth to note that in the correlation condition negative peaks can appear, and therefore the spectra from this method is less representive of measured IR spectra. The theoretical background of the methods was given in detail in previous chapter.

Fig 3.8 demonstrates the comparison of the methods applied in the present work for carboxylate frequencies region between 1250 -1700 cm^{-1}. The dynamic spectrum is globally shifted towards lower frequencies with respect to the experimental spectrum, with an average red-shift of $\sim$230 cm^{-1} in the region of asymmetric carboxylate stretching and $\sim$260 cm^{-1} for the symmetric vibration of the same functional group. This systematic shift still remain puzzling, it might be entirely fortuitous and due to the DFT PES. However, it remains that upon these shifts the dynamic spectra are globally aligned with the FTIR spectra and provide a fair overall agreement with the experimental signatures. In this way, the dynamic spectra presented in this work are globally translated due to the above mentioned red-shift but there is no scaling factor applied to the dynamic spectra.

Differences observed in the intensities are due to the equipartition of energy, which is difficult to achieve within such a short dynamics scale. Consequently, the corresponding IR intensities of colder atoms involved in active bands are underestimated, while the intensities of warmer atoms are overestimated. Carbon atoms are, on average, the warmest atoms, which is one main reason for the high intensities of the carbon involved modes intensities. Weak intermolecular interactions can also be the reason for the differences in intensities since that restrict a full equilibration of all degrees of freedom.

The present investigation shows that room-temperature dynamics of Zhang biomimetic complex (the temperature of FTIR measurements is 298K) provides a theoretical spectrum that is not in close agreement with the experiment. At the same time worse agreement is achieved with unconstrained harmonic calculations, hence anharmonicities and mode-couplings are appropriately probed in room-temperature

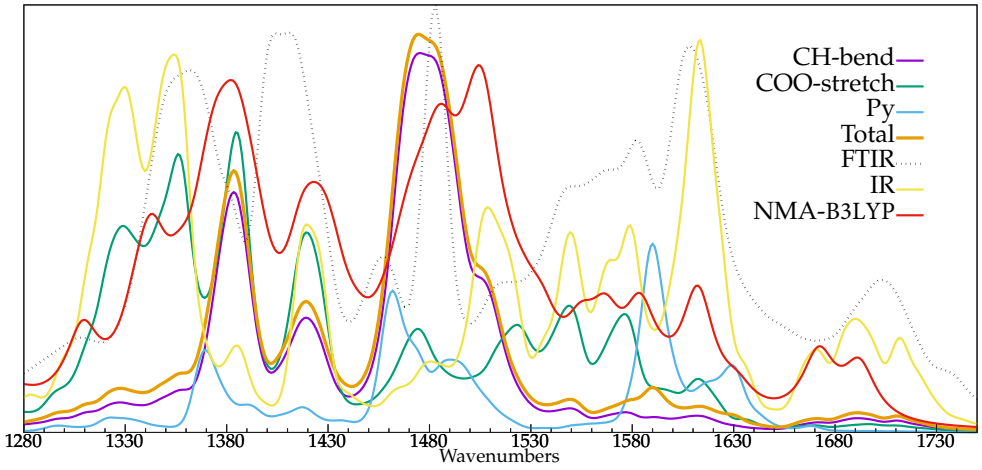

Figure 3.8. Effect of dynamics on vibrational modes in carboxylate stretching region

simulations and can lead to a better agreement with the IR experimental results at room-temperature. It is expected that the relevance of these effects will be even larger for the systems of increasing size and complexity, like OEC of PSII.

Any remaining discrepancies between dynamical and experimental spectra should mainly arise because of the choice of the DFT/PBE functional and DZVP basis set, as DFT-based dynamics are only as good as the functional itself allows. Conformational sampling might be another source of discrepancy: sampling is limited by the length of the trajectories we can afford and the number of initial isomers we are including in the investigation. As it was shown in [118] the conformational space is not fully explored by the gas phase systems at the temperature of the simulation, thus losing relevant information about the real condensed phase system. This behavior was ascribed to too short simulations (10 ps) and/or to the fact that the isolated, non-interacting molecule cannot gather the torsional energy required to overcome the energy barriers between different conformations. Thus, we must take into account further the fact that Zhang Synthetic Complex has three isomeric forms (S1a, S1b, and S1c) [270] which differ in hydrogen-bonding patterns that involve protonated carboxylate ligands (Figure 3.9).

We used the lowest energy isomer (S1c) in all of our calculation, both static and dynamic. The presence of the other two isomers should lead to changes in the H-bond network of carboxylic acid ligands. S1a structure has $anti - anti$ conformations of X1 and X2, therefore has no H-bonds with A344 and O2 atom of the inorganic core. Thereby such a singnificant rearrangement will result in the shifted positions of the peaks associated with the altered residues. At the same time S1b isomer presents *syn* and *anti* conformations and is characterized by the absence of the H-bond with A344. Whereas the most stable isomer S1c has both hydrogen bonds between carboxylic H and O atoms of carboxylato and oxo ligands.

When we try to analyze the spectrum in the 1250-1350 cm^{-1} region, significant differences appear with respect to static results and experimental data. A large red-shift and a significant change of band shape is observed for the COO^- symmetric stretching bands. These variations may result from a coupling of the COO^- symmet-

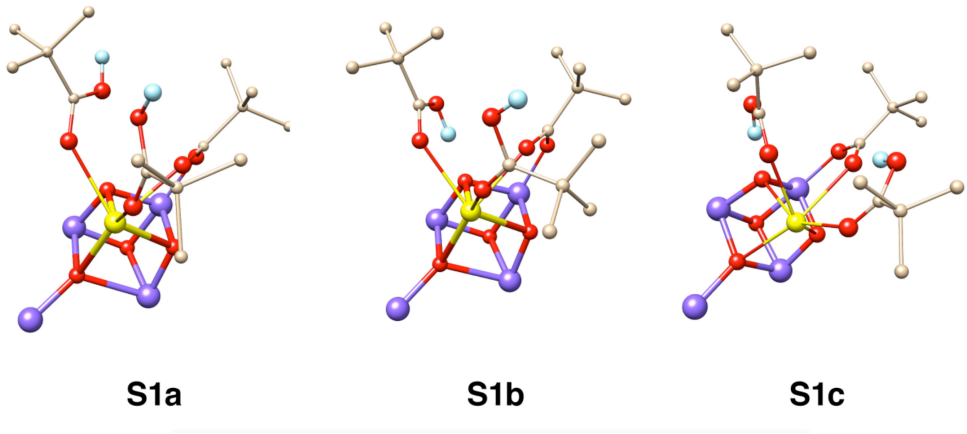

Figure 3.9. Isomeric forms of the S1 state of complex 1, with S1c being the most stable energetically. Most ligands are omitted for clarity. Important hydrogen atoms are indicated in cyan. From ref. [270]

ric stretching with adjacent CH_3 bending vibrations. Additionally, the misplacement of the band can arise from a misrepresentation of the anharmonicities of the potential energy surface of this movement with the PBE functional and DZVP basis set.

Another issue which is observed from dynamics spectra of Synthetic Complex is the strong underestimation of the methyl asymmetric bending vibration. This feature was also found in dynamic spectrum of single propionate molecule (see Fig. 3.4).

Vibrational spectra of molecules in the gas phase are characteristic of the free molecules and exclude any interactions. Each of the molecules may be distorted due to interactions with nearest neighbor molecules in the crystalline phase. This distortion can change the symmetry of the molecule, which in turn can alter the spectral features and can determine a remarkable variation of the intrinsic deformation intensities.

Another reason could lie in the methods intrinsically performed in CP2K package for the calculation of intensities from dipole moments. This in turn can alter the region of coupled vibrations of symmetric carboxylate stretching.

In order to better understand the discrepancies of the COO^- symmetric stretching region, we accurately compared calculated static spectra of the Synthetic complex depending on the presence or absence of the constraint on terminal carbons of each methyl group in the ligands of the metal-oxo cluster. Fig. 3.10 displays the difference of the band shapes and peak positions of two spectra. As expected there is no methyl umbrella motions observed anymore on the NMA spectra with the constraint and this absence essentially affect the bands identified in this region. Due to the strong coupling of the carboxylate stretching and methyl bending vibrations in the unconstrained NMA spectrum, it becomes difficult to distinguish and assign most of the individual peaks of the ligands. In the symmetric stretching region only the bands of D342', D170', E189' and Z1 ligands could be assigned for sure. While the peaks of the rest are delocalized and appear in several regions mixing with umbrella motions of methyl group and COH bending of carboxylic ligands. The asymmetric

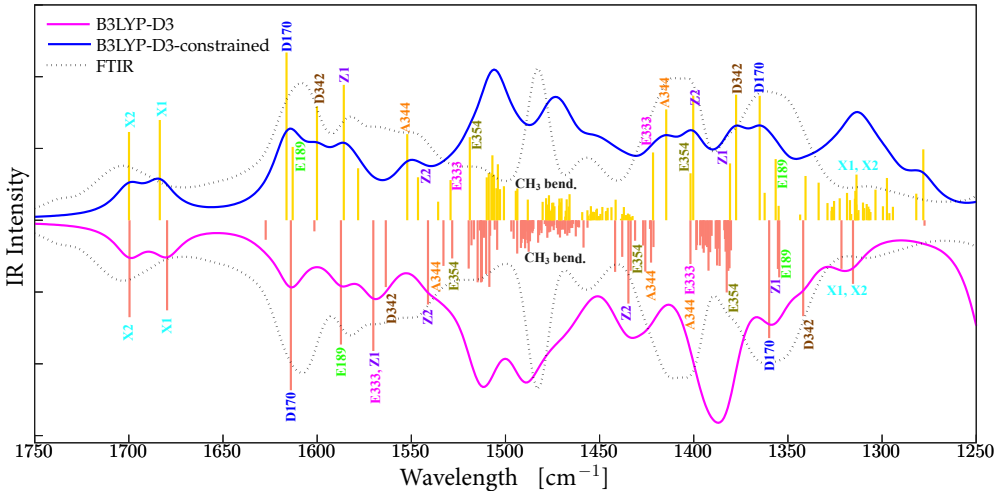

Figure 3.10. Effect of the constraint on terminal carbon atoms in methyl group on NMA band positions in carboxylate stretching region

stretching region is even more complex, since coupling with asymmetric methyl bending lead to the simultaneous vibration of almost all the ligands and strong overlap between their vibrational peaks. Despite the fact that such fixing of the atoms was helpful for the solid assignment of the bands to individual residues, we assume that it becomes essential in the region of our research to take into account the vibrational coupling of the modes for the reliable and accurate interpretation.

To investigate further the reason for the discrepancies in the dynamic spectra, we made the VDOS decomposition separately from the groups of interest. Figure 3.8 reports the power spectrum of the symmetric and asymmetric COO^- stretches, CH_3 bendings, Py vibrations and total calculated VDOS and IR spectra compared to the experimentally observed peaks of the synthetic complex. The assignment of the peaks was performed by analyzing the spectrum of velocity autocorrellation function (VAF). This quantity was projected along the carboxylate, methyl and Py functional groups vibrations separately. In this way we can show the contribution of each mode to the peaks in the considered region.

Nevertheless, the asymmetric stretching region of the vibrational spectra remains almost unchanged and has the same pattern in all the methods. While the symmetric region is rather different from each other and experimental data. This makes the interpretation more difficult. First of all, the NMA analysis shows that the first two shoulder peaks of the spectrum at around 1300 cm^{-1} and 1350 cm^{-1} are due to the two carboxylic acids and five carboxylate residues. The peak at ∼1380 cm^{-1} is due to the contributions from CH_3 umbrella motions, very weak carboxylate stretches and CH rocking motion of Py-ring, while the smaller peak at around 1420 cm^{-1} has contributions from CH_3 umbrella deformations, weak carboxylate stretching vibrations and OH bending of carboxylic groups. The broad band with the peak frequency at ∼1480 cm $^{-1}$ with the lower intensity peak nearby, are both assigned as was said before to the tert-butyl group bending vibrations.

Let us consider now the results from VDOS spectra of different functional groups. The power spectrum of methyl group shows the contribution to the same peaks as

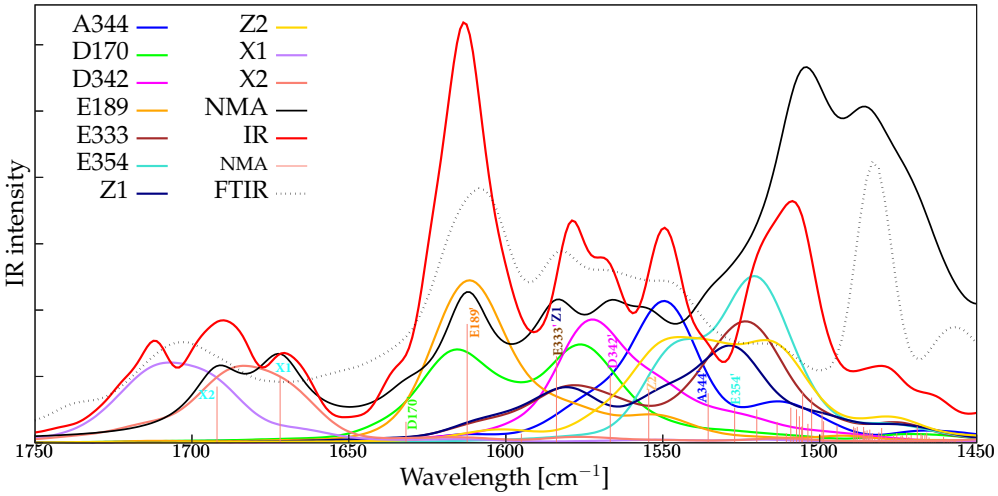

Figure 3.11. Effect of dynamics on vibrational modes in asymmetric carboxylate stretching region

was reported from NMA. At the same time power spectrum from carboxylate group shows contribution to all the peaks observed in the symmetric stretching region, which is again in agreement with NMA assignment. As well the Py-ring vibrations appear at the same place as in the static calculation. When it comes to calculated IR spectrum, we can still observe the same four well-resolved peaks although with different intensities which is expected since different methods use different estimates of the intensities. Thus, we can say that all the peaks observed in power spectra case are IR active.

Although all the spectra show such a good agreement between each other, there is no exact correspondence with the experimental FTIR spectrum. Figure 3.12 presents in detail the region of the IR spectrum between 1270 and 1450 cm^{-1} with the lines from different vibrational spectrum decomposition methods. According to the aforementioned consistency between NMA without the constraint and the other dynamic methods we conclude that for the correct interpretation of the spectra it is mandatory to take into account mode coupling. Therefore fixing the positions of the terminal carbons in methyl groups becomes crucial in this region of the spectra.

Dipole decomposition method allows us to interpret the dynamic spectrum of Zhang Synthetic Complex in the region of carboxylate stretching vibrations. It appears to be rather different from the previous assignment of the bands from NMA with the constraint. The bands in symmetric stretching region from all the carboxylate ligands experiences strong overlapping between each other and lies in a very narrow zone with an overall 70 cm^{-1} width. This calculated band is assigned to the experimental peak at around 1362 cm^{-1}. The second band at ∼1411 cm^{-1} is assigned as the mode coupling of the following groups: methyl group umbrella motion, carboxylate stretching and COH bending of the carboxylic acid ligand. Vibrational modes which often generate bands of relatively minor intensity, such as COH bend or symmetric carboxylate stretch, can undergo significant shifts which, in certain cases, lead to mode coupling and intensity enhancement.

In the asymmetric stretching region only three peaks can be assigned by NMA

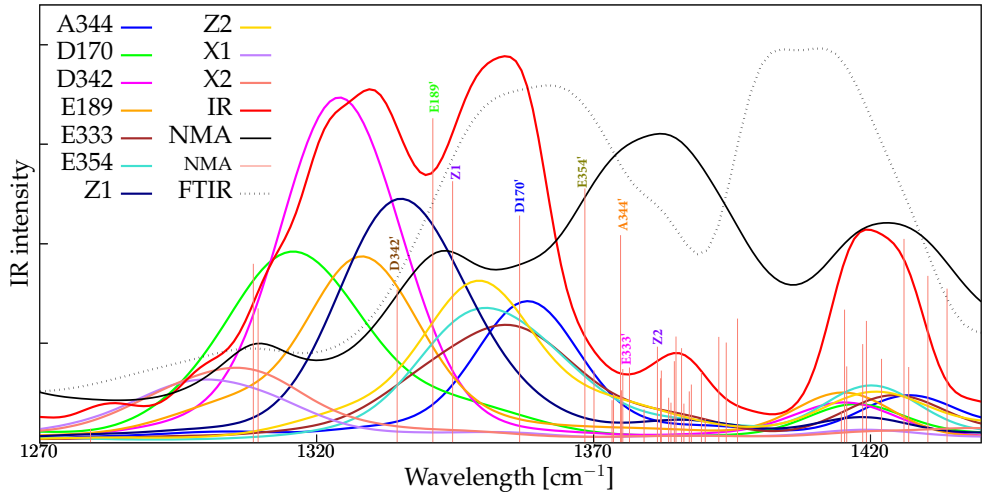

Figure 3.12. Effect of dynamics on vibrational modes in symmetric carboxylate stretching region

without ambiguity for E189, D342 and A344 at around 1583, 1545, and 1522 cm^{-1}, respectively. While the rest of ligands experiences the overlap of the frequencies between each other which results in appearance of several peaks for individual residue. Thus, D170 ligand is characterized by split peak at $\sim$ 1620 and 1615 cm^{-1}. Despite this fact, the region of asymmetric carboxylate vibrations is the better diagnostic in this study because is less susceptible to vibrational coupling than symmetric stretching part.

In addition, strong band broadening in the 1500-1625 cm^{-1} range may be a consequence of non-classical proton sharing. This appears to bring additional evidence of such behaviour when two carboxylate groups share a proton, a feature which has also been invoked recently in a variety of other systems where the proton is shared by two identical or different anionic groups. Dynamical treatment appears to be necessary to model room temperature spectra, including quantum nuclear effects.

It is worth to mention that present theoretical investigation would undoubtedly benefit from a complementary dynamical study where other functionals, including more precise exchange and correlation effects, are taken into account in order to definitely assess the role of the level of theory in misrepresentation of the experimental bands. The objective that we have set for the present work was to give an impression of state of the art "first-principle" computational spectroscopy in the form of an application to the large and representative synthetic complex of biochemical importance.

3.2.4 Low-frequencies region

The low-frequency region of the IR spectrum is mostly originated from the vibrations of the Mn_4Ca cluster and its metal-ligand bonds. This section is dedicated to the analysis of the 350-750 cm^{-1} region of the vibrational spectrum considering the synthetic mimic of OEC in S_1 state. We preferred to use ENMA analysis since it

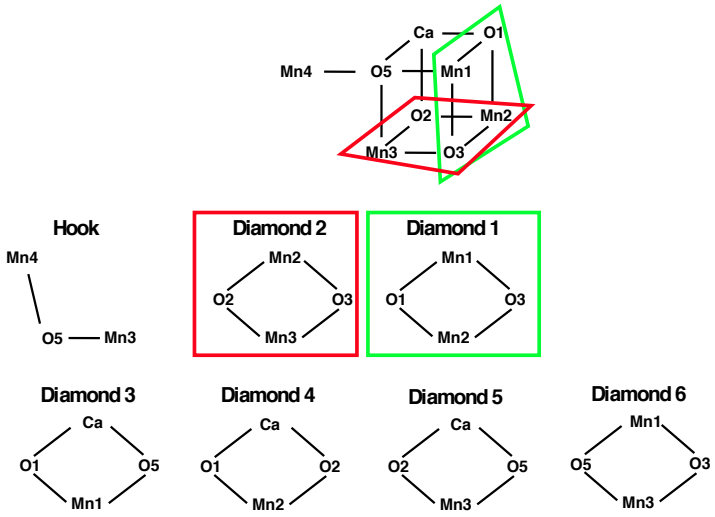

Figure 3.13. Diamond blocks decomposition of the Synthetic Mn_4CaO_4 complex for Effective Normal Mode Analysis.

provides an established procedure to localize the vibrational modes starting from VDOS data, which has been already applied to the S_2 state of PSII [44]. It will therefore make possible to compare the Natural and Synthetic complexes in S_1 state using the same spectral decomposition, to pinpoint similarities and differences in specific vibrational groups.

Following the procedure [44, 348] explained in detail in the Methods section of present work, we decomposed the MnCa cluster in diamonds blocks (as presented in Fig. 3.13, which are therefore used to describe the molecular vibration. For the further assignment we have decomposed the spectra from each diamond by means of ENMA defining the bond stretching, ring deformation and torsion as the internal coordinates [284].

Assignment of the vibrational bands extracted from MD simulations has been achieved with the localization and decomposition procedure developed previously [117] with the associated Potential Energy Distribution (PED) quantification. This procedure goes beyond the VDOS analysis usually performed in the literature. Assignments have been done in terms of nonredundant Pulay internal coordinates. The "effective normal modes" extracted from 298K nonharmonic dynamics take into account temperature and anharmonicities of the dynamics. Using the PED analysis [240] we can clearly assign the bands to the vibrational modes of a specific Mn-O bond (see Fig. 3.14).

As expected, we found that the spectra of the diamonds share some common patterns, due to the fact that a given peak is shared by several moieties, but also

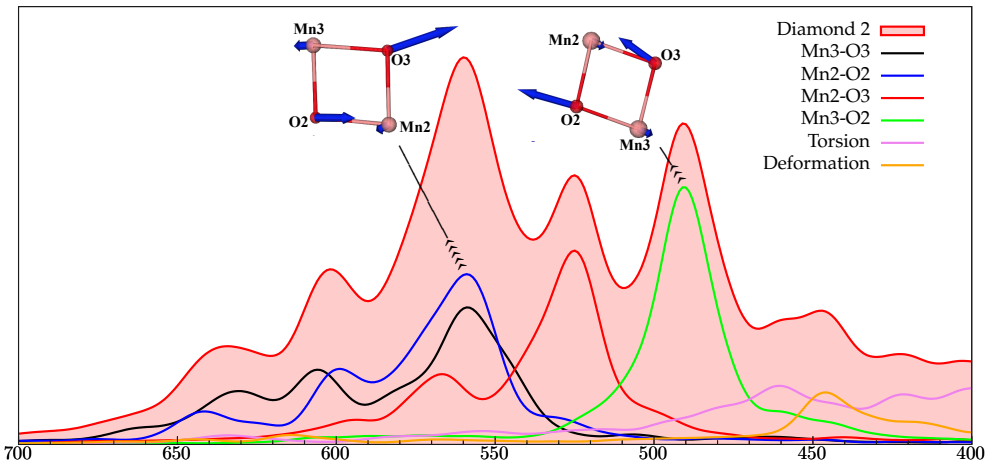

Figure 3.14. Effective Normal Modes and PED analysis for Diamond 2 of the Synthetic Mn_4CaO_4 complex.

presents bands with fingerprints of a specific diamond. As it has been previously clarified [44], we examine the better characterized and more localized Mn–μ–oxo bond stretching modes which are mostly found to be in the region from 450 cm^{-1} to 670 cm^{-1}. The region around 600-610 cm^{-1} of the Synthetic complex at Fig. 3.15 shows contributions from all the moieties except the hook. Diamond 1 contribute to the band at $\sim$ 608 cm^{-1}, assigned to Mn1-O1 stretching mode, while Diamond 2 and Diamond 4 have the secondary peak in this band assigned to the Mn3-O2 bond vibration. Finally Diamonds 3 contribute to this band with the torsion mode identified from PED (75%) which is caused by the previously assigned stretching motion of Mn1-O1. Such a strong coupling in this region is expected since identify the vibration of the inorganic cubane.

Diamonds 1 and 3 have well-defined band at $\sim$ 643 cm^{-1} assigned to Mn2-O1 bond stretching with PED (96%). The other well distinct band we can highlight is presented in Diamond 4 and Hook at $\sim$ 669 cm^{-1} which both contribute to this peak with the Mn3-O5 moiety stretching. Another significant bands with clear and solid assignments are: at $\sim$ 560 cm^{-1} is the band involving the Mn2-O3 bond stretching in Diamond 1 and Diamond 2; at $\sim$ 490 cm^{-1} is the stretching vibration of Mn2-O2 bond from Diamond 2 and Diamond 3, this band albeit less intense is observed in Diamond 4 and assigned as a concomitant torsion of the neighbour ring. We have tried to assign all the 9 Mn-O frequencies to modes which are as much localized in space as possible.

3.3 Chapter Conclusions

Through a combination of AIMD simulations and static NMA, we interpreted experimental infrared spectra of Synthetic Zhang Complex and explored the role of anharmonic effects in this system.

In this thesis, we explored the potentialities and the reliability of different

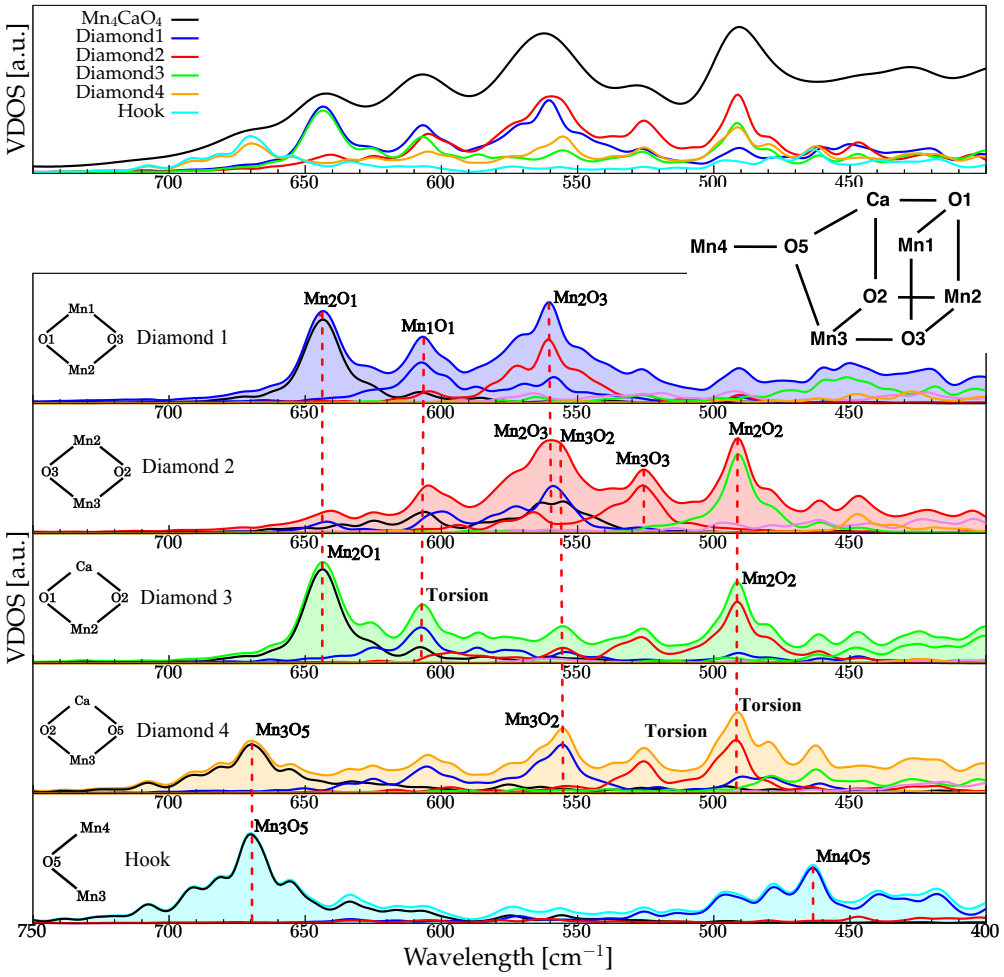

Figure 3.15. Effective Normal Mode Analysis of the Synthetic Mn_4CaO_4 complex in oxidation and spin state of S_1. The overall spectra of each diamond group as well as its decomposition in the contribution of internal collective modes.

state-of-the-art computational techniques for the investigation of the structural and vibrational properties of complex macromolecular materials of biochemical importance. The use of FTIR spectroscopy to probe the structure and function of the OEC complex in Photosystem II has a long history. The synthesis of a very close structural mimic of the catalytic centre has opened up the opportunity to perform a comprehensive and parallel study of both the natural and artificial compounds and of their vibrational modes. Using Normal Mode Analysis in the mid-frequency region (1750-1300 cm^{-1}) we identified and assigned without ambiguity all the relevant peaks of the spectra. The calculation parameters as B3LYP functional with TZVP basis set and dispersion correction are found to be a suitable model chemistry and offer the best compromise between quality and computational cost for the reliable theoretical interpretation of IR spectra in the region of carboxylate stretching.

In summary, our work allowed to unambiguously assign several vibrational peaks of the Synthetic Complex mimicking the Photosystem II reported by Zhang *et al.*[395]. The detailed parallel analysis between the two complexes also provided a comprehensive characterization of the vibrational fingerprints of carboxylate ligands in such class of cubane-like Mn-based compounds. In the light of this characterization we may identify few firm points that should be considered in the interpretation of the spectra as well as the intrinsic limitations and weaknesses of commonly used interpretations.

Our results highlight the advantage of combining traditional normal-mode analyses with AIMD-based vibrational spectra. The normal modes from the static calculations allow for more detailed interpretation of the AIMD results, while AIMD offers a detailed analysis of the role of anharmonicities predicted with the static calculations.

With this detailed account of an application to a single model system, we hope to have presented convincing evidence of the potentialities of ab initio MD based computational spectroscopy. A number of discrepancies and ambiguities remain however. One of the shortcomings in the computed spectrum is a down shift of up to $\approx$50 cm^{-1}. The origin of this bias, which becomes worse at higher frequencies, is related to the choice of the density functional and further technical approximations inherent to the ab initio MD methodology.

Chapter 4

Relevance to Oxygen-Evolving Complex of Photosystem II

4.1 Computational details

Overall, the Natural and Synthetic complexes are rather similar in structure and coordination apart from the two major differences between the systems which are: 1)the total absence of water in the inorganic system, substituted by carboxylate/carboxyl ligands and 2) the lack of the O4 μ–oxo atom in Synthetic complex, that leaves the Mn4 much more flexible in OEC. Furthermore, one of the carboxyl ligands (X2) in the Zhang [395] Synthetic complex ligates the O2 atom as the Arginine D1 (R357) of PSII. Eventually the additional Mn1-Mn4 ligand named Z2 substitutes the H332 presented in the biological system. Those changes induce a contraction of the artificial compound which have shorter intermolecular and intramolecular distances with an exception for the Mn3-Mn4 distance, clearly due to the absence of O4. In particular the most affected distances are the Mn1-Mn4 that is shortened of more than 1 Åand the coordination distance of the E189 analogue, that is closer to the Ca ion and more similar to the other hetero-metal ligand.In general, metal-ligand distances in the Synthetic cluster decreases although the ligands A344' and D342' become slightly farther from the cubane by less than 0.1 Å.

As PS II model we considered a reduced system including the most relevant residues around the Mn_4CaO_5 cluster: the first shell ligands (D170, E189, H332, E333, D342, A344 and E354) and second shell residues (D61, Y161, H190, H337, S169 and R357). In addition, the system contains the four water molecules which are directly linked to the OEC (W2 is a hydroxil) and other ten molecules closest to the cluster; the chloride anion near the E333 is also considered in our model.

Ab initio molecular dynamics (MD) simulations are performed using the density functional theory with the Hubbard correction (DFT+U) approach [11, 101, 100], which is widely used in transition metal systems [220] in order to improve the electron correlation description. The Hubbard U correction for the Mn 3d shell is chosen as U=1.16 eV, as already done in previous works [45, 241, 46, 52]. The Perdew-Burke-Ernzerhof functional [278, 396] is used together with Goedecker-Teter-Hutter pseudopotentials [122, 140, 185] in a mixed Gaussian/Plane Waves approach (Quickstep) as implemented in CP2K package [354]; the chosen basis set is DZVP-

MOLOPT-SR-GTH[353] and the cutoff for plane waves has been set to 320 Ry. Quantum mechanical (QM) Born-Oppenheimer dynamics is performed with a time step of 0.5 fs in NVT ensemble with T=298K for 21 ps. The system is treated in a cubic cell with dimensions of 25.0 × 25.0 × 25.0 Å.

The NMA theoretical calculation is performed using the hybrid DFT Becke-3-Lee-Yang-Parr (B3LYP) exchange correlation functional [26, 327] with corresponding zero damping D3 dispersion correction [127] and TZVP-MOLOPT-SR-GTH Gaussian basis set. Smoothing algorithms (NN50 for the density and NN50-SMOOTH for derivative) were employed to reduce grid effects on the exchange-correlation potential, and the convergence criterion for the OT iterations (EPA-SCF) was set to 10^{-7}. For the exchange we employ a screening threshold of 10^{-12} Hartree and Coulomb operator truncation radius of 10 Å. Furthermore, we apply the auxiliary density matrix method [130] with a contracted cFIT3 basis set for C, O, N, H atoms and SZV-MOLOPT-SR-GTH basis for Mn and Ca atoms for a rapid evaluation of the HFX energy.

4.2 Carboxylate region

We endeavoured to assign the peaks for each of the carboxylate residues in Natural complex using the same procedure as in the case of simpler Synthetic complex. Similarly to the Synthetic complex, two broad bands are shown in the region of the symmetric stretching of carboxylate group. A344, E189 and E333 contribute to the band around 1340 cm^{-1} with the peaks at $\sim$ 1338 cm^{-1}, $\sim$ 1346 cm^{-1} and $\sim$ 1354 cm^{-1}, respectively. The second band is assigned to the other three MnCa-cluster ligands with the peaks at $\sim$ 1396 cm^{-1} from the E354, at $\sim$ 1406 cm^{-1} from D170 and at $\sim$ 1416 cm^{-1} from D342 residue.

The region of antisymmetric stretching modes of COO^- group is characterized by a smaller superposition with other frequencies. The peak at $\sim$ 1540 cm^{-1} is attributed to the vibrational mode of D342. Following that E354 is assigned to the minor peak at around 1563 cm^{-1} while the COO^- stretching of D170 refers to the line at $\sim$ 1575 cm^{-1}. The peaks at $\sim$ 1589 cm^{-1}, $\sim$ 1611 cm^{-1} and $\sim$ 1627 cm^{-1} are attributed to E333, A344 and E189 ligands, respectively.

The comparison of the vibrational properties in Synthetic model with its Natural analogue shows the most relevant differences are on the ligands A344', E333' and D342', in both symmetric and asymmetric modes. The $\Delta\nu$=(ν_{asym}-ν_{sym}) value decreases for more than 100 cm^{-1} comparing to the Natural complex for the ligands A344' and E333' while only for D342' ligand among the others this value oppositely increases for 75 cm^{-1}. Such kind of significant difference could be explained by the essential rearrangement of the surrounding residues. The X2 protonated carboxylate residue directly bonded to A344' in Synthetic complex instead of R357 coordination in Natural enzyme possibly leads to the redshift of A344' frequencies. We can observe strong coupling of methyl umbrella modes, methylene bending modes and ring modes with carboxylate symmetric stretch on the vibrational spectra of Natural Complex. Thus, D342 ligand stretching vibration is coupled to the H337 (ligand of O3 atom in the cubane). The same vibration of E333 ligand is always strongly coupled to methylene bending. Further we will consider in detail how the neighbour

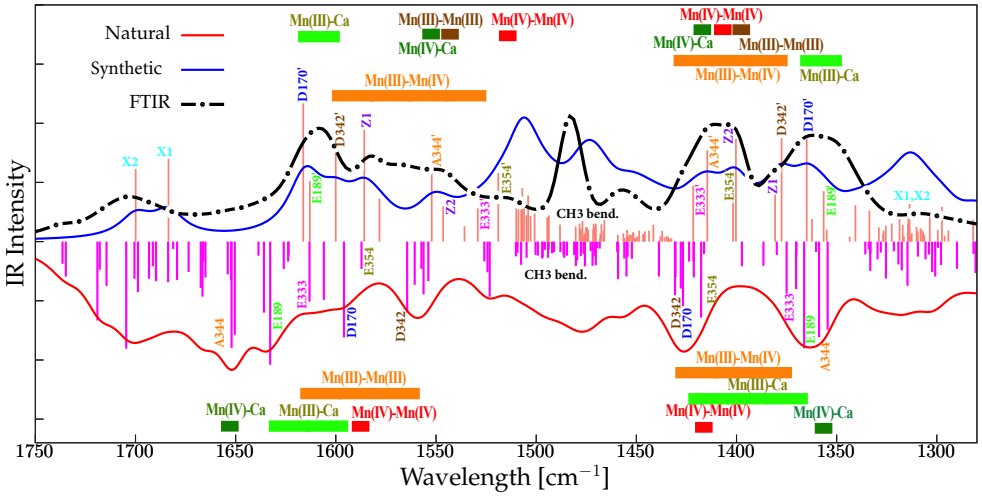

Figure 4.1. Calculated normal mode spectra of the Natural complex with open cubane structure (pink, red) and Synthetic complex with fixed terminal carbons on the ligands and D_3 correction (blue, salmon). We used a scaling factor of 0.985 for the frequencies of synthetic compound. Dashed line in the upper part of the figure is the experimental FTIR data for Synthetic Complex by [395]. The highlights show the region of the moiety vibrations depending on its binding mode and Mn oxidation state.

Residue	$\Delta\nu$ NMA | MD SC	$\Delta\nu$ NMA | MD NC
D170	251 | 294	179 | 199
E189	243 | 278	270 | 351
D342	208 | 247	130 | 168
A344	138 | 188	293 | 289
E354	117 | 167	169 | 161
E333	114 | 167	238 | 163

Table 4.1. NMA and MD frequencies of the symmetrical COO^- stretching vibrations of Synthetic Complex (SC) (B3LYP/TZVP/D3) with 0.985 scaling factor comparing to Natural Complex (NC) with the same parameters

ligands can affect the frequencies of the same residues in two complexes.

Table 4.1 reports the $\Delta\nu$ values for Inorganic and Natural complexes calculated with static and dynamic methods. As it is seen, the frequency shifts and the splitting values are completely system dependent. Thus, we can assume that not only the level of theory is determining the reason for the apparent difference between the two methods but also anharmonicities and temperature effects intrinsically included in dynamic calculations cause essential changes in the positions of the vibrational bands.

4.3 Low-frequencies region

The ENMA decomposition of metal-oxo bonds for Natural complex is shown in Fig. 4.3. For such complex the band assignment is more difficult because of the presence

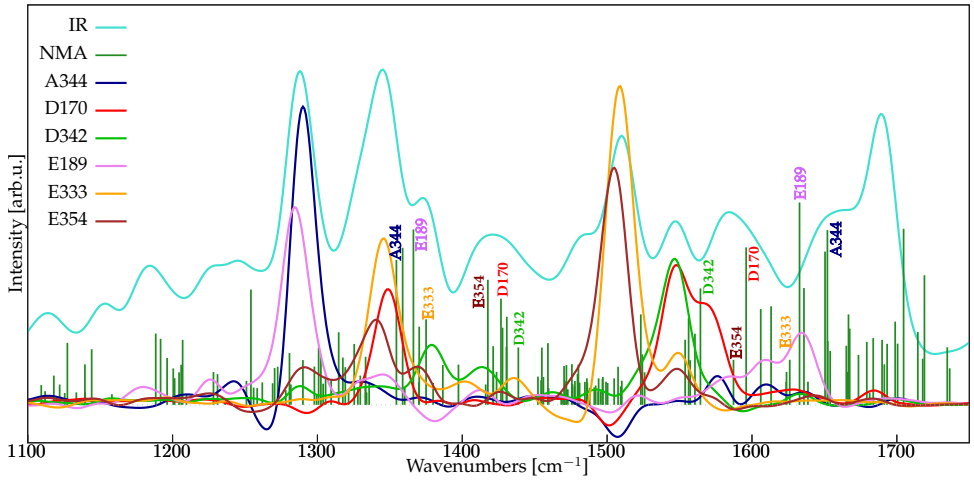

Figure 4.2. Calculated dynamic spectra of the Natural complex (blue line) for individual carboxylate ligands (colored lines) from FT of dipole autocorrelation function in comparison with NMA frequencies (green lines) in the region of carboxylate stretching frequencies

of split peaks in the regions around 600-610 cm^{-1} and 535-545 cm^{-1}. Thus, Mn3-O5 bond stretching has mixed nature and appears simultaneously at several bands (at $\sim$ 605 cm^{-1}, $\sim$ 625 cm^{-1} and $\sim$ 650 cm^{-1}). Similarly, Mn3-O2 bond vibration is found to be at $\sim$ 544 cm^{-1}, $\sim$ 562 cm^{-1} and $\sim$ 578 cm^{-1}. According to the PED data we can robustly assign the following peaks: at 614 cm^{-1} is the intense band both in Diamond 2 and Diamond 4 assigned as Mn2-O2; the $\sim$ 498 cm^{-1} peak is characterized by the contribution from Mn2-O3 bond stretching; at $\sim$ 445 cm^{-1} resonates the stretching motion of Mn3-O3 bond in Diamond 2.

Fig. 4.4 shows the comparison of the calculated VDOS from biological system and artificial cluster together with the low frequency FTIR [395] and IR spectrum of Synthetic complex. It is clear that the calculated spectra are underestimated with the average absolute error of about 17 cm^{-1} comparing to the experimental data,

Mode description	Synthetic [cm^{-1}]	Natural [cm^{-1}]
Mn1-O1	606	604
Mn1-O3	450	541
Mn2-O1	643	580
Mn2-O2	490	614
Mn2-O3	560	495
Mn3-O2	555	544
Mn3-O3	525	445
Mn3-O5	669	650
Mn4-O5	463	609

Table 4.2. Identification of specific vibrational modes of the Mn_4CaO_5 cluster in the S_1 state. The characterization is performed on the basis of the effective normal mode analysis.

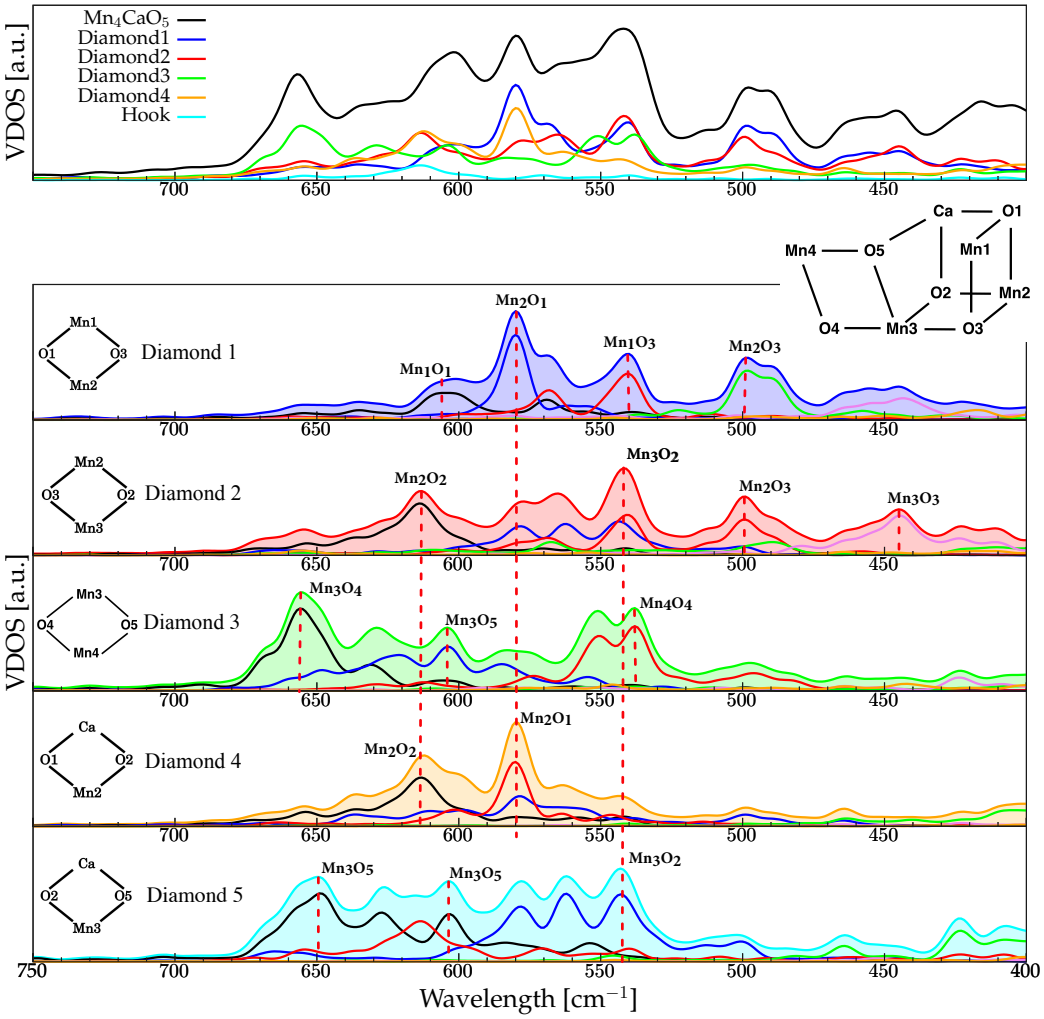

Figure 4.3. Effective Normal Mode Analysis of the Natural Mn_4CaO_5 complex in oxidation and spin state of S_1. The overall spectra of each diamond group as well as its decomposition in the contribution of internal collective modes.

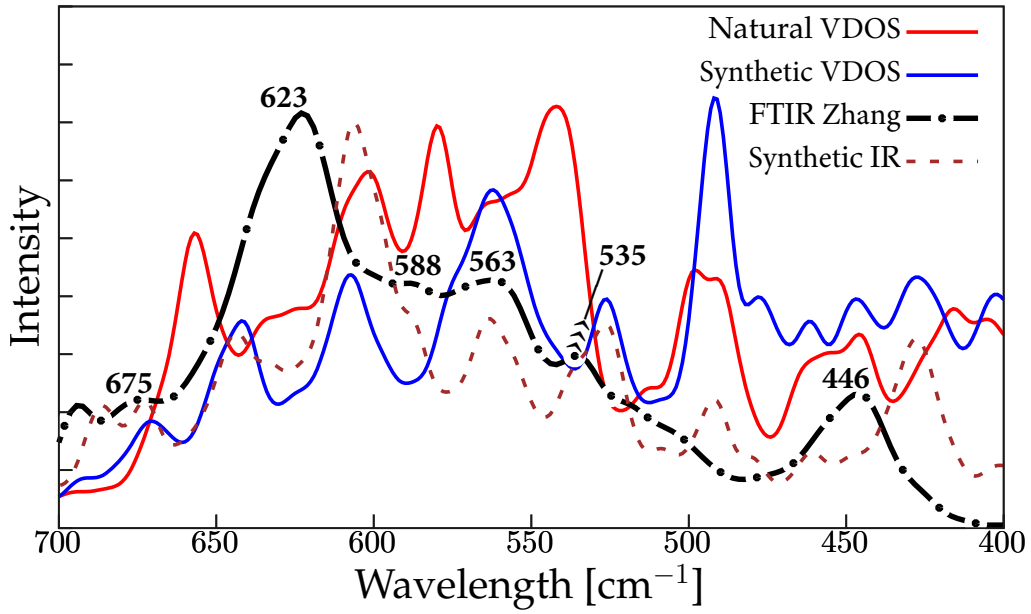

Figure 4.4. VDOS of the Synthetic and Natural clusters from the QM dynamics of S_1 state together with the FTIR data by Zhang *et al.* and calculated IR spectrum of Synthetic complex in the region of Mn cubane vibrations.

at variance with the overestimated result for the mid-frequency region. This kind of shift could arise from the PBE functional and DZVP basis set we used for MD simulation, besides the anharmonic effects usually leading to blue-shifted frequencies. The overall trend in the positions and intensities of the peaks is similar for both complexes, allowing the comparison of bond frequencies between the Synthetic and the Natural complexes. This may indicate the several regions with similar spectroscopic pattern in both complexes at $\sim$ 670 cm^{-1}, $\sim$ 625 cm^{-1}, $\sim$ 560 cm^{-1} and $\sim$ 450 cm^{-1}. It is shown in the experimental study [172] that the bands in the region 670-610 cm^{-1} are sensitive to ^{16}O/^{18}O and H/D exchange thus assigned as Mn-O stretching modes of Mn-O_2 and/or Mn-OH species with bridging oxygen exchanging with water oxygen and interacting with hydrogen. Our results assign the peak around 650 cm^{-1} in Natural complex either to the O3-Mn3-O4 vibrational mode or simply to the Mn3-O5 bond stretching. Surprisingly, experimental peak of the Synthetic complex at around 670 cm^{-1} is assigned to Mn3-O5 vibrational mode as well despite the strong structural differences of the moieties in two models.

The region of the VDOS spectrum at $\sim$ 625 cm^{-1} is characterized by two split peaks from Mn2-O1 and Mn1-O1 bonds vibration whereas in the same region of the experimental and calculated IR spectra one broad band is observed. This band could be approximately assigned to Mn1-O1-Mn2 stretching vibration of Synthetic complex analogously to the previously proposed experimental assignment in the Natural complex [68, 175]. According to this assignment the band at $\sim$ 606 cm^{-1} in S_2 state of OEC is shifted to $\sim$ 625 cm^{-1} in S_1 and reveals sensitivity to ^{18}O and ^{13}C isotope labelling. Based on the differential FTIR results this band was assigned to symmetric stretch of Mn-O-Mn bond involving the O5 μ–oxo bridge. In the same

way for the Natural Complex we can assign the Mn1-O1 and Mn2-O1 modes to the bands appearing at $\sim$ 604 cm^{-1} and $\sim$ 580 cm^{-1}, respectively as the Mn1-O1-Mn2 stretching vibration consistently with the aforementioned experimental suggestion.

The regions of the experimental spectra around 560 cm^{-1} and $\sim$ 450 cm^{-1} although have similar character differ by the nature of the bonds giving rise to the bands in these zones. Thus, Mn2-O3, Mn3-O3 and Mn4-O5 bonds stretching of Synthetic complex appear at around 560 cm^{-1}, $\sim$ 525 cm^{-1} and $\sim$ 463 cm^{-1} whereas in the Natural complex these bands are observed at $\sim$ 445 cm^{-1}, $\sim$ 495 cm^{-1} and $\sim$ 275 cm^{-1}. Oppositely, the Mn1-O3 and Mn2-O2 bonds stretching in Synthetic cluster after the ENMA decomposition appears at $\sim$ 450 and $\sim$ 490 whereas in the Natural cluster the same bond motions are assigned to the peaks at $\sim$ 541 and $\sim$ 614 respectively.

We observe large shift for the Mn2-O2 bond stretching comparing Natural and Synthetic complexes spectra. Its band is localized at $\sim$ 614 cm^{-1} in OEC and moves downward by 124 cm^{-1} in the Synthetic complex. This difference could arise form the positions of the surrounding network of ligands which is deeply changed. Where the Natural complex has R357, the coordination is replaced by carboxylic ligands X1 and X2, where X2 is bonded to O2 atom. Another replacement which could induce strong alteration in the positions of the peaks is the presence of H337 bonded O3 atom in OEC which may led to the significantly shifted ($\sim$91 cm^{-1}) stretching vibration frequency of Mn1-O3 bond. It is worth to note that the band positions of the bonds stretching between all Mn ions and O3 atom are also shifted by minimum 65 cm^{-1} in the case of Mn2-O3. The other area of the synthetic system with strong alteration is around Mn4 which is now bonded to Py and Z2 ligands instead of W1 and W2 water molecules. Furthermore the μ–O4 bridge between Mn3 and Mn4 ions is substituted by Z1 carboxylate ligand bridging same Mn ions. Such a reshuffle leads to the significant shortening of the bonds and upward shift in peak position of the Mn4-O5 stretching mode for $\sim$188 cm^{-1}.

Additionally we need to mention that different orientation of the Jahn-Teller axis in both clusters [270, 318] could possibly be another reason for such an alteration in frequencies of Mn-O stretching mode. This is consistent with the aforementioned difference of the Mn_4-O_5 stretching bands in two complexes.

In a previous paper [359] it was proposed to consider the total number of the μ–oxo bridges as one of the criterion influencing the strength of Mn-O bond. Considering two complexes there are Mn_1 and Mn_2 ions which have the same number of μ–oxo bridges while Mn_3 and Mn_4 ions in Synthetic compound have 1 less μ–oxo bridge due to the lack of O_4 between them. Nonetheless two bonds out of three connected with the Mn_3 ion have very close bond lengths and band positions in both clusters. For Mn_1 and Mn_2 ions in contrast the only bond with close bond lengths and frequencies is Mn_1-O_1. Thereby we believe that the amount of μ–oxo bridges has little role in determining the cluster vibrations, whereas other factors are dominant, such as surrounded residues and Jahn-Teller axis orientation.

Thus the strength of Mn-O bond and therefore the frequency of vibrational modes depends not only on the metal oxidation state but mostly on the character of the bridging ligands and the residues bonded to the oxygen atoms. Consequently despite the fact that Mn_4Ca cores of the both Complexes are structurally very similar, it is not surprising to observe differences in IR spectra between the Synthetic complex

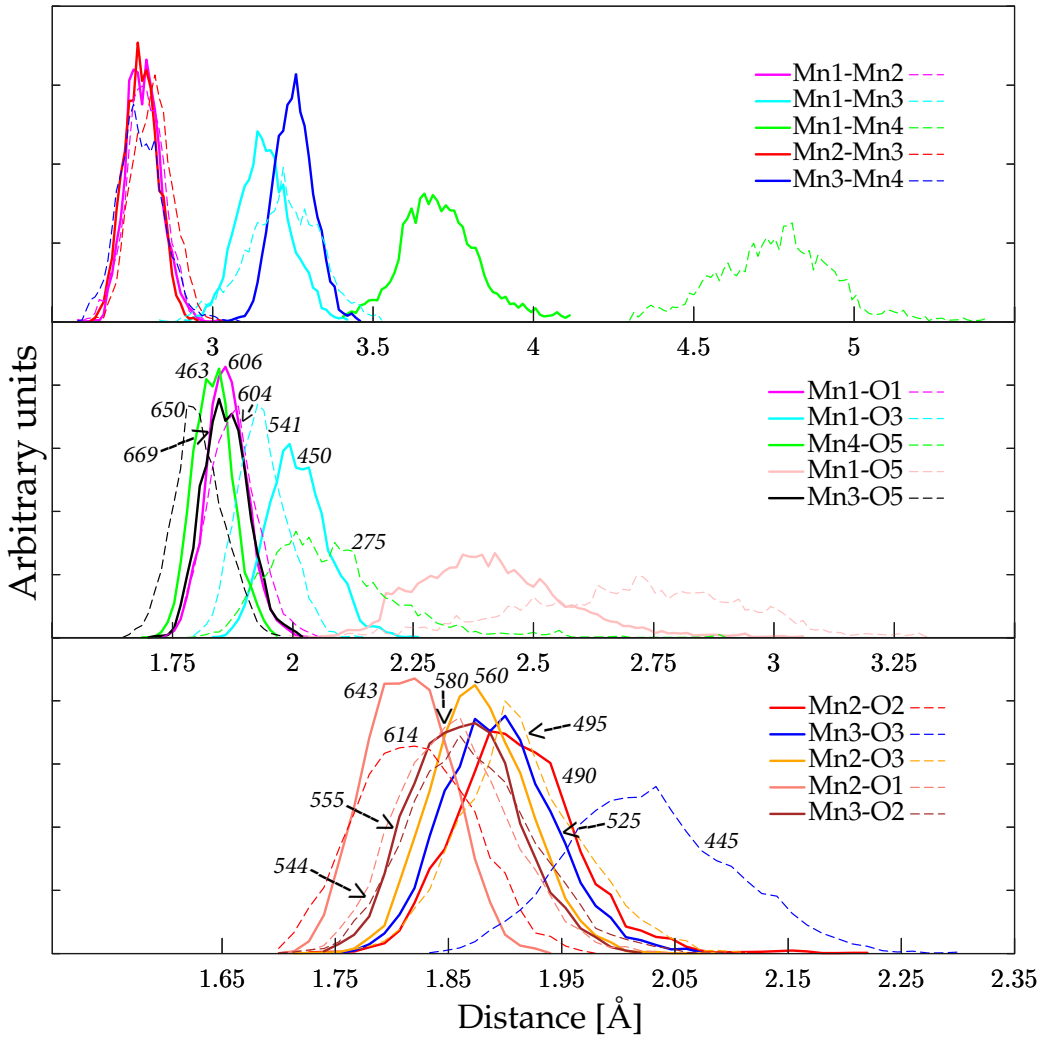

Figure 4.5. Distribution of the selected distances calculated along the MD simulations of Synthetic (solid line) and Natural (dashed line) complexes.

and the OEC. Fig. 4.5 displays the distribution of key distances in both models along the AIMD trajectories in order to indicate the changes in bond strengths and overall positions of the atoms in Synthetic core. It is worth to note that Mn1-O5 and Mn4-O5 distances has a larger distribution (see Fig. 4.5) in Natural complex which is compatible with the more flexible structure of the manganese cubane, responsible for the isomerization between open and closed conformers. The two bottom panels of Fig. 4.5 represent the Mn-O distance distributions along the dynamics. It is shown that the metal-oxo bond length affects the cluster frequencies with the general trend of a decreasing Mn-O stretching band positions at increasing bond lengths. The only exception is Mn4-O5 bond frequency which appears at $\sim$ 463 cm^{-1} although has short Mn-O bond length of 1.84 Å. This is probably due to the increase of Mn3-O5-Mn4 angle for almost 18 ° comparing to the other Mn-O-Mn angles which are around 95-105 °.

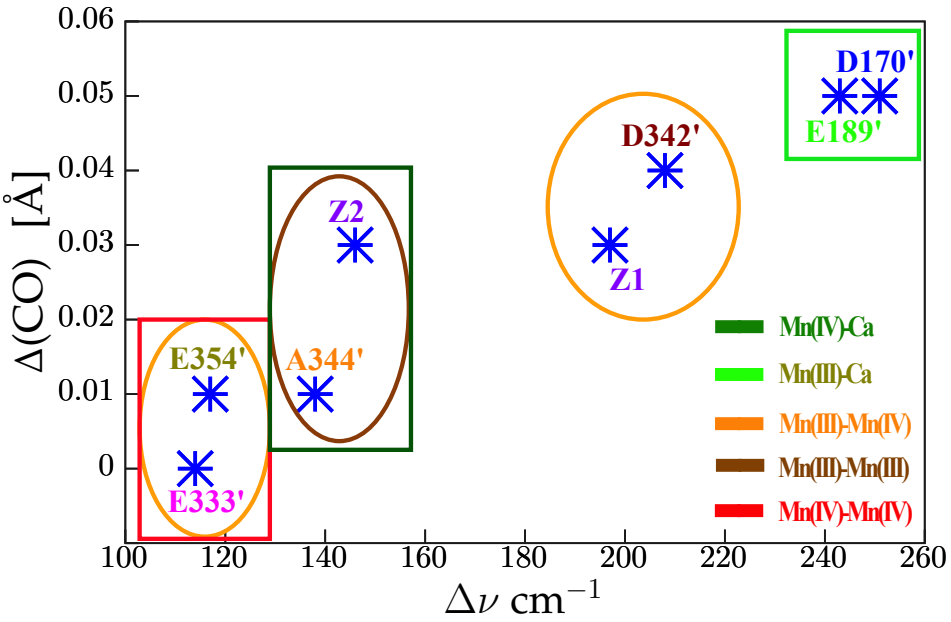

Figure 4.6. Geometric characterization of carboxylate ligands from the positions of CO bond lengths distances d(CO) = [d(CO_1)-d(CO_2)] influence on $\Delta\nu$ values.

4.4 Factors affecting the carboxylate frequencies position

The slight difference is attributed to a change in conformation of the system to reach a more favorable energetic state, and to some degree due to temperature effects.

For both complexes it is possible to specify the ligands related to the bonded metal in the following way:

$$\nu_{s.} : [COOH > COO^{-}(Mn/Ca) > COO^{-}(Mn/Mn)]$$

and :

$$\nu_{as.} : [COO^{-}(Mn/Mn) > COO^{-}(Mn/Ca) > COOH]$$

This tendency is consistent with the distribution of the carboxylate ligands vibration observed in our recent paper [53] for symmetric stretching region in OEC. Interestingly our results are in contrast with the previously observed trend of a decreasing $\Delta\nu$ value with decreasing oxidation states for high-valent dinuclear Mn complexes [31]. The general trend observed for both complexes in the present work is indeed an increasing $\Delta\nu$ with decreasing metal oxidation state. The factors which affect the band positions of the cluster ligands depends indeed more on geometrical properties of the system than on the metal oxidation state, as we can see in Fig. 4.6 by monitoring the CO bond geometries.

Reporting the difference between two CO bond lengths of each ligand, defined as Δ(CO) = d$(CO)_1$ - d$(CO)_2$, we can identify four groups: a) E354', E333' with Δ(CO) $\sim$ 0-0.01 Å ; b) A344', Z2 with Δ(CO) $\sim$ 0.01-0.03 Å ; c) Z1, D342' with Δ(CO) $\sim$ 0.03-0.04 Å ; d) E189', D170' with Δ(CO) $\sim$ 0.05 Å . We use the previously

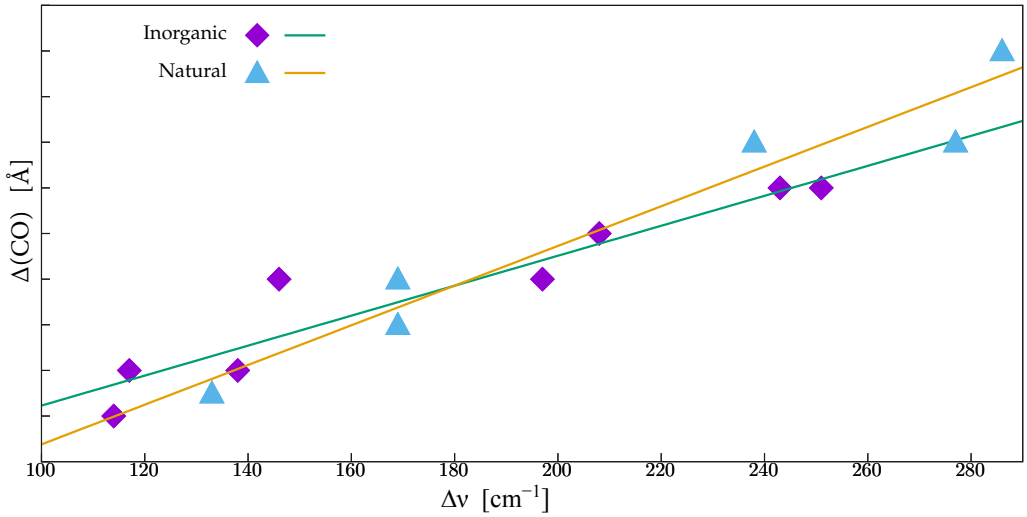

Figure 4.7. Correlation between the positions of CO bond lengths distances d(CO) = [d(CO_1)-d(CO_2)] and $\Delta\nu$ values.

specified color labels of the ligands (see Fig. 4.1) depending on the metal oxidation state in order to show the correlation between different criteria. The region with low $\Delta\nu$ values is populated by different ligands without relationship with oxidation state or bonded metal. Therefore, as the asymmetry of the carboxylate group becomes larger, the frequencies approach to the C=O and C-O stretching modes, respectively, so that their frequency difference increases [238, 337]. The same clear correlation of $\Delta\nu$ value with d(CO) is observed for the Natural complex (as shown in the Tab. 4.3).

For example A344' carboxylate ligand is expected to appear in close vicinity to D170' and E189' considering its oxidation state and coordination to the Ca while the symmetry of the carboxylate group moved it to the low $\Delta\nu$ region. Possible explanation for such kind of behaviour is the difference in residues surrounding this ligand in two complexes. A344' in biomimetic model is characterized by the presence of X2 carboxylic acid instead of W4 water molecule and an R357 in the vicinity of this ligand (see Fig. 1). The second most affected residue is E333' bonded to Mn3 and Mn4, characterized as well by significant changes in the neighbour coordination. W1 and W2 water molecules of the Natural complex are substituted by the Py-ring and Z2 carboxylate group, while another additional carboxylate Z1 is present in Synthetic complex instead of μ–oxo bridge between Mn3 and Mn4. The last ligand with significant change in band positions is D342', bonded to Mn1 and Mn2. The changes consist of 1) Z2 carboxylate on Mn1 in Synthetic complex instead of H332 and 2) stronger μ–oxo bridge between Mn1 and O5. The elongated CO-metal bond length of D342' analogue due to the Jahn-Teller effect on Mn1 ion is an additional reason for such a considerable change in frequencies.

In contrast D170', E189' and E354' ligands have almost unchanged $\Delta\nu$ values in both models. In the case of E354' it is expected to have unaltered band positions since there are no changes observed in the coordination of this residue. When it comes to E189' and D170' which neighbour coordination also heavily changed it is possible to explain the invariability by the fact of the simultaneous replacements on

	Natural Complex				Synthetic Complex			
Ligand	CO-M (Å)	CO-BL (Å)	Angle (°)	$\Delta\nu$ (cm^{-1})	CO-M (Å)	CO-BL (Å)	Angle (°)	$\Delta\nu$ (cm^{-1})
A344	2.42/1.91	1.30/1.24	126.47	293	2.47/1.92	1.27/1.26	124.88	138
D170	2.37/2.15	1.28/1.25	124.58	170	2.36/1.91	1.29/1.24	124.67	251
D342	2.13/2.12	1.27/1.27	124.78	130	2.16/1.91	1.29/1.25	126.18	208
E333	1.96/2.08	1.31/1.25	123.98	238	1.96/2.01	1.26/1.26	125.24	114
E354	2.17/1.99	1.28/1.26	124.99	169	2.00/1.98	1.26/1.27	125.71	117
E189	3.98/2.00	1.31/1.23	123.91	270	2.33/1.93	1.29/1.24	124.16	243

Table 4.3. Comparison of the ligands bound to the Natural and Synthetic Complexes. CO-M is used to indicate the distance from CO bond to metal ions; CO-BL is used as the distance of CO bonds in carboxylate group; Angle represents the angle of COO^- group.

both ligated metals. For instance in Natural enzyme D170 bridging ligand is bonded to Mn4 together with W1 and W2 water molecules substituted in Synthetic complex by Py-ring and Z2 carboxylate showing an elongation of the CO-Mn distance. On the other side the natural ligand coordinates Ca with another W3 and W4 water molecules which are replaced in biomimetic complex by X1 and X2 carboxylic acids induce a higher polarization of the CO-Ca bond. These changes on both metals counterbalance each other and induce no major shift in $\Delta\nu$ values but anyway affect bands positions.

Another relevant reason for the rearrangement in symmetry of the COO^- group is the total absence of water molecules and therefore the very limited hydrogen bond network. As it was shown in the work of Chuah et al. [69], the deprotonation process suppresses the carboxylate stretching intensities during the oxidation. It was also proposed [318, 325] that the presence of water molecules directly coordinated to Ca and Mn4 is playing a significant role in the elongation of Mn1-Mn4 bond which is responsible for promotion of the molecular oxygen formation reaction in the native OEC. Thus the hydrogen bond network is probably a relevant factor influencing the carboxylate frequencies shift.

It is worth to mention that the COO^- group angle (in Tab. 4.3) does not affect the $\Delta\nu$ value of different ligands because of the same bidentate bridging coordination of all carboxylate residues, which lead to the small angle variations within 2°.

As it clearly seen from the Tab. 4.3 the change in coordination mode of the ligands is not the reason for the decrease or increase in $\Delta\nu$. All carboxylate ligands in both complexes are bridging bidentate except the unidentate E189 in Natural enzyme and becomes bidentate in Synthetic complex experiencing the significant shortening of the distance to Ca. However, the change of the coordination mode as well as the CO-metal distance cause only a minor shift of frequencies if compared to the other affected residues.

Another criterium which was proposed as a possible reason for the IR silence of carboxylate residues during oxidation is the ligation along the Jahn-Teller axis on Mn(III) center [325]. In the model complexes considered in present work, the Jahn-Teller axis on Mn4 in synthetic catalyst is oriented perpendicularly [270, 318] to

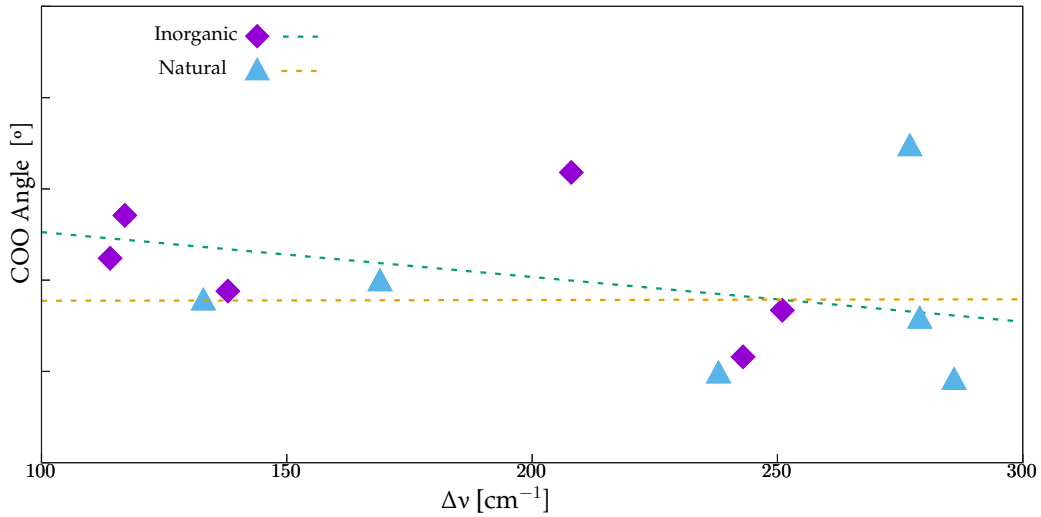

Figure 4.8. Correlation between the angle of the carboxylate group and $\Delta\nu$ values.

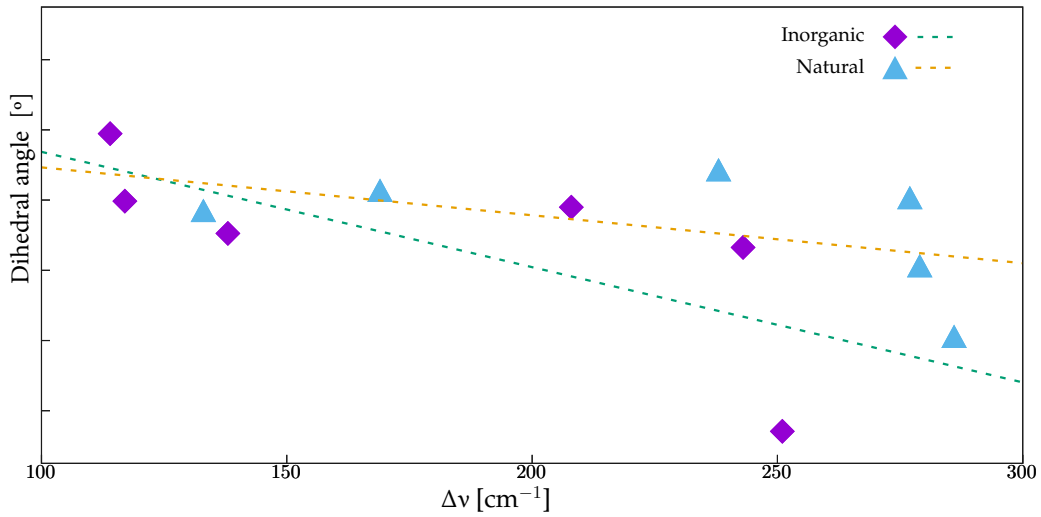

Figure 4.9. Correlation between the dihedral angle responsible for the orientation of the ligand and $\Delta\nu$ values.

the same axis on Mn1 which is in contrast to the collinear orientation of Jahn-Teller axis in Natural complex along the Mn1-Mn4 axis. Nevertheless this difference does not induce any changes on the ligands expected to be affected. Furthermore, D342' is oriented along the Jahn-Teller axis in the same way as in the Natural complex and it experiences significant shift in the frequencies. This conclusion agrees with the result of Berggren et al. [31] that the observed shifts of COO-stretch do not require the ligation along the Jahn-Teller axis and are attributable to the oxidation of directly coordinated Mn ion or to the neighboring Mn ion if the two ions are electronically coupled. We can then reasonably assume that the coordination symmetry of the COO^- group is the main factor controlling the $\Delta\nu$ parameter in Synthetic complex and prevailing over the other criteria like metal oxidation state or denticity of the ligands (unidentate, bidentate, multidentate).

4.5 Chapter conclusions

We have tried to rationalize the results using several geometrical and electronic descriptors. In particular we focussed on the difference $\Delta\nu$ between symmetric and asymmetric stretching of the carboxyl ligands. Our data shows that the Mn oxidation states itself and denticity of the ligands are not capable to catch the $\Delta\nu$ reported by the different ligands, and this might be the reason for misleading interpretations of the experiments. From the structural point of view we have seen that the clearest correlation to $\Delta\nu$ comes from the difference $\Delta(CO)$ between the two C-O bond lengths. This effect is prevailing over the other criteria like metal oxidation state, CO-metal distance, COO^- group angles, orientation of the ligands and their coordination mode. The possible reasons for the changes in carboxylate group symmetry in two complexes are the character of the neighbour ligands and hydrogen bond network. Despite our deep analysis in many case the shift obtained is not clearly predictable by a single electronic or geometric reason.

With the help of ab-initio MD we could identify strong differences in the flexibility of the two clusters, which can be also correlated with differences in the catalytic properties of Synthetic complex. Using the Effective Normal Mode Analysis decomposition from ab initio dynamics for the low-frequency region we observed that the band position of Mn-O vibrational modes depends mostly on the character of the bridging ligands and the residues bonded to the oxygen atoms. Particularly it was shown that the largest band shifts have been observed on such metal-oxo bonds where the ligands of oxygen atom are changed as for O2 atom with protonated carboxylate X2 instead of R357 or for O3 with missed bound H337 residue. Thus, despite the fact that Mn_4Ca cores of both Complexes are structurally very similar, significant differences are reported between the Synthetic and the OEC spectra.

We have also attempted to assign the experimentally determined band at $\sim$ 625 cm^{-1} in oxygen-evolving complex during S_1 state [68] which was previously identified as Mn-O-Mn vibrational mode. Our results suggest the Mn1-O1-Mn2 symmetric stretching as a possible assignment for this band for the Natural complex. The same bond stretching is assigned in Synthetic Complex to the experimentally observed peak at $\sim$ 622 cm^{-1}. In similar way we have tried to assign the peak at $\sim$ 650 cm^{-1} to O5-Mn3-O4 vibratuonal mode in Natural complex and FTIR peak of

the mimicking compound at ~ 670 cm^{-1} to Mn3-O5 mode.

Chapter 5

Electronic structure and properties of Inorganic Complex Mn_4O_4 by Agapie group

Current understanding of the S2 state structure is based on theoretical modelling studies [266, 241, 45] starting from the high-resolution X-ray structures of OEC in S1 state [349, 335] combined with the XAS and EPR spectroscopy available data. Nevertheless, structural and spectroscopic studies of model complexes in S2 state remain rare [229, 228, 270]. As it was discussed in detail in previous chapters, the closest structural mimic of OEC gives rise to two EPR signals in S2 state similar to OEC. Although accurate computational study [270] has found only one energetically valid ground state structure corresponding to the $g \approx 4.9$ signal with $S = 5/2$ form. The second signal was suggested to be associated with an isomerization or rearrangement product. In order to help to understand the discrepancies in the interpretation of EPR spectra of Natural and Synthetic complexes, Agapie and coworkers [196] proposed the systematic studies probing the effect of small structural changes on the spectroscopic and magnetic properties of S2 model clusters.

Their benchmarking results showed that the electronic structure of tetranuclear Mn complexes is highly sensitive to small geometric changes and the nature of the bridging ligands. This has been demonstrated upon systematic changes in bridging and terminal ligands of the series of Mn4 cubane model complexes. Three complexes (Fig. 5.1 in their one-electron oxidized forms had the following differences: a) the first complex, 2-ox, with phosphinate-bridged cubane complex $[Mn_4O_4(Ph_2PO_2)_6]^+$; b) the second, 3-ox, with $n-propyl$-linked diamidate bridging ligands $Mn4O4(diam)(OAc)$; c) the third, 4-ox, with diamidate-benzoate ligands $[LMn_4O_4(diam) - (OBz^{CF3})]^+$.

Present chapter is dedicated to the theoretical investigation of structural and electronic properties of 3-ox synthetic Mn_4O_4 model complex spectroscopically mimicking the S2 state of OEC. This complex is characterized by an npropyl-linked diacetamide proligand (H2diam) replacing two acetate moieties. The n-propyl-linked diamidate serves as a bridging ligand across two faces of the $[Mn_4O_4]$ cubane moiety, resulting in a pseudo-C_S symmetric complex. The oxidation of the precursor complex was performed with the Ag(OTf). The oxidation state of Mn(3) is assigned as MnIII

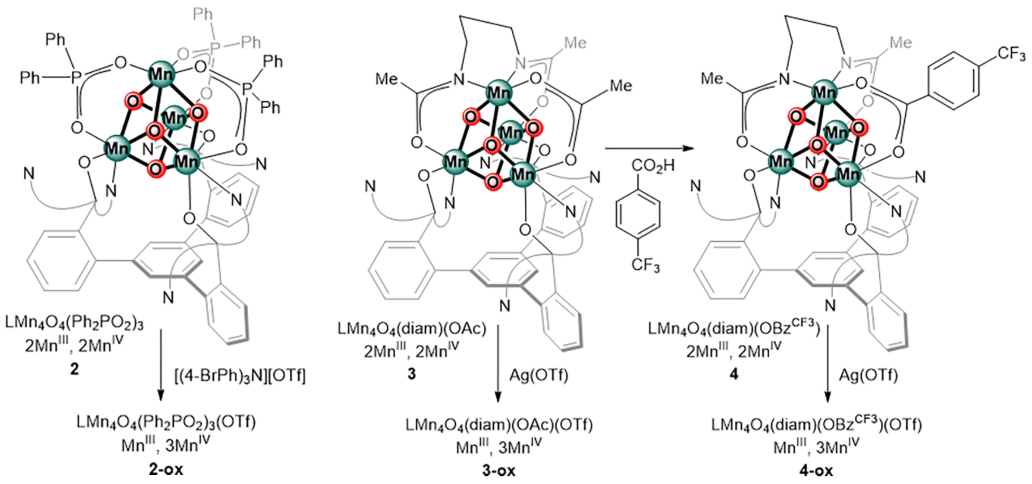

Figure 5.1. Synthetic complexes as spectroscopic models of S2 state of OEC by Agapie et al. [196]

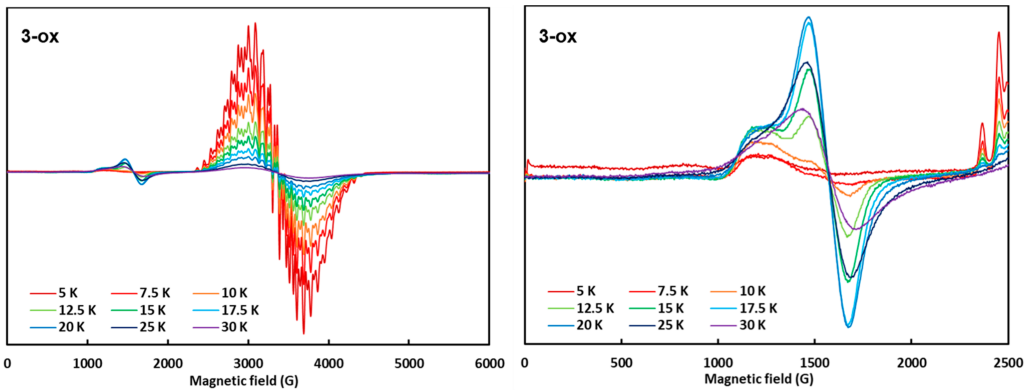

Figure 5.2. (Left) Variable-temperature X-band continuous-wave EPR spectra of 3-ox. (Right) Expanded view of the low field (g > 2) region. Adapted from Agapie et al. [196]

in 3-ox. The elongation of Mn3–O3 distance of 2.051(4) Å is observed, while all other Mn–oxo distances are in the range of 1.893(4)–1.937(4) Å , that is consistent with the $MnIIIMn_3IV$ oxidation state assignment.

For the EPR spectrum of 3-ox at 5 K, only the multiline signal centered at g = 2.0 is discernible. As the sample is warmed, the signal at g = 2 decreases in intensity as a signal centered at g = 4.2 gains intensity (Figure 5.2). In the case of 3-ox, the two signals arise from different spin states of a single, structurally static species. The temperature dependence of the EPR spectrum of 3-ox can be explained in terms of small differences in the Boltzmann distribution of the ground and excited states.

5.1 Broken-Symmetry DFT

A fictitious pair of ferromagnetically coupled site spins can be suitably described by a single Kohn-Sham determinant. In a situation where the fictitious spins

are antiferromagnetically coupled multideterminant behaviour is displayed which consequently requires a multideterminant wavefunction in order to provide a correct description of the system.

The correct description of antiferromagnetically coupled systems would require the use of correlated ab initio multireference methods. However the computational costs arising from describing moderately sized systems with these methods is demanding. Broken Symmetry DFT (BS-DFT) is a technique that can be used to bypass the need for a multideterminant approach by using a single determinant broken symmetry solution.

The idea of BS-DFT is to start from a single determinant that displays the correct antiferromagnetic character but possesses the wrong spin symmetry as seen in Eq. 5.1 below.[243]

$$\Psi_{BS}^{guess} = |(\text{core})\varphi_A\bar{\varphi}_B| \tag{5.1}$$

Where (core) signifies all the doubly occupied orbitals, while φ_A and $\bar{\varphi}_B$ are singly occupied orbitals with the overscore signifying orbitals occupied by spin down electrons.

While it is obvious that wavefunctions which take the form seen in are not able to describe the antiferromagnetic coupling correctly, application of the variational principle enables the arrival at the true broken symmetry wavefunction which is comprised of the reoptimised orbitals (core)$'$, φ'_A and $\bar{\varphi}'_B$ [242].

$$\Psi_{BS} = \left|(\text{core})'\varphi'_A\bar{\varphi}'_B\right| \tag{5.2}$$

Calculation of the Heisenberg exchange coupling constant serves to connect the energies obtained from BS-DFT calculations to the spin Hamiltonian description. J is denoted as Heisenberg exchange-coupling constant and describes the magnetic coupling of localized spins within the Heisenberg-Dirac-van Vleck (HDvV)-Hamiltonian:

$$\widehat{H}_{HDvV} = -2J\hat{\vec{S}}_A\hat{\vec{S}}_B \tag{5.3}$$

where $\hat{\vec{S}}_A$ and $\hat{\vec{S}}_B$ are spin operators on different centers in a dinuclear (sub-)system. Accurately calculating the Heisenberg exchange coupling constant requires reliably calculated energy differences of the various spin states involved. Multiconfigurational computational techniques are able to calculate the exchange parameters; however they are hindered by the large computational cost required for the calculations. BS-DFT provides a way to surmount this multideterminant requirement and allows for the calculation of the exchange coupling constants.

For dinuclear systems, the expression seen in Eq. 5.4 suggested by Yamaguchi and coworkers may be used to calculate the Heisenberg exchange coupling constant in BS-DFT calculations.[295]

$$J = -\frac{E_{HS} - E_{BS}}{\left\langle \hat{S}^2 \right\rangle_{HS} - \left\langle \hat{S}^2 \right\rangle_{BS}} \tag{5.4}$$

Here, E_{HS} and E_{BS} denote the energies of the high-spin and broken-symmetry states, respectively, and $\left\langle \hat{S}^2 \right\rangle_{HS}$ and $\left\langle \hat{S}^2 \right\rangle_{BS}$ are the corresponding expectation values of the spin squared operator.

The total number of magnetic interactions J_{ij} in exchange coupled systems containing n spins S_i is equal to the number of possible pairwise combinations constructed from these spins, e.g. four spin centers (in case of the OEC) lead to six magnetic interactions. The total number of distinct spin configurations is 2^{n-1}, given the equivalence of configurations that are one-to-one spin-inverse. The parameters J_{ij} are then found from the solution of a system of 2^{n-1} linear equations within the framework of the Ising approximation:

$$E\left(S_K\right) = -2\sum_{i<j} M_{S,i} M_{S,j} J_{ij} \tag{5.5}$$

with

$$M_{S,i} = \pm S_i \tag{5.6}$$

and

$$\sum_{i=1}^{n} M_{S,i} > 0, K \tag{5.7}$$

The series of equations 5.5 is overdetermined (n linear independent equations with $\sum_1^{n-1} a_i$ variables cannot be simultaneously exactly satisfied) and therefore a least-squares fit or singular value decomposition [124] is used to find the optimal solution.

5.2 Computational details and results

The full structural model of 3-ox was used for geometric and electronic structure calculations. Crystallographic coordinates of the Synthetic complex 3-ox were used as the starting geometry except for the wrong additional hydrogen atom (index of H atom is 18) on one of the Py-ring (we have contacted prof. Agapie and he has specified that they missed one hydrogen during the manual check of the system). The model includes a solvent dicloromethane molecule and OTf^- counterion. All structures have the same valence state distribution of the Mn ions (4434). All calculations used the ORCA and CP2K packages. Full optimisations were performed in total HS and selectively in some of the BS states with PBE+U, B3LYP, TPSSh functionals.

The broken-symmetry approach has now been established as a practical tool especially for transition metal complexes and metalloproteins [1, 383, 256, 4]. By the proper selection of the DFT functionals, the geometric structures and magnetic properties can be well reproduced at the BS level. We used several different functional/basis set parameters reported as well suited for the geometric optimizations and magnetic interaction calculations, such as TPSSh/def2TZVP, B3LYP/TZVP and PBE+U/DZVP [46, 270, 318].

The single-point energies of all BS states (including HS) were calculated. In the second step, using these energies and the calculated values of S^2 we obtain the coupling constants J following eq.5.5. In the third step the HDvV spin Hamiltonian

BS state	$(2S+1)$	S_z	$\|m_1, m_2, m_3, m_4\rangle$
Ψ_1	14	13/2	$\|+3/2, +3/2, +2, +3/2\rangle$
Ψ_2	8	7/2	$\|+3/2, -3/2, +2, +3/2\rangle$
Ψ_3	8	7/2	$\|-3/2, +3/2, +2, +3/2\rangle$
Ψ_4	8	7/2	$\|+3/2, +3/2, +2, -3/2\rangle$
Ψ_5	6	5/2	$\|+3/2, +3/2, -2, +3/2\rangle$
Ψ_6	2	1/2	$\|+3/2, -3/2, +2, -3/2\rangle$
Ψ_7	2	1/2	$\|-3/2, +3/2, +2, -3/2\rangle$
Ψ_8	2	1/2	$\|-3/2, -3/2, +2, +3/2\rangle$

Table 5.1. All possible BS spin states for the 3-ox complex

was constructed and diagonalized to generate the spin ladder based on the calculated J values in eq. 5.3.

We used the ORCA package to perform calculations with hybrid TPSSH with the following key parameters. ORCA significantly speed up hybrid functional calculations due to the several tricks, like 'chain-of-spheres exchange' (COSX) approximation of Coullomb and exchange parts of Fock matrix, implemented in the package. Scalar relativistic effects were included through the zeroth-order regular approximation (ZORA), [351, 350] retaining one-center terms and using ZORA-recontracted def2-TZVP basis sets [367] for all elements except C and H, for which ZORA-SVP basis sets were used. All calculations used the dispersion corrections proposed by Grimme, with Becke-Johnson damping [127, 128]. Increased integration accuracy (Grid6, GridX8 and IntAcc 6.0 in the ORCA convention) and tight self-consistent field convergence criteria were applied. We have performed the calculations both without CPCM and with the dielectric constant value equal to 8.5 according the solvent effect used in EPR measurements (1:2CH_2Cl_2:2-Me-THF).

At the same time, CP2K package has shown the best speed for GGA functionals. For the calculations with PBE functional we have used the D3 dispersion corrections and 10^{-5} SCF parameters together with the DZVP basis set and the Hubbard correction U=1.16 eV. Periodic calculations in CP2K have been done using the crystallographic data from the experiment for the unit cell with triclinic symmetry consisting of 2 asymmetric units. The Mn labels are the same as in the experiment and article [196]. Periodic calculations have been done at PBE+U level of theory with the same parameters as for the gas phase case.

BS states for the model are generated in CP2K by the broken symmetry section of the input file putting the right number of electrons on the alpha and beta orbitals of the selected d level for each Mn atom. While ORCA BS solutions are generated by inverting the local spin of individual Mn ions using the "Flip Spin" feature of the package. Table 5.1 lists the spin states in Dirac's representation, for the electron configurations of 3-ox model.

We were able to converge the system with the same spin scheme as in the experiment. The system has a strong propensity to put the unique Mn(III) oxidation state on Mn_3 atom in the absence of any changes in geometry. The position of the Mn(III) atom is defined by the Mulliken population analysis. Furthermore it

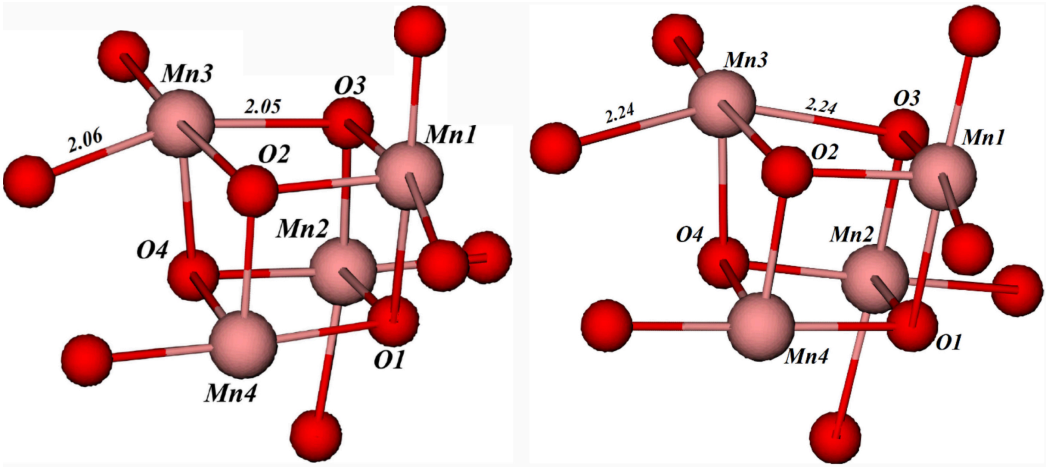

Figure 5.3. Cluster structures of the truncated optimized model with TPSSh functional and ϵ=8.5 (right) comparing to the experimental cluster model (left).

Constant	PBE+U	B3LYP	Exp.
$J_{1,2}$	-31.3	-21.8	-15.3
$J_{1,3}$	23.8	12.09	-8.9
$J_{1,4}$	0.4	0.028	-16.7
$J_{2,3}$	27.3	19.1	-8.9
$J_{2,4}$	30	18.2	-16.7
$J_{3,4}$	5.47	-4.45	-10.6

Table 5.2. Calculated effective exchange integrals (J/cm^{-1} values) of 3-ox in S_2 state with B3LYP and PBE+U functionals comparing with the experimental data from Agapie *et al.* [196]

is observed the Mn_3-O_3 bond elongation by more than 0.1 Å together with the distance from Mn_3 to the unique carboxylate ligand both in the calculation and experiment. This indicates that the orientation of the Jahn-Teller axis is along this elongation.

The strong elongation of Mn_3-O_3 bond distance for about 0.15-0.2 Å comparing to the experimental value is observed in all the calculations using different functionals and basis sets. This bond elongation is the same as for the previous structures with dielectric constant in CPCM model of ORCA equal to 8.5 and TPSSh functional.

In order to exclude the crystal packing effects on the key bond distances of the inorganic core, we have performed periodic DFT calculations with the PBE+U/TZVP level of theory. We have found the BAAB (S=1/2) spin state to be the lowest energy BS state both in periodic and in gas phase calculations with the relative energy lower for about 31 cm^{-1} from the AABA (S=5/2) state and for about 130 cm^{-1} lower than the HS state. The RMSD value for the system in the lowest energy BS state without H atoms is 0.174Å while for the cluster is around 0.11 Å . Bond distances for the model of the complex with different functionals, basis sets and spin states comparing to the experimental values are presented in Table 5.3. Differences

		PBE+U		TPSSh	B3LYP		PBE+U -PBC	
Bond	Exp.	HS	LS(BAAB)	HS ϵ=8.5	HS	LS(BAAB)	HS	LS (BAAB)
Mn1-O1	1.91	1.92	1.92	1.90	1.91	1.91	1.93	1.93
Mn1-O2	1.90	1.91	1.91	1.88	1.90	1.91	1.91	1.90
Mn1-O3	1.94	1.87	1.87	1.84	1.86	1.86	1.88	1.87
Mn2-O1	1.89	1.90	1.89	1.87	1.89	1.89	1.89	1.89
Mn2-O3	1.93	1.87	1.88	1.85	1.86	1.87	1.87	1.88
Mn2-O4	1.90	1.93	1.93	1.90	1.93	1.93	1.91	1.92
Mn3-O2	1.91	1.94	1.94	1.88	1.94	1.94	1.94	1.94
Mn3-O3	2.05	2.25	2.18	2.24	2.25	2.23	2.26	2.21
Mn3-O4	1.93	1.96	1.98	1.96	1.95	1.96	1.97	1.98
Mn4-O1	1.90	1.90	1.91	1.87	1.89	1.9	1.91	1.91
Mn4-O2	1.91	1.93	1.92	1.90	1.92	1.91	1.93	1.92
Mn4-O4	1.90	1.91	1.89	1.88	1.90	1.9	1.92	1.90
Mn1-Mn2	2.9	2.85	2.87	2.85	2.85	-	-	-
Mn1-Mn3	2.95	2.99	2.98	3.0	3.0	-	-	-
Mn1-Mn4	2.78	2.8	2.8	2.8	2.8	-	-	-
Mn2-Mn3	2.96	3.02	3.02	3.02	3.02	-	-	-
Mn2-Mn4	2.76	2.8	2.76	2.78	2.8	-	-	-
Mn3-Mn4	2.8	2.86	2.86	2.86	2.87	-	-	-
COO-Mn3	2.06	2.26	2.26	2.24	2.27	2.27	2.22	2.22

Table 5.3. Bond lengths of optimized structures of Inorganic cluster in S_2 state with TPSSh, B3LYP and PBE+U functionals comparing with the XRD crystal structure of synthetic complex from Agapie *et al.*

of the Mn-Mn and Mn-O distances with respect to crystallographic data [196] are shown in Table 5.3. Considering results optimized using the B3LYP and PBE+U functionals for this structure, both functionals seems to slightly overestimate all Mn-Mn distances.

The calculated J values by PBE+U/TZVP and B3LYP/TZVP are summarized in (Table 5.2) and reflect the differences reported in the geometries, being contradictory to the most of the experimental values. This lead to the conclusion that the difference in Mn3-O3 distance of about 0.2 Å is crucial in determining the electronic structure and magnetic properties of the Synthetic complex. Thus, we plan to further investigate the complex 3-ox with the help of extended BS approach and to calculate the EPR parameters and magnetic susceptibility plots.

Chapter 6

Summary

In this work, Density Functional Theory (DFT) methods have been used to study a variety of native and artificial systems containing multinuclear manganese sites as an integral part of their structure. These types of systems play an important role in biological catalysis, particularly for water splitting reaction and photosynthesis.

In this thesis, we explored the potentialities and the reliability of different state-of-the-art computational techniques for the investigation of the structural and vibrational properties of complex macromolecular materials of biochemical importance. In Chapter III, using Normal Mode Analysis in the mid-frequency region (1750-1300 cm^{-1}) we identified and assigned without ambiguity all the relevant peaks of the spectra. The employed calculation setup based on the B3LYP functional with TZVP basis set and D3 dispersion correction has proved to be a suitable model chemistry and offer the best compromise between quality and computational cost for the reliable theoretical interpretation of IR spectra in the region of carboxylate stretching.

In Chapter IV, we performed the detailed parallel analysis between Synthetic and Natural complexes providing a comprehensive characterization of the vibrational fingerprints of carboxylate ligands in such class of cubane-like Mn-based compounds. In the light of this characterization we identified firm points that should be considered in the interpretation of the spectra as well as the intrinsic limitations and weaknesses of commonly used interpretations.

Moreover, in Chapters III and IV, with the help of AIMD, we identified strong differences in the flexibility of the two clusters, which can be also correlated with differences in the catalytic properties of Synthetic complex. Using the Effective Normal Mode Analysis decomposition from ab initio dynamics for the low-frequency region we observed that the band position of Mn-O vibrational modes depends mostly on the character of the bridging ligands and the residues bonded to the oxygen atoms.

In Chapter V of the thesis we discussed our preliminary results on the electronic and structural properties of the novel Mn_4O_4 synthetic compound mimicking the EPR spectroscopic nature of OEC in S_2 state.

In summary the present work demonstrates how electronic structure calculations in combination with other computational methods are now mature to approach complex biological systems and they can be of valuable help in the rationalization

and understanding of structure/function relationships in molecular Biophysics.

Bibliography

[1] Generalized hartree-fock natural-orbital configuration-interaction (ghf no ci) approach to unstable molecules: trimethylene. *Chemical Physics Letters*, **49** (1977), 555 .

[2] A. Weil, J. and R. Bolton, J. *Electron paramagnetic resonance: elementary theory and practical applications.* Wiley, Hoboken (2007).

[3] Ahrling, K. A., Peterson, S., and Styring, S. An oscillating manganese electron paramagnetic resonance signal from the s0 state of the oxygen evolving complex in photosystem ii. *Biochemistry*, **36** (1997), 13148.

[4] Aizman, A. and Case, D. A. Electronic structure calculations on active site models for 4-fe,4-s iron-sulfur proteins. *Journal of the American Chemical Society*, **104** (1982), 3269.

[5] Allen, J. F. and Forsberg, J. Molecular recognition in thylakoid structure and function. *Trends in Plant Science*, **6** (2001), 317.

[6] Allen, J. F. and Martin, W. Out of thin air. *Nature*, **445** (2007), 610.

[7] Ames, W., Pantazis, D. A., Krewald, V., Cox, N., Messinger, J., Lubitz, W., and Neese, F. Theoretical evaluation of structural models of the s2 state in the oxygen evolving complex of photosystem ii: Protonation states and magnetic interactions. *Journal of the American Chemical Society*, **133** (2011), 19743.

[8] Anbar, A. D., et al. A whiff of oxygen before the great oxidation event? *Science*, **317** (2007), 1903.

[9] Anisimov, V. I., Solovyev, I. V., Korotin, M. A., Czyżyk, M. T., and Sawatzky, G. A. Density-functional theory and nio photoemission spectra. *Physical Review B*, **48** (1993), 16929.

[10] Anisimov, V. I., Zaanen, J., and Andersen, O. K. Band theory and mott insulators: Hubbard u instead of stoner i. *Phys. Rev. B*, **44** (1991), 943.

[11] Anisimov, V. I., Zaanen, J., and Andersen, O. K. Band theory and mott insulators: Hubbard u instead of stoner i. *Physical Review B*, **44** (1991), 943.

[12] Armstrong, F. A. Why did nature choose manganese to make oxygen? *Philosophical transactions of the Royal Society of London. Series B, Biological sciences*, **363** (2008), 1263.

[13] Arndt, B., et al. Carboxylic acid induced near-surface restructuring of a magnetite surface. *Communications Chemistry*, **2** (2019), 92.

[14] Askerka, M., Vinyard, D. J., Wang, J., Brudvig, G. W., and Batista, V. S. Analysis of the radiation-damage-free x-ray structure of photosystem ii in light of exafs and qm/mm data. *Biochemistry*, **54** (2015), 1713.

[15] Assefa, M., Devera, J., Brathwaite, J., and Duncan, M. Vibrational scaling factors for transition metal carbonyls. *Chemical Physics Letters*, **640** (2015).

[16] Baffert, C., et al. Biologically relevant mono- and di-nuclear manganese ii/iii/iv complexes of mononegative pentadentate ligands. *Dalton Transactions*, (2003), 1765.

[17] Bang, S., Lee, Y.-M., Hong, S., Cho, K.-B., Nishida, Y., Seo, M. S., Sarangi, R., Fukuzumi, S., and Nam, W. Redox-inactive metal ions modulate the reactivity and oxygen release of mononuclear non-haem iron(iii)–peroxo complexes. *Nature Chemistry*, **6** (2014), 934.

[18] Barber, J. Photosynthetic energy conversion: Natural and artificial. *Chem. Soc. Rev.*, (2009), 185.

[19] Barber, J. and Tran, P. D. From natural to artificial photosynthesis. *J.R. Soc., Interface*, (2013), 290.

[20] Barcelo, D. and Kostianoy, A. G. *The Handbook of Environmental Chemistry*. Springer-Verlag (1980).

[21] Barth, A. The infrared absorption of amino acid side chains. *Progress in Biophysics and Molecular Biology*, **74** (2000), 141.

[22] Barth, A. Infrared spectroscopy of proteins. *Biochimica et Biophysica Acta (BBA) - Bioenergetics*, **1767** (2007), 1073.

[23] Beck, W. F., De Paula, J. C., and Brudvig, G. W. Ammonia binds to the manganese site of the oxygen-evolving complex of photosystem ii in the s2 state. *Journal of the American Chemical Society*, **108** (1986), 4018.

[24] Becke, A. D. Density functional calculations of molecular bond energies. *The Journal of Chemical Physics*, **84** (1986), 4524.

[25] Becke, A. D. Density-functional exchange-energy approximation with correct asymptotic behavior. *Physical Review A*, **38** (1988), 3098.

[26] Becke, A. D. Density functional thermochemistry. iii. the role of exact exchange. *The Journal of Chemical Physics*, **7** (1993), 5648.

[27] Becke, A. D. A new mixing of hartree–fock and local density-functional theories. *The Journal of Chemical Physics*, **98** (1993), 1372.

[28] Bekker, A., Holland, H. D., Wang, P. L., Rumble, D., Stein, H. J., Hannah, J. L., Coetzee, L. L., and Beukes, N. J. Dating the rise of atmospheric oxygen. *Nature*, **427** (2004), 117.

[29] Bencini, A. and Gatteschi, D. *Electron paramagnetic resonance of exchange coupled systems*. Springer-Verlag Berlin Heidelberg, New York (1990).

[30] Benighaus, T., DiStasio, R. A., Lochan, R. C., Chai, J.-D., and Head-Gordon, M. Semiempirical double-hybrid density functional with improved description of long-range correlation. *The Journal of Physical Chemistry A*, **112** (2008), 2702.

[31] Berggren, G., Anderlund, M. F., Styring, S., and Thapper, A. Ftir study of manganese dimers with carboxylate donors as model complexes for the water oxidation complex in photosystem ii. *Inorganic Chemistry*, **4** (2012), 2332.

[32] Bernarding, J., Eckert, H.-J., Eichler, H. J., Napiwotzki, A., and Renger, G. Kinetic studies on the stabilization of the primary radical pair p680+ pheo- in different photosystem ii preparations from higher plants. *Photochemistry and Photobiology*, **59** (1994), 566.

[33] Berthomieu, C. and Hienerwadel, R. Fourier transform infrared (ftir) spectroscopy. *Photosynthesis Research*, **101** (2009), 157.

[34] Blankenship, R. E. *Molecular mechanisms of photosynthesis*. John Wiley & Sons (2013).

[35] Blankenship, R. E., et al. *Science*, (2011), 805.

[36] Bobrowicz, F. W. and Goddard, W. A. *The Self-Consistent Field Equations for Generalized Valence Bond and Open-Shell Hartree—Fock Wave Functions*, pp. 79–127. Springer US (1977). ISBN 978-1-4757-0887-5.

[37] Boese, A. D. and Handy, N. C. New exchange-correlation density functionals: The role of the kinetic-energy density. *The Journal of Chemical Physics*, **116** (2002), 9559.

[38] Boussac, A., A. Rutherford, W., and Sugiura, M. Electron transfer pathways from the s2-states to the s3-states either after a ca2+/sr2+ or a cl-/i- exchange in photosystem ii from thermosynechococcus elongatus. *Biochimica et Biophysica Acta (BBA) - Bioenergetics*, **1847** (2015), 576 .

[39] Boussac, A., Girerd, J.-J., and Rutherford, A. W. Conversion of the spin state of the manganese complex in photosystem ii induced by near-infrared light. *Biochemistry*, **35** (1996), 6984.

[40] Boussac, A. and Rutherford, A. W. Nature of the inhibition of the oxygen-evolving enzyme of photosystem ii induced by sodium chloride washing and reversed by the addition of calcium(2+) or strontium(2+). *Biochemistry*, **27** (1988), 3476.

[41] Boussac, A., Sugiura, M., Rutherford, A. W., and Dorlet, P. Complete epr spectrum of the s3-state of the oxygen-evolving photosystem ii. *Journal of the American Chemical Society*, **131** (2009), 5050.

[42] Boussac, A., Zimmermann, J. L., and Rutherford, A. W. Epr signals from modified charge accumulation states of the oxygen-evolving enzyme in calcium-deficient photosystem ii. *Biochemistry*, **28** (1989), 8984.

[43] Boussac, A., Zimmermann, J.-L., and Rutherford, A. W. *Further Characterization of the Modified S2 and S3 EPR Signals Observed in Ca2+-Depleted Photosystem-II Reconstituted with the 17 and 23 kDA Polypeptides*. Springer Netherlands (1990).

[44] Bovi, D., Capone, M., Narzi, D., and Guidoni, L. Vibrational fingerprints of the mn4cao5 cluster in photosystemii by mixed quantum-classical molecular dynamics. *Biochimica et Biophysica Acta (BBA)-Bioenergetics*, **1857** (2016), 1669.

[45] Bovi, D., Narzi, D., and Guidoni, L. The s2 state of the oxygen-evolving complex of photosystem ii explored by qm/mm dynamics: Spin surfaces and metastable states suggest a reaction path towards the s3 state. *Angewandte Chemie International Edition*, **52** (2013), 11744.

[46] Bovi, D., Narzi, D., and Guidoni, L. Magnetic interactions in the catalyst used by nature to split water: A dft+ u multiscale study on the mn4cao5 core in photosystem ii. *New Journal of Physics*, **16** (2014), 015020.

[47] Brimblecombe, R., Swiegers, G. F., Dismukes, G. C., and Spiccia, L. Sustained water oxidation photocatalysis by a bioinspired manganese cluster. *Angewandte Chemie International Edition*, **47** (2008), 7335.

[48] Britt, R., Zimmermann, J., Sauer, K., and Klein, M. Ammonia binds to the catalytic mn of the oxygen-evolving complex of photosystem-ii: evidence by electron-spin echo envelope modulation spectroscopy. *J Am Chem Soc*, (1989), 3522–3532.

[49] Britt, R. D., Campbell, K. A., Peloquin, J. M., Gilchrist, M. L., Aznar, C. P., Dicus, M. M., Robblee, J., and Messinger, J. Recent pulsed epr studies of the photosystem ii oxygen-evolving complex: implications as to water oxidation mechanisms. *Biochimica et Biophysica Acta (BBA) - Bioenergetics*, **1655** (2004), 158 .

[50] Britt, R. D., Peloquin, J. M., and Campbell, K. A. Pulsed and parallel-polarization epr characterization of the photosystem ii oxygen-evolving complex. *Annual Review of Biophysics and Biomolecular Structure*, **29** (2000), 463.

[51] Brudvig, G. and Crabtree, R. Mechanism for photosynthetic o2 evolution. *Proceedings of the National Academy of Sciences*, **83** (1986), 4586.

[52] Capone, M., Bovi, D., Narzi, D., and Guidoni, L. Reorganization of substrate waters between the closed and open cubane conformers during the s2 to s3 transition in the oxygen evolving complex. *Biochemistry*, **54** (2015), 6439.

[53] Capone, M., Narzi, D., Tychengulova, A., and Guidoni, L. On the comparison between differential vibrational spectroscopy spectra and theoretical data in the carboxyl region of photosystem ii. *Physiologia Plantarum*, **166** (2019), 33.

[54] Ceperley, D. M. and Alder, B. J. Ground state of the electron gas by a stochastic method. *Physical Review Letters*, **45** (1980), 566.

[55] Chan, M. K. and Armstrong, W. H. A high-potential mononuclear manganese(iv) complex. synthesis, structure, and properties, including epr spectroscopy and electrochemistry, of [mn(hb(3,5-me2pz)3)2] (clo4)2 (pz = pyrazolyl). *Inorganic Chemistry*, **28** (1989), 3777.

[56] Chan, M. K. and Armstrong, W. H. Support for a dimer of di-μ-oxo dimers model for the photosystem ii manganese aggregate. synthesis and properties of [(mn2o2)2(tphpn)2](clo4)4. *Journal of the American Chemical Society*, **113** (1991), 5055.

[57] Chatterjee, R., et al. Structural changes correlated with magnetic spin state isomorphism in the s2 state of the mn4cao5 cluster in the oxygen-evolving complex of photosystem ii. *Chem. Sci.*, **7** (2016), 5236.

[58] Chen, C., Li, Y., Zhao, G., Yao, R., and Zhang, C. Natural and artificial mn4ca cluster for the water splitting reaction. *ChemSusChem*, **10** (2017), 4403.

[59] Chen, H., Dismukes, G. C., and Case, D. A. Resolving ambiguous protonation and oxidation states in the oxygen evolving complex of photosystem ii. *The Journal of Physical Chemistry B*, **122** (2018), 8654.

[60] Chen, H., Sun, Z., Liu, X., Han, A., and Du, P. Cobalt–salen complexes as catalyst precursors for electrocatalytic water oxidation at low overpotential. *The Journal of Physical Chemistry C*, **119** (2015), 8998.

[61] Christou, G. Manganese carboxylate chemistry and its biological relevance. *Accounts of Chemical Research*, **22** (1989), 328.

[62] Chu, H., Debus, R., and Babcock, G. D1-asp170 is structurally coupled to the oxygen evolving complex in photosystem ii as revealed by light-induced fourier transform infrared difference spectroscopy. *Biochemistry*, **40** (2001).

[63] Chu, H.-A. Fourier transform infrared difference spectroscopy for studying the molecular mechanism of photosynthetic water oxidation. *Frontiers in Plant Science*, **4** (2013), 146.

[64] Chu, H. A., Gardner, M. T., O'brien, J. P., and Babcock, G. T. Low-frequency fourier transform infrared spectroscopy of the oxygen-evolving and quinone acceptor complexes in photosystem ii. *Biochemistry*, **38** (1999), 4533.

[65] Chu, H.-A., Hillier, W., A., L. N., and Babcock, G. T. Vibrational spectroscopy of the oxygen-evolving complex and of manganese model compounds. *Biochimica et Biophysica Acta (BBA) - Bioenergetics*, **1503** (2001), 69.

[66] Chu, H.-A., Hillier, W., and Debus, R. J. Evidence that the c-terminus of the d1 polypeptide of photosystem ii is ligated to the manganese ion that undergoes oxidation during the s1 to s2 transition: an isotope-edited ftir study. *Biochemistry*, **43** (2004), 3152.

[67] Chu, H.-A., Sackett, H., and Babcock, G. T. Identification of a mn-o-mn cluster vibrational mode of the oxygen-evolving complex in photosystem ii by low-frequency ftir spectroscopy. *Biochemistry*, **39** (2000), 14371.

[68] Chu, H.-A., Sackett, H., and Babcock, G. T. Identification of a mn-o-mn cluster vibrational mode of the oxygen-evolving complex in photosystem ii by low-frequency ftir spectroscopy. *Biochemistry*, **39** (2000), 14371.

[69] Chuah, W. Y., Stranger, R., Pace, R. J., Krausz, E., and Frankcombe, T. J. Deprotonation of water/hydroxo ligands in clusters mimicking the water oxidizing complex of psii and its effect on the vibrational frequencies of ligated carboxylate groups. *The Journal of Physical Chemistry B*, **120** (2016), 377.

[70] Ciamician, G. The photochemistry of the future. *Science*, **36** (1912), 385.

[71] Ciofini, I., Illas, F., and Adamo, C. Performance of the τ-dependent functionals in predicting the magnetic coupling of ionic antiferromagnetic insulators. *The Journal of Chemical Physics*, **120** (2004), 3811.

[72] Cococcioni, M. *A LDA+U study of selected iron compounds*. Ph.D. thesis, SISSA, Trieste, Italy (2002).

[73] Codolà, Z., Gómez, L., Kleespies, S. T., Que Jr, L., Costas, M., and Lloret-Fillol, J. Evidence for an oxygen evolving iron–oxo–cerium intermediate in iron-catalysed water oxidation. *Nature Communications*, **6** (2015), 5865.

[74] Coggins, M. K., Zhang, M.-T., Vannucci, A. K., Dares, C. J., and Meyer, T. J. Electrocatalytic water oxidation by a monomeric amidate–ligated fe(iii)-–aqua complex. *Journal of the American Chemical Society*, **136** (2014), 5531.

[75] Cohen, A. J., Mori-Sánchez, P., and Yang, W. Fractional spins and static correlation error in density functional theory. *The Journal of Chemical Physics*, **129** (2008), 121104.

[76] Cohen, A. J., Mori-Sánchez, P., and Yang, W. Insights into current limitations of density functional theory. *Science*, **321** (2008), 792.

[77] Cohen, A. J., Mori-Sánchez, P., and Yang, W. Challenges for density functional theory. *Chemical Reviews*, **112** (2012), 289.

[78] Concepcion, J. J., Tsai, M.-K., Muckerman, J. T., and Meyer, T. J. Mechanism of water oxidation by single-site ruthenium complex catalysts. *Journal of the American Chemical Society*, **132** (2010), 1545.

[79] Cooper, S. R. and Calvin, M. Mixed valence interactions in di-.mu.-oxo bridged manganese complexes. *Journal of the American Chemical Society*, **99** (1977), 6623.

[80] Cox, N., Retegan, M., Neese, F., Pantazis, D., Boussac, A., and Lubitz, W. Electronic structure of the oxygen-evolving complex in photosystem ii prior to oo bond formation. *Science*, **345** (2014), 804.

[81] Cox, N., et al. *J. Am. Chem. Soc.*, (2011), 3635.

[82] Daldrop, J. O., Saita, M., Heyden, M., Lorenz-Fonfria, V. A., Heberle, J., and Netz, R. R. Orientation of non-spherical protonated water clusters revealed by infrared absorption dichroism. *Nature communications*, **9** (2018), 311.

[83] Dau, H. and Haumann, M. Eight steps preceding o–o bond formation in oxygenic photosynthesis—a basic reaction cycle of the photosystem ii manganese complex. *Biochimica et Biophysica Acta (BBA) - Bioenergetics*, **1767** (2007), 472.

[84] Dau, H. and Haumann, M. The manganese complex of photosystem ii in its reaction cycle—basic framework and possible realization at the atomic level. *Coordination Chemistry Reviews*, **252** (2008), 273.

[85] Dau, H., Liebisch, P., and Haumann, M. The structure of the manganese complex of photosystem ii in its dark-stable s1-state—exafs results in relation to recent crystallographic data. *Physical Chemistry Chemical Physics*, **6** (2004), 4781.

[86] Dau, H., Limberg, C., Reier, T., Risch, M., Roggan, S., and Strasser, P. The mechanism of water oxidation: From electrolysis via homogeneous to biological catalysis. *ChemCatChem*, **2** (2010), 724.

[87] Dau, H., Zaharieva, I., and Haumann, M. C. *Opinion Chem. Biol.*, (2012), 3.

[88] De Paula, J. C., Beck, W. F., and Brudvig, G. W. Magnetic properties of manganese in the photosynthetic o2-evolving complex. 2. evidence for a manganese tetramer. *Journal of the American Chemical Society*, **108** (1986), 4002.

[89] Debus, R. J. Protein ligation of the photosynthetic oxygen-evolving center. *Coordination Chemistry Reviews*, **252** (2008), 244.

[90] Debus, R. J. Evidence from ftir difference spectroscopy that d1-asp61 influences the water reactions of the oxygen-evolving mn4cao5 cluster of photosystem ii. *Biochemistry*, **53** (2014), 2941.

[91] Debus, R. J. Ftir studies of metal ligands, networks of hydrogen bonds, and water molecules near the active site mn4co5 cluster in photosystem ii. *Biochimica et Biophysica Acta (BBA)-Bioenergetics*, **1847** (2015), 19.

[92] Debus, R. J., Strickler, M. A., Walker, L. M., and Hillier, W. No evidence from ftir difference spectroscopy that aspartate-170 of the d1 polypeptide ligates a manganese ion that undergoes oxidation during the s0 to s1, s1 to s2, or s2 to s3 transitions in photosystem ii. *Biochemistry*, **44** (2005), 1367.

[93] Deisenhofer, J., Epp, O., Miki, K., Huber, R., and Michel, H. Structure of the protein subunits in the photosynthetic reaction centre of rhodopseudomonas viridis at 3åresolution. *Nature*, **318** (1985), 618.

[94] Dirac, P. A. M. and Fowler, R. H. Quantum mechanics of many-electron systems. *Proceedings of the Royal Society of London. Series A, Containing Papers of a Mathematical and Physical Character*, **123** (1929), 714.

[95] Dismukes, G. C. and Siderer, Y. Intermediates of a polynuclear manganese center involved in photosynthetic oxidation of water. *Proceedings of the National Academy of Sciences*, **78** (1981), 274.

[96] Dogutan, D. K., McGuire, R., and Nocera, D. G. Electocatalytic water oxidation by cobalt(iii) hangman β–octafluoro corroles. *Journal of the American Chemical Society*, **133** (2011), 9178.

[97] Du, H.-Y., Chen, S.-C., Su, X.-J., Jiao, L., and Zhang, M.-T. Redox-active ligand assisted multielectron catalysis: A case of coiii complex as water oxidation catalyst. *Journal of the American Chemical Society*, **140** (2018), 1557.

[98] Duan, L., Araujo, C. M., Ahlquist, M. S., and Sun, L. Highly efficient and robust molecular ruthenium catalysts for water oxidation. *Proceedings of the National Academy of Sciences*, **109** (2012), 15584.

[99] Duan, L., Xu, Y., Zhang, P., Wang, M., and Sun, L. Visible light-driven water oxidation by a molecular ruthenium catalyst in homogeneous system. *Inorganic Chemistry*, **49** (2010), 209.

[100] Dudarev, S., Botton, G., Savrasov, S., Humphreys, C., and Sutton, A. Electron-energy-loss spectra and the structural stability of nickel oxide: An lsda+ u study. *Physical Review B*, **57** (1998), 1505.

[101] Dudarev, S., Manh, D. N., and Sutton, A. Effect of mott-hubbard correlations on the electronic structure and structural stability of uranium dioxide. *Philosophical Magazine B*, **75** (1997), 613.

[102] Dudarev, S. L., Botton, G. A., Savrasov, S. Y., Humphreys, C. J., and Sutton, A. P. Electron-energy-loss spectra and the structural stability of nickel oxide: An lsda+u study. *Physical Review B*, **57** (1998), 1505.

[103] Dudarev, S. L., Nguyen Manh, D., and Sutton, A. P. Effect of mott-hubbard correlations on the electronic structure and structural stability of uranium dioxide. *Philosophical Magazine B*, **75** (1997), 613.

[104] Dunning, T. H. Gaussian basis sets for use in correlated molecular calculations. i. the atoms boron through neon and hydrogen. *The Journal of Chemical Physics*, **90** (1989), 1007.

[105] Ellis, W. C., McDaniel, N. D., Bernhard, S., and Collins, T. J. Fast water oxidation using iron. *Journal of the American Chemical Society*, **132** (2010), 10990.

[106] Emerson, R. and Arnold, W. The photochemical reaction in photosynthesis. *The Journal of General Physiology*, **16** (1932), 191.

[107] Evans, M., Sihra, C., and Slabas, A. The oxidation-reduction potential of the reaction-centre chlorophyll (p700) in photosystem i. evidence for multiple components in electron-paramagnetic-resonance signal 1 at low temperature. *The Biochemical Journal*, **162** (1977), 75.

[108] Faunce, T., et al. Artificial photosynthesis as a frontier technology for energy sustainability. *Energy Environ. Sci.*, (2013), 1074.

[109] Ferreira, K. N., Iverson, T. M., Maghlaoui, K., Barber, J., and Iwata, S. *Science*, (2004), 1831.

[110] Fillol, J. L., Codolà, Z., Garcia-Bosch, I., Gómez, L., Pla, J. J., and Costas, M. Efficient water oxidation catalysts based on readily available iron coordination complexes. *Nature Chemistry*, **3** (2011), 807.

[111] Fock, V. Näherungsmethode zur lösung des quantenmechanischen mehrkörperproblems. *Zeitschrift für Physik*, **61** (1930), 126.

[112] Forster, V. and Junge, W. Stoichiometry and kinetics of proton release upon photosynthetic water oxidation. *Photochemistry and Photobiology*, **41** (1985), 183.

[113] Freitag, M. and Boschloo, G. The revival of dye-sensitized solar cells. *CURRENT OPINION IN ELECTROCHEMISTRY*, **2** (2017), 111.

[114] Freitag, M., Giordano, F., Yang, W., Pazoki, M., Hao, Y., Zietz, B., Grätzel, M., Hagfeldt, A., and Boschloo, G. Copper phenanthroline as a fast and high-performance redox mediator for dye-sensitized solar cells. *The Journal of Physical Chemistry C*, **120** (2016), 9595.

[115] Gagliardi, L., Truhlar, D. G., Li Manni, G., Carlson, R. K., Hoyer, C. E., and Bao, J. L. Multiconfiguration pair-density functional theory: A new way to treat strongly correlated systems. *Accounts of Chemical Research*, **50** (2017), 66.

[116] Gaigeot, M.-P. Theoretical spectroscopy of floppy peptides at room temperature. a dftmd perspective: gas and aqueous phase. *Physical Chemistry Chemical Physics*, **12** (2010), 3336.

[117] Gaigeot, M.-P. Infrared spectroscopy of small protonated water clusters at room temperature: An effective modes analysis. *The Journal of chemical physics*, **138** (2011), 257.

[118] Galimberti, D. R., Milani, A., Gaigeot, M.-P., Radice, S., Tonelli, C., Picozzi, R., and Castiglioni, C. Static vs dynamic dft prediction of ir spectra of flexible molecules in the condensed phase: The (clcf2cf(cf3)ocf2ch3) liquid as a test case. *Spectrochimica Acta Part A: Molecular and Biomolecular Spectroscopy*, **183** (2017), 195 .

[119] Gao, Y., Åkermark, T., Liu, J., Sun, L., and Åkermark, B. Nucleophilic attack of hydroxide on a mnv oxo complex: A model of the o–o bond formation in the oxygen evolving complex of photosystem ii. *Journal of the American Chemical Society*, **131** (2009), 8726.

[120] Gerey, B., Goure, E., Fortage, J., Pecaut, J., and Collomb, M.-N. Manganese-calcium/strontium heterometallic compounds and their relevance for the oxygen-evolving center of photosystem ii. *Coordination Chemistry Reviews*, **319** (2016), 1.

[121] Gloaguen, E., et al. Gas-phase folding of a two-residue model peptide chain: on the importance of an interplay between experiment and theory. *Journal of the American Chemical Society*, **132** (2010), 11860.

[122] Goedecker, S., Teter, M., and Hutter, J. Separable dual-space gaussian pseudopotentials. *Physical Review B*, **54** (1996), 1703.

[123] Goldfarb, S. S., Daniella. *EPR spectroscopy: fundamentals and methods.* eMagRes Books and Wiley, New York (2018).

[124] Golub, G. H. and Reinsch, C. Singular value decomposition and least squares solutions. *Numerische Mathematik*, **14** (1970), 403.

[125] Govindjee and Shevela, D. Adventures with cyanobacteria: A personal perspective. *Frontiers in Plant Science*, **2** (2011), 28.

[126] Grimme, S. Semiempirical hybrid density functional with perturbative second-order correlation. *The Journal of Chemical Physics*, **124** (2006), 034108.

[127] Grimme, S., Antony, J., Ehrlich, S., and Krieg, H. A consistent and accurate ab initio parametrization of density functional dispersion correction (dft-d) for the 94 elements h-pu. *The Journal of Chemical Physics*, **154104** (2010), 1.

[128] Grimme, S., Ehrlich, S., and Goerigk, L. Effect of the damping function in dispersion corrected density functional theory. *Journal of Computational Chemistry*, **32** (2011), 1456.

[129] Grundmeier, A. and Dau, H. Structural models of the manganese complex of photosystem ii and mechanistic implications. *Biochimica et Biophysica Acta (BBA)-Bioenergetics*, **1817** (2012), 88.

[130] Guidon, M., Hutter, J., and VandeVondele, J. Auxiliary density matrix methods for hartree-fock exchange calculations. *Journal of Chemical Theory and Computation*, **8** (2010), 2348.

[131] Guskov, A., Kern, J., Gabdulkhakov, A., Broser, M., Zouni, A., and Saenger, W. *Nat. Struct. Mol. Biol.*, (2009), 334.

[132] Haddy, A. *Photosynthesis Research*, (2008), 357.

[133] Haddy, A., Lakshmi, K., W. Brudvig, G., and Frank, H. A. Q-band epr of the s2 state of photosystem ii confirms an s=5/2 origin of the x-band g=4.1 signal. *Biophysical Journal*, **87** (2004), 2885 .

[134] Hagfeldt, A., Boschloo, G., Sun, L., Kloo, L., and Pettersson, H. Dye-sensitized solar cells. *Chemical Reviews*, **110** (2010), 6595.

[135] Hamilton, T. P. and Pulay, P. Direct inversion in the iterative subspace (diis) optimization of open-shell, excited-state, and small multiconfiguration scf wave functions. *The Journal of Chemical Physics*, **84** (1986), 5728.

[136] Hansson, O., Aasa, R., and Vanngaard, T. The origin of the multiline and g = 4.1 electron paramagnetic resonance signals from the oxygen-evolving system of photosystem ii. *Biophysical Journal*, **51** (1987), 825.

[137] Harriman, A., Pickering, I. J., Thomas, J. M., and Christensen, P. A. Metal oxides as heterogeneous catalysts for oxygen evolution under photochemical conditions. *J. Chem. Soc., Faraday Trans. 1*, **84** (1988), 2795.

[138] Hartree, D. R. The wave mechanics of an atom with a non-coulomb central field. part i. theory and methods. *Mathematical Proceedings of the Cambridge Philosophical Society*, **24** (1928), 89.

[139] Hartwigsen, C., Goedecker, S., and Hutter, J. Relativistic separable dual-space gaussian pseudopotentials from h to rn. *Physical Review B*, **58** (1998), 3641.

[140] Hartwigsen, C., Gœdecker, S., and Hutter, J. Relativistic separable dual-space gaussian pseudopotentials from h to rn. *Physical Review B*, **58** (1998), 3641.

[141] Hill, R. M. and Bendall, F. Function of the two cytochrome components in chloroplasts: A working hypothesis. *Nature*, **186** (1960), 136.

[142] Hillier, W. and Babcock, G. T. S-state dependent fourier transform infrared difference spectra for the photosystem ii oxygen evolving complex. *Biochemistry*, **40** (2001), 1503.

[143] Himmetoglu, B., Floris, A., de Gironcoli, S., and Cococcioni, M. Hubbard-corrected dft energy functionals: The lda+u description of correlated systems. *International Journal of Quantum Chemistry*, **114** (2014), 14.

[144] Hodge, J. A., Hill, M. G., and Gray, H. B. Electrochemistry of nonplanar zinc(ii) tetrakis(pentafluorophenyl)porphyrins. *Inorganic Chemistry*, **34** (1995), 809.

[145] Hohenberg, P. and Kohn, W. Inhomogeneous electron gas. *Physical Review B*, **136** (1964), 864.

[146] Hong, D., Jung, J., Park, J., Yamada, Y., Suenobu, T., Lee, Y.-M., Nam, W., and Fukuzumi, S. Water-soluble mononuclear cobalt complexes with organic ligands acting as precatalysts for efficient photocatalytic water oxidation. *Energy Environ. Sci.*, **5** (2012), 7606.

[147] Iizasa, M., Suzuki, H., and Noguchi, T. Orientations of carboxylate groups coupled to the mn cluster in the photosynthetic oxygen-evolving center as studied by polarized atr-ftir spectroscopy. *Biochemistry*, **49** (2010), 3074.

[148] Ilke, U., A. William, R., and Ville, R. K. Redox-coupled substrate water reorganization in the active site of photosystem ii—the role of calcium in substrate water delivery. *Biochimica et Biophysica Acta (BBA) - Bioenergetics*, **1857** (2016), 740 .

[149] Ishikita, H. and Knapp, E.-W. Function of redox-active tyrosine in photosystem ii. *Biophysical Journal*, **90** (2006), 3886.

[150] Isobe, H., Shoji, M., Yamanaka, S., Umena, Y., Kawakami, K., Kamiya, N., Shen, J.-R., and Yamaguchi, K. Theoretical illumination of water-inserted structures of the camn4o5 cluster in the s2 and s3 states of oxygen-evolving complex of photosystem ii: full geometry optimizations by b3lyp hybrid density functional. *Dalton Transactions*, **41** (2012), 13727.

[151] Ito, A. A historical meta-analysis of global terrestrial net primary productivity: are estimates converging? *Global Change Biology*, **17** (2011), 3161.

[152] Ivanic, J. Direct configuration interaction and multiconfigurational self-consistent-field method for multiple active spaces with variable occupations. I. Method. *The Journal of Chemical Physics*, **119** (2003), 9364.

[153] Jahn, H. A. and Teller, E. Stability of Polyatomic Molecules in Degenerate Electronic States. I. Orbital Degeneracy. *Proceedings of the Royal Society of London Series A*, **161** (1937), 220.

[154] Jiao, F. and Frei, H. Nanostructured manganese oxide clusters supported on mesoporous silica as efficient oxygen-evolving catalysts. *Chem. Commun.*, **46** (2010), 2920.

[155] Johnson, J. E., Webb, S. M., Thomas, K., Ono, S., Kirschvink, J. L., and Fischer, W. W. Manganese-oxidizing photosynthesis before the rise of cyanobacteria. *Proceedings of the National Academy of Sciences*, **110** (2013), 11238.

[156] Joliot, P., Barbieri, G., and Chabaud, R. Un nouveau modele des centres photochimiques du systeme ii*. *Photochemistry and Photobiology*, **10** (1969), 309.

[157] Joliot, P. and Joliot, A. A polarographic method for detection of oxygen production and reduction of hill reagent by isolated chloroplasts. *Biochimica et Biophysica Acta (BBA) - Bioenergetics*, **153** (1968), 625 .

[158] Junge, W. Oxygenic photosynthesis: history, status and perspective. *Quarterly Reviews of Biophysics*, **52** (2019), e1.

[159] Junge, W., Haumann, M., Ahlbrink, R., Mulkidjanian, A., and Clausen, J. Electrostatics and proton transfer in photosynthetic water oxidation. *Philosophical transactions of the Royal Society of London. Series B, Biological sciences*, **357** (2002), 1407—17; discussion 1417—20.

[160] Junqi, L., Peng, K., Xiangming, L., Baochun, M., and Yong, D. Homogeneous electrocatalytic water oxidation catalyzed by a mononuclear nickel complex. *Electrochimica Acta*, **258** (2017), 353 .

[161] Kamiya, N. and Shen, J. R. *Proc. Natl. Acad. Sci. U. S. A.*, (2003), 98.

[162] Kanady, J. S., Lin, P.-H., Carsch, K. M., Nielsen, R. J., Takase, M. K., Goddard III, W. A., and Agapie, T. Toward models for the full oxygen-evolving complex of photosystem ii by ligand coordination to lower the symmetry of the mn3cao4 cubane: Demonstration that electronic effects facilitate binding of a fifth metal. *Journal of the American Chemical Society*, **136** (2014), 14373.

[163] Kanady, J. S., Tsui, E. Y., Day, M. W., and Agapie, T. A synthetic model of the mn3ca subsite of the oxygen-evolving complex in photosystem ii. *Science*, **333** (2011), 733.

[164] Kanady, J. S., Tsui, E. Y., Day, M. W., and Agapie, T. A synthetic model of the mn3ca subsite of the oxygen-evolving complex in photosystem ii. *Science*, **333** (2011), 733.

[165] Kanan, M. W. and Nocera, D. G. In situ formation of an oxygen-evolving catalyst in neutral water containing phosphate and co2+. *Science*, **321** (2008), 1072.

[166] Kanda, K., et al. Labile electronic and spin states of the camn4o5 cluster in the psii system refined to the 1.9 åx-ray resolution. ub3lyp computational results. *Chemical Physics Letters*, **506** (2011), 98.

[167] Kärkäs, M. D., Verho, O., Johnston, E. V., and Åkermark, B. Artificial photosynthesis: Molecular systems for catalytic water oxidation. *Chemical Reviews*, **114** (2014), 11863.

[168] Karlsson, E. A., Lee, B.-L., Åkermark, T., Johnston, E. V., Kärkäs, M. D., Sun, J., Hansson, Ö., Bäckvall, J.-E., and Åkermark, B. Photosensitized water oxidation by use of a bioinspired manganese catalyst. *Angewandte Chemie International Edition*, **50** (2011), 11715.

[169] Kashif, M. K., et al. Cobalt polypyridyl complexes as transparent solution-processable solid-state charge transport materials. *Advanced Energy Materials*, **6** (2016), 1600874.

[170] Kaupp, M., Reviakine, R., Malkina, O. L., Arbuznikov, A., Schimmelpfennig, B., and Malkin, V. G. Calculation of electronic g-tensors for transition metal complexes using hybrid density functionals and atomic mean-field spin-orbit operators. *Journal of Computational Chemistry*, **23** (2002), 794.

[171] Kesharwani, M. K., Brauer, B., and Martin, J. M. L. Frequency and zero-point vibrational energy scale factors for double-hybrid density functionals (and other selected methods): Can anharmonic force fields be avoided? *The Journal of Physical Chemistry A*, **119** (2015), 1701.

[172] Kimura, Y., Ishii, A., Yamanari, T., and Ono, T.-a. Water-sensitive low-frequency vibrations of reaction intermediates during s-state cycling in photosynthetic water oxidation. *Biochemistry*, **44** (2005), 7613.

[173] Kimura, Y., Mizusawa, N., Ishii, A., Nakazawa, S., and Ono, T.-a. Changes in structural and functional properties of oxygen-evolving complex induced by replacement of d1-glutamate 189 with glutamine in photosystem ii: Ligation of glutamate 189 carboxylate to the manganese cluster. *Journal of Biological Chemistry*, **280** (2005), 37895.

[174] Kimura, Y., Mizusawa, N., Ishii, A., Yamanari, T., and Ono, T.-a. Changes of low-frequency vibrational modes induced by universal 15n- and 13c-isotope labeling in s2/s1 ftir difference spectrum of oxygen-evolving complex. *Biochemistry*, **42** (2003), 13170.

[175] Kimura, Y., Mizusawa, N., Ishii, A., Yamanari, T., and Ono, T.-a. Changes of low-frequency vibrational modes indused by universal n and c-isotope labelling in s2-s1 ftir difference spectrum of oxygen-evolving complex. *Biochemistry*, **42** (2003), 13170.

[176] Kimura, Y., Mizusawa, N., Yamanari, T., Ishii, A., and Ono, T.-a. Structural changes of d1 c-terminal α-carboxylate during s-state cycling in photosynthetic oxygen evolution. *Journal of Biological Chemistry*, **280** (2005), 2078.

[177] Kirch, M., Lehn, J.-M., and Sauvage, J.-P. Hydrogen generation by visible light irradiation of aqueous solutions of metal complexes. an approach to the photochemical conversion and storage of solar energy. *Helvetica Chimica Acta*, **62** (1979), 1345.

[178] Kohls, E. and Stein, M. Vibrational scaling factors for rh(i) carbonyl compounds in homogeneous catalysis. *Contributions, Section of Natural, Mathematical and Biotechnical Sciences,*, **38** (2017), 43.

[179] Kohn, W. and Sham, L. J. Self-consistent equations including exchange and correlation effects. *Physical Review A*, **140** (1965), 1133.

[180] Koji, H., Masami, K., Yorinao, I., and Taka-aki, O. Simulation of s2-state multiline epr signal in oriented photosystem ii membranes: Structural implications for the manganese cluster in an oxygen-evolving complex. *Biochemistry*, **37** (1998), 9457.

[181] Koji, H., Taka-aki, O., Yorinao, I., and Masami, K. Spin-exchange interactions in the s2-state manganese tetramer in photosynthetic oxygen-evolving complex deduced from g=2 multiline epr signal. *Chemical Physics Letters*, **300** (1999), 9 .

[182] Kok, B., Forbush, B., and McGloin, M. Cooperation of charges in photosynthetic o2 evolution–i. a linear four step mechanism. *Photochemistry and Photobiology*, **11** (1970), 457.

[183] Kolling, D., Cox, N., Ananyev, G., Pace, R., and Dismukes, G. What are the oxidation states of manganese required to catalyze photosynthetic water oxidation? *Biophys J*, (2012), 313.

[184] Koua, F. H. M., Umena, Y., Kawakami, K., and Shen, J.-R. *Proc. Natl. Acad. Sci. U. S. A.*, (2013), 3889.

[185] Krack, M. Pseudopotentials for h to kr optimized for gradient-corrected exchange-correlation functionals. *Theoretical Chemistry Accounts: Theory, Computation, and Modeling (Theoretica Chimica Acta)*, **114** (2005), 145.

[186] Krewald, V., Neese, F., and Pantazis, D. A. On the magnetic and spectroscopic properties of high-valent mn3cao4 cubanes as structural units of natural and artificial water-oxidizing catalysts. *Journal of the American Chemical Society*, **135** (2013), 5726.

[187] Krewald, V., Retegan, M., Cox, N., Messinger, J., Lubitz, W., DeBeer, S., Neese, F., and Pantazis, D. A. Metal oxidation states in biological water splitting. *Chemical Science*, **6** (2015), 1676.

[188] Krewald, V., Retegan, M., Neese, F., Lubitz, W., Pantazis, D. A., and Cox, N. Spin state as a marker for the structural evolution of nature's water-splitting catalyst. *Inorganic chemistry*, **55** (2015), 488.

[189] Krewald, V., Retegan, M., Neese, F., Lubitz, W., Pantazis, D. A., and Cox, N. Spin state as a marker for the structural evolution of nature's water-splitting catalyst. *Inorganic Chemistry*, **55** (2016), 488.

[190] Kudo, A. Z-scheme photocatalyst systems for water splitting under visible light irradiation. *MRS Bulletin*, **36** (2011), 32.

[191] Kulik, L. V., Epel, B., Lubitz, W., and Messinger, J. *J. Am. Chem. Soc.*, (2005), 2392.

[192] Kulik, L. V., Epel, B., Lubitz, W., and Messinger, J. Electronic structure of the mn4oxca cluster in the s0 and s2 states of the oxygen-evolving complex of photosystem ii based on pulse 55mn-endor and epr spectroscopy. *Journal of the American Chemical Society*, **129** (2007), 13421.

[193] L. Casey, J. and Sauer, K. Epr detection of a cryogenically photogenerated intermediate in photosynthetic oxygen evolution. *Biochimica et Biophysica Acta (BBA) - Bioenergetics*, **767** (1984), 21 .

[194] Lavergne, J. and Junge, W. Proton release during the redox cycle of the water oxidase. *Photosynthesis Research*, **38** (1999), 279.

[195] Lee, C., Yang, W., and Parr, R. G. Development of the colle-salvetti correlation-energy formula into a functional of the electron density. *Physical Review B*, **37** (1988), 785.

[196] Lee, H. B., Shiau, A. A., Oyala, P. H., Marchiori, D. A., Gul, S., Chatterjee, R., Yano, J., Britt, R. D., and Agapie, T. Tetranuclear [mniiimn3ivo4] complexes as spectroscopic models of the s2 state of the oxygen evolving complex in photosystem ii. *Journal of the American Chemical Society*, **140** (2018), 17175.

[197] Lei, H., Han, A., Li, F., Zhang, M., Han, Y., Du, P., Lai, W., and Cao, R. Electrochemical, spectroscopic and theoretical studies of a simple bifunctional cobalt corrole catalyst for oxygen evolution and hydrogen production. *Phys. Chem. Chem. Phys.*, **16** (2014), 1883.

[198] Leung, C.-F., Ng, S.-M., Ko, C.-C., Man, W.-L., Wu, J., Chen, L., and Lau, T.-C. A cobalt(ii) quaterpyridine complex as a visible light-driven catalyst for both water oxidation and reduction. *Energy Environ. Sci.*, **5** (2012), 7903.

[199] Lewars, E. G. *Computational Chemistry Introduction to the Theory and Applications of Molecular and Quantum Mechanics*. Springer Netherlands, Dordrecht (2011).

[200] Lewis, N. S. Toward cost-effective solar energy use. *Science*, (2007), 798.

[201] Li, Q., Vincent, J. B., Libby, E., Chang, H.-R., Huffman, J. C., Boyd, P. D., Christou, G., and Hendrickson, D. N. Structure, magnetochemistry and biological relevance of [mn4o3cl4(oac)3(py)3], a complex with s = 9/2 ground state. *Angewandte Chemie International Edition*, **27** (1988), 1731.

[202] Li Manni, G., Carlson, R. K., Luo, S., Ma, D., Olsen, J., Truhlar, D. G., and Gagliardi, L. Multiconfiguration pair-density functional theory. *Journal of Chemical Theory and Computation*, **10** (2014), 3669.

[203] Lin, P. H., Takase, M. K., and Agapie, T. Investigations of the effect of the non-manganese metal in heterometallic-oxido cluster models of the oxygen evolving complex of photosystem ii: Lanthanides as substitutes for calcium. *Inorganic Chemistry*, **54** (2015), 59.

[204] Liu, Y., Xiang, R., Du, X., Ding, Y., and Ma, B. An efficient oxygen evolving catalyst based on a μ–o diiron coordination complex. *Chem. Commun.*, **50** (2014), 12779.

[205] Lohmiller, T., Krewald, V., Sedoud, A., Rutherford, A. W., Neese, F., Lubitz, W., Pantazis, D. A., and Cox, N. The first state in the catalytic cycle of the water-oxidizing enzyme: Identification of a water-derived μ-hydroxo bridge. *Journal of the American Chemical Society*, **139** (2017), 14412.

[206] Lohmiller, T., et al. Structure, ligands and substrate coordination of the oxygen-evolving complex of photosystem ii in the s2 state: a combined epr and dft study. *Physical Chemistry Chemical Physics*, **16** (2014), 11877.

[207] Lohmuller, T., Cox, N., Su, J.-H., Messinger, J., and Lubitz, W. *J. Biol. Chem.*, (2012), 24721.

[208] Loll, B., Kern, J., Saenger, W., Zouni, A., and Biesiadka, J. *Nature*, (2005), 1040.

[209] Loup, V. Computer "experiments" on classical fluids. i. thermodynamical properties of lennard-jones molecules. *Physical Review*, **159** (1967), 98.

[210] Loyola-Vargas, V. M. and Vazquez-Flota, F. *Plant Cell Culture Protocols*. Humana Press (2006).

[211] Lubitz, W., Reijerse, E. J., and Messinger, J. Solar water-splitting into h2 and o2: design principles of photosystem ii and hydrogenases. *Energy Environ. Sci.*, **1** (2008), 15.

[212] Luo, G.-Y., Huang, H.-H., Wang, J.-W., and Lu, T.-B. Further investigation of a nickel-based homogeneous water oxidation catalyst with two cis labile sites. *ChemSusChem*, **9** (2016), 485.

[213] Ma, D., Li Manni, G., and Gagliardi, L. The generalized active space concept in multiconfigurational self-consistent field methods. *The Journal of Chemical Physics*, **135** (2011), 044128.

[214] Maeda, K. and Domen, K. Photocatalytic water splitting: Recent progress and future challenges. *The Journal of Physical Chemistry Letters*, **1** (2010), 2655.

[215] Malmqvist, P. A., Rendell, A., and Roos, B. O. The restricted active space self-consistent-field method, implemented with a split graph unitary group approach. *The Journal of Physical Chemistry*, **94** (1990), 5477.

[216] Mantele, W. Reaction-induced infrared difference spectroscopy for the study of protein function and reaction mechanisms. *Trends in Biochemical Sciences*, **18** (1993), 197.

[217] Marchiori, D., Oyala, P., Debus, R., Stich, T., and Britt, R. Structural effects of ammonia binding to the mn4cao5 cluster of photosystem ii. *J Phys Chem B*, (2018), 1588–1599.

[218] Materna, K. L., Jiang, J., Regan, K. P., Schmuttenmaer, C. A., Crabtree, R. H., and Brudvig, G. W. Optimization of photoanodes for photocatalytic water oxidation by combining a heterogenized iridium water-oxidation catalyst with a high-potential porphyrin photosensitizer. *ChemSusChem*, **10** (2017), 4526.

[219] Mathew, S., et al. Dye-sensitized solar cells with 13% efficiency achieved through the molecular engineering of porphyrin sensitizers. *Nature Chemistry*, **6** (2014), 242.

[220] Mattioli, G., Giannozzi, P., Amore Bonapasta, A., and Guidoni, L. Reaction pathways for oxygen evolution promoted by cobalt catalyst. *Journal of the American Chemical Society*, **135** (2013), 15353.

[221] McWeeny, R. *Methods of Molecular Quantum Mechanics*. Academic Press, London (1992).

[222] Messinger, J., Robblee, J. H., Yu, W. O., Sauer, K., Yachandra, V. K., and Klein, M. P. The s0 state of the oxygen-evolving complex in photosystem ii is paramagnetic: Detection of an epr multiline signal. *Journal of the American Chemical Society*, **119** (1997), 11349.

[223] Miqyass, M., Marosvölgyi, M. A., Nagel, Z., Yocum, C. F., and van Gorkom, H. J. S-state dependence of the calcium requirement and binding characteristics in the oxygen-evolving complex of photosystem ii. *Biochemistry*, **47** (2008), 7915.

[224] Mizusawa, N., Kimura, Y., Ishii, A., Yamanari, T., Nakazawa, S., Teramoto, H., and Ono, T.-a. Impact of replacement of d1 c-terminal alanine with glycine on structure and function of photosynthetic oxygen-evolving complex. *Journal of Biological Chemistry*, **279** (2004), 29622.

[225] Moore, G. F., Blakemore, J. D., Milot, R. L., Hull, J. F., Song, H.-e., Cai, L., Schmuttenmaer, C. A., Crabtree, R. H., and Brudvig, G. W. A visible light water-splitting cell with a photoanode formed by codeposition of a high-potential porphyrin and an iridium water-oxidation catalyst. *Energy Environ. Sci.*, **4** (2011), 2389.

[226] Morris, N. D. and Mallouk, T. E. A high-throughput optical screening method for the optimization of colloidal water oxidation catalysts. *Journal of the American Chemical Society*, **124** (2002), 11114.

[227] Mukherjee, S., et al. Synthetic model of the asymmetric [mn3cao4] cubane core of the oxygen-evolving complex of photosystem ii. *Proceedings of the National Academy of Sciences*, **109** (2012), 2257.

[228] Mukhopadhyay, S., Mandal, S. K., Bhaduri, S., and Armstrong, W. H. Manganese clusters with relevance to photosystem ii. *Chemical Reviews*, **104** (2004), 3981.

[229] Mullins, C. S. and Pecoraro, V. L. Reflections on small molecule manganese models that seek to mimic photosynthetic water oxidation chemistry. *Coordination chemistry reviews*, **252** (2008), 416.

[230] Munzarova, M. and Kaupp, M. A critical validation of density functional and coupled-cluster approaches for the calculation of epr hyperfine coupling constants in transition metal complexes. *The Journal of Physical Chemistry A*, **103** (1999), 9966.

[231] Munzarova, M. L., Kubacek, P., and Kaupp, M. Mechanisms of epr hyperfine coupling in transition metal complexes. *Journal of the American Chemical Society*, **122** (2000), 11900.

[232] Mussini, P. R., Biroli, A. O., Tessore, F., Pizzotti, M., Biaggi, C., Carlo, G. D., Lobello, M. G., and Angelis, F. D. Modulating the electronic properties of asymmetric push–pull and symmetric zn(ii)-diarylporphyrinates with para substituted phenylethynyl moieties in 5,15 meso positions: A combined electrochemical and spectroscopic investigation. *Electrochimica Acta*, **85** (2012), 509 .

[233] Najafpour, M. M., Ehrenberg, T., Wiechen, M., and Kurz, P. Communication. *Angewandte Chemie International Edition*, **49** (2010), 2233.

[234] Najafpour, M. M., Moghaddam, A. N., Sedigh, D. J., and Hołyńska, M. A dinuclear iron complex with a single oxo bridge as an efficient water-oxidizing catalyst in the presence of cerium(iv) ammonium nitrate: new findings and current controversies. *Catal. Sci. Technol.*, **4** (2014), 30.

[235] Najafpour, M. M., et al. Manganese compounds as water-oxidizing catalysts: From the natural water-oxidizing complex to nanosized manganese oxide structures. *Chemical Reviews*, **116** (2016), 2886.

[236] Nakamura, S., Ota, K., Shibuya, Y., and Noguchi, T. Role of a water network around the mn4cao5 cluster in photosynthetic water oxidation: A fourier transform infrared spectroscopy and quantum mechanics/molecular mechanics calculation study. *Biochemistry*, **55** (2016), 597.

[237] Nakazono, T., Parent, A. R., and Sakai, K. Cobalt porphyrins as homogeneous catalysts for water oxidation. *Chem. Commun.*, **49** (2013), 6325.

[238] Nara, M., Torii, H., and Tasumi, M. Correlation between the vibrational frequencies of the carboxylate group and the types of its coordination to a metal ion: An ab initio molecular orbital study. *The Journal of Physical Chemistry*, **100** (1996), 19812.

[239] Naruta, Y., Sasayama, M.-a., and Sasaki, T. Oxygen evolution by oxidation of water with manganese porphyrin dimers. *Angewandte Chemie International Edition in English*, **33** (1994), 1839.

[240] Narzi, D., Bovi, D., De Gaetano, P., and Guidoni, L. Dynamics of the special pair of chlorophylls of photosystem ii. *Journal of the American Chemical Society*, **138** (2016), 257.

[241] Narzi, D., Bovi, D., and Guidoni, L. Pathway for mn-cluster oxidation by tyrosine-z in the s2 state of photosystem ii. *Proceedings of the National Academy of Sciences*, **111** (2014), 8723.

[242] Neese, F. Definition of corresponding orbitals and the diradical character in broken symmetry dft calculations on spin coupled systems. *Journal of Physics and Chemistry of Solids*, **65** (2004), 781 .

[243] Neese, F. Prediction of molecular properties and molecular spectroscopy with density functional theory: From fundamental theory to exchange-coupling. *Coordination Chemistry Reviews*, **253** (2009), 526 .

[244] Neese, F. The orca program system. *Wiley Interdisciplinary Reviews: Computational Molecular Science*, **2** (2012), 73.

[245] Nocera, D. G. The artificial leaf. *Accounts of Chemical Research*, **45** (2012), 767.

[246] Noguchi, T. Light-induced ftir difference spectroscopy as a powerful tool toward understanding the molecular mechanism of photosynthetic oxygen evolution. *Photosynthesis Research*, **91** (2007), 59.

[247] Noguchi, T. Fourier transform infrared analysis of the photosynthetic oxygen-evolving center. *Coordination Chemistry Reviews*, **252** (2008), 336.

[248] Noguchi, T. and Berthomieu, C. *Photosystem II: The Light-Driven Water:Plastoquinone Oxidoreductase*, chap. Molecular analysis by vibrational spectroscopy, pp. 367–387. Springer, Dordrecht, The Netherlands (2005).

[249] Noguchi, T., Inoue, Y., and Tang, X. Structural coupling between the oxygen-evolving mn cluster and a tyrosine residue in photosystem ii as revealed by fourier transform infrared spectroscopy. *Biochemistry*, **36** (1997), 14705.

[250] Noguchi, T., Inoue, Y., and Tang, X.-S. Structure of a histidine ligand in the photosynthetic oxygen-evolving complex as studied by light-induced fourier transform infrared difference spectroscopy. *Biochemistry*, **38** (1999), 10187.

[251] Noguchi, T., Ono, T., and Inoue, Y. Detection of structural changes upon s1-to-s2 transition in the oxygen-evolving manganese cluster in photosystem ii by light-induced fourier transform infrared difference spectroscopy. *Biochemistry*, **31** (1992), 5953.

[252] Noguchi, T., Ono, T.-a., and Inoue, Y. A carboxylate ligand interacting with water in the oxygen-evolving center of photosystem ii as revealed by fourier transform infrared spectroscopy. *Biochimica et Biophysica Acta (BBA) - Bioenergetics*, **1232** (1995), 59.

[253] Noguchi, T., Ono, T.-a., and Inoue, Y. Direct detection of a carboxylate bridge between mn and ca2+ in the photosynthetic oxygen-evolving center by means of fourier transform infrared spectroscopy. *Biochimica et Biophysica Acta (BBA) - Bioenergetics*, **1228** (1995), 189.

[254] Noguchi, T. and Sugiura, M. Flash-induced fourier transform infrared detection of the structural changes during the s-state cycle of the oxygen-evolving complex in photosystem ii. *Biochemistry*, **40** (2001), 1497.

[255] Noguchi, T. and Sugiura, M. Ftir detection of water reactions during the flash-induced s-state cycle of the photosynthetic water-oxidizing complex. *Biochemistry*, **41** (2002), 15706.

[256] Noodleman, L. Valence bond description of antiferromagnetic coupling in transition metal dimers. *The Journal of Chemical Physics*, **74** (1981), 5737.

[257] Nuijs, A. M., van Gorkom, H. J., Plijter, J. J., and Duysens, L. N. Primary-charge separation and excitation of chlorophyll a in photosystem ii particles from spinach as studied by picosecond absorbance-difference spectroscopy. *Biochimica et Biophysica Acta (BBA) - Bioenergetics*, **848** (1986), 167.

[258] Odoh, S. O., Manni, G. L., Carlson, R. K., Truhlar, D. G., and Gagliardi, L. Separated-pair approximation and separated-pair pair-density functional theory. *Chem. Sci.*, **7** (2016), 2399.

[259] Okamura, M., et al. A pentanuclear iron catalyst designed for water oxidation. *Nature*, **530** (2016), 465.

[260] Oomens, J. and Steill, J. D. The structure of deprotonated tri-alanine and its a3-fragment anion by ir spectroscopy. *Journal of the American Society for Mass Spectrometry*, **21** (2010), 698.

[261] Oyala, P. H., Stich, T. A., Debus, R. J., and Britt, R. D. Ammonia binds to the dangler manganese of the photosystem ii oxygen-evolving complex. *Journal of the American Chemical Society*, **137** (2015), 8829.

[262] Oyala, P. H., Stich, T. A., Stull, J. A., Yu, F., Pecoraro, V. L., and Britt, R. D. Pulse electron paramagnetic resonance studies of the interaction of methanol with the s2 state of the mn4o5ca cluster of photosystem ii. *Biochemistry*, **53** (2014), 7914.

[263] Pace, R., Smith, P., Bramley, R., and Stehlik, D. Epr saturation and temperature dependence studies on signals from the oxygen-evolving centre of photosystem ii. *Biochimica et Biophysica Acta (BBA) - Bioenergetics*, **1058** (1991), 161 .

[264] Pantazis, D. A. Missing pieces in the puzzle of biological water oxidation. *ACS Catalysis*, **8** (2018), 9477.

[265] Pantazis, D. A., Ames, W., Cox, N., Lubitz, W., and Neese, F. *Angew. Chem. Int. Ed.*, (2012), 9935.

[266] Pantazis, D. A., Ames, W., Cox, N., Lubitz, W., and Neese, F. Two interconvertible structures that explain the spectroscopic properties of the oxygen-evolving complex of photosystem ii in the s2 state. *Angewandte Chemie International Edition*, **51** (2012), 9935.

[267] Pantazis, D. A., Orio, M., Petrenko, T., Zein, S., Lubitz, W., Messinger, J., and Neese, F. Structure of the oxygen-evolving complex of photosystem ii: information on the s2 state through quantum chemical calculation of its magnetic properties. *Phys. Chem. Chem. Phys.*, **11** (2009), 6788.

[268] Parent, A. R., Nakazono, T., Lin, S., Utsunomiya, S., and Sakai, K. Mechanism of water oxidation by non-heme iron catalysts when driven with sodium periodate. *Dalton Trans.*, **43** (2014), 12501.

[269] Patchkovskii, S. and Ziegler, T. Prediction of electron paramagnetic resonance g-tensors of transition metal complexes using density functional theory: First applications to some axial d1mex4 systems. *The Journal of Chemical Physics*, **111** (1999), 5730.

[270] Paul, S., Cox, N., and Pantazis, D. A. What can we learn from a biomimetic model of nature's oxygen-evolving complex? *Inorganic Chemistry*, **7** (2017), 3875.

[271] Pavacik, P. S., Huffman, J. C., and Christou, G. A manganese(iv) complex with phenoxide- and carboxylate-like ligation: preparation and structure of [mn(sal)2(bipyl)](h2sal = salicylic acid; bipy = 2,2'-bipyridine). *Journal of Chemical Society, Chemical Communications*, (1986), 43.

[272] Pearce, J. M. Photovoltaics—a path to sustainable futures. *Futures*, **34** (2002), 663.

[273] Pecoraro, V. L., Baldwin, M. J., Tyler Caudle, M., Hsieh, W.-Y., and Law, N. A. A proposal for water oxidation in photosystem ii. *Pure and Applied Chemistry*, **70** (1998), 925.

[274] Peloquin, J. M., Campbell, K. A., Randall, D. W., Evanchik, M. A., Pecoraro, V. L., Armstrong, W. H., and Britt, R. D. *J. Am. Chem. Soc.*, (2000), 10926.

[275] Peloquin, J. M., Campbell, K. A., Randall, D. W., Evanchik, M. A., Pecoraro, V. L., Armstrong, W. H., and Britt, R. D. 55mn endor of the s2-state multiline epr signal of photosystem ii: Implications on the structure of the tetranuclear mn cluster. *Journal of the American Chemical Society*, **122** (2000), 10926.

[276] Perdew, J. P. Density-functional approximation for the correlation energy of the inhomogeneous electron gas. *Physical Review B*, **33** (1986), 8822.

[277] Perdew, J. P., Burke, K., and Ernzerhof, M. Generalized gradient approximation made simple. *Physical Review Letters*, **77** (1996), 3865.

[278] Perdew, J. P., Burke, K., and Ernzerhof, M. Generalized gradient approximation made simple. *Physical review letters*, **77** (1996), 3865.

[279] Perdew, J. P. and Yue, W. Accurate and simple density functional for the electronic exchange energy: Generalized gradient approximation. *Physical Review B*, **33** (1986), 8800.

[280] Perez-Navarro, M. e. a. Ammonia binding to the oxygen-evolving complex of photosystem ii identifies the solvent-exchangeable oxygen bridge (mu-oxo) of the manganese tetramer. *PNAS USA*, (2013), 15561–15566.

[281] Pickett, W. E., Erwin, S. C., and Ethridge, E. C. Reformulation of the LDA + u method for a local-orbital basis. *Physical Review B*, **58** (1998), 1201.

[282] Pizzolato, E., et al. Light driven water oxidation by a single site cobalt salophen catalyst. *Chem. Commun.*, **49** (2013), 9941.

[283] Powell, B. J., Baruah, T., Bernstein, N., Brake, K., McKenzie, R. H., Meredith, P., and Pederson, M. R. A first-principles density-functional calculation of the electronic and vibrational structure of the key melanin monomers. *The Journal of Chemical Physics*, **120** (2004), 8608.

[284] Pulay, P., Fogarasi, G., Pang, F., and Boggs, J. E. Systematic ab initio gradient calculation of molecular geometries, force constants, and dipole moment derivatives. *Journal of the American Chemical Society*, **101** (1979), 2550.

[285] Raines, C. A. The calvin cycle revisited. *Photosynthesis Research*, **75** (2003), 1.

[286] Ramírez, A., Bogdanoff, P., Friedrich, D., and Fiechter, S. Synthesis of ca2mn3o8 films and their electrochemical studies for the oxygen evolution reaction (oer) of water. *Nano Energy*, **1** (2012), 282.

[287] Rappaport, F. and Diner, B. A. Primary photochemistry and energetics leading to the oxidation of the (mn)4ca cluster and to the evolution of molecular oxygen in photosystem ii. vol. 252, pp. 259–272 (2008).

[288] Rappaport, F., Guergova-Kuras, M., Nixon, P. J., Diner, B. A., and Lavergne, J. Kinetics and pathways of charge recombination in photosystem ii. *Biochemistry*, **41** (2002), 8518.

[289] Remenyi, C. and Kaupp, M. Where is the spin? understanding electronic structure and g-tensors for ruthenium complexes with redox-active quinonoid ligands. *Journal of the American Chemical Society*, **127** (2005), 11399.

[290] Renger, G. A model for the molecular mechanism of photosynthetic oxygen evolution. *FEBS Letters*, **81** (1977), 223.

[291] Renger, G. Mechanistic aspects of photosynthetic water cleavage. *Photosynthetica*, **21** (1987), 203.

[292] Renger, G., Jori, G., Hader, D. P., and Lancaster, R. *Primary Processes of Photosynthesis: Principles and Apparatus. Comprehensive Series in Photochemical and Photobiological Sciences*. RSC Publishing: Cambridge (2008).

[293] Retegan, M., Cox, N., Lubitz, W., Neese, F., and Pantazis, D. A. The first tyrosyl radical intermediate formed in the s2–s3 transition of photosystem ii. *Phys. Chem. Chem. Phys.*, **16** (2014), 11901.

[294] Retegan, M., Krewald, V., Mamedov, F., Neese, F., Lubitz, W., Cox, N., and Pantazis, D. A. A five-coordinate mn(iv) intermediate in biological water oxidation: spectroscopic signature and a pivot mechanism for water binding. *Chemical Science*, **7** (2016), 72.

[295] Reviakine, R., Arbuznikov, A. V., Tremblay, J.-C., Remenyi, C., Malkina, O. L., Malkin, V. G., and Kaupp, M. Calculation of zero-field splitting parameters: Comparison of a two-component noncolinear spin-density-functional method and a one-component perturbational approach. *The Journal of Chemical Physics*, **125** (2006), 054110.

[296] Rochaix, J.-D. Regulation of photosynthetic electron transport. *Biochimica et Biophysica Acta (BBA) - Bioenergetics*, **1807** (2011), 375 .

[297] Rohith, P. J., Anandram, S., Maliyeckal, R. P. K., and Hoong-Kun, F. Chelating behavior of 2-hydroxyacetophenone n(4)-disubstituted thiosemicarbazones: Facile formation of mn(iv) complexes – x-ray structure, epr and cyclic voltammetric studies. *Polyhedron*, **24** (2005), 601.

[298] Roos, B. O. *The Complete Active Space Self-Consistent Field Method and its Applications in Electronic Structure Calculations*, pp. 399–445. John Wiley & Sons, Ltd (2007). ISBN 9780470142943.

[299] Rossi, F. D., Pontecorvo, T., and Brown, T. M. Characterization of photovoltaic devices for indoor light harvesting and customization of flexible dye solar cells to deliver superior efficiency under artificial lighting. *Applied Energy*, **156** (2015), 413 .

[300] Ruettinger, W. F., Campana, C., and Dismukes, G. C. Synthesis and characterization of mn4o4l6 complexes with cubane-like core structure: A new class of models of the active site of the photosynthetic water oxidase. *Journal of the American Chemical Society*, **119** (1997), 6670.

[301] Saadeh, S. M., Lah, M. S., and Pecoraro, V. L. Manganese complexes of .alpha.-hydroxy acids. *Inorganic Chemistry*, **30** (1991), 8.

[302] Sanakis, Y., Sarrou, J., Zahariou, G., and Petrouleas, V. Q-band electron paramagnetic resonance studies of the s3 state of the oec of photosystem ii. In *Photosynthesis. Energy from the Sun* (edited by J. F. Allen, E. Gantt, J. H. Golbeck, and B. Osmond), pp. 479–482. Springer Netherlands, Dordrecht (2008).

[303] Sauer, K., Yachandra, V., Britt, R., and Klein, M. The photosynthetic water oxidation complex studied by epr and x-ray absorption spectroscopy. *Manganese Redox Enzymes*, (1992), 141.

[304] Sauer, K. and Yachandra, V. K. *Proc. Natl. Acad. Sci. U. S. A.*, (2002), 8631.

[305] Schaftenaar, G. and Noordik, J. Molden: a pre- and post-processing program for molecular and electronic structures*. *Journal of Computer-Aided Molecular Design*, **14** (2000), 123.

[306] Schaftenaar, G., Vlieg, E., and Vriend, G. Molden 2.0: quantum chemistry meets proteins. *Journal of Computer-Aided Molecular Design*, **31** (2017), 789.

[307] Schmitt, F.-J., Maksimov, E., Hatti, P., Weissenborn, J., Jeyasangar, V., Razjivin, A., Paschenko, V., Friedrich, T., and Renger, G. Coupling of different isolated photosynthetic light harvesting complexes and cdse/zns nanocrystals via förster resonance energy transfer. *Biochimica et Biophysica Acta (BBA) - Bioenergetics*, **1817** (2012), 1461.

[308] Schraut, J. and Kaupp, M. On ammonia binding to the oxygen-evolving complex of photosystemii: A quantum chemical study. *Chemistry – A European Journal*, **20** (2014), 7300.

[309] Schwabe, T. and Grimme, S. Towards chemical accuracy for the thermodynamics of large molecules: new hybrid density functionals including non-local correlation effects. *Physical Chemistry and Chemical Physics*, **8** (2006), 4398.

[310] Schwabe, T. and Grimme, S. Double-hybrid density functionals with long-range dispersion corrections: higher accuracy and extended applicability. *Physical Chemistry Chemical Physics*, **9** (2007), 3397.

[311] Service, R. J., Hillier, W., and Debus, R. J. Evidence from ftir difference spectroscopy of an extensive network of hydrogen bonds near the oxygen-evolving mn4ca cluster of photosystem ii involving d1-glu65, d2-glu312, and d1-glu329. *Biochemistry*, **49** (2010), 6655.

[312] Service, R. J., Hillier, W., and Debus, R. J. Network of hydrogen bonds near the oxygen-evolving mn4cao5 cluster of photosystem ii probed with ftir difference spectroscopy. *Biochemistry*, **53** (2014), 1001.

[313] Service, R. J., Yano, J., Dilbeck, P. L., Burnap, R. L., Hillier, W., and Debus, R. J. Participation of glutamate-333 of the d1 polypeptide in the ligation of the mn4cao5 cluster in photosystem ii. *Biochemistry*, **52** (2013), 8452.

[314] Service, R. J., et al. Participation of glutamate-354 of the cp43 polypeptide in the ligation of manganese and the binding of substrate water in photosystem ii. *Biochemistry*, **50** (2011), 63.

[315] Shen, J.-R. The structure of photosystem ii and the mechanism of water oxidation in photosynthesis. *Annual Review of Plant Biology*, **66** (2015), 23.

[316] Shimada, Y., Suzuki, H., Tsuchiya, T., Mimuro, M., and Noguchi, T. Structural coupling of an arginine side chain with the oxygen-evolving mn4ca cluster in photosystem ii as revealed by isotope-edited fourier transform infrared spectroscopy. *Journal of the American Chemical Society*, **133** (2011), 3808.

[317] Shimada, Y., Suzuki, H., Tsuchiya, T., Tomo, T., Noguchi, T., and Mimuro, M. Effect of a single-amino acid substitution of the 43 kda chlorophyll protein on the oxygen-evolving reaction of the cyanobacterium synechocystis sp. pcc 6803: Analysis of the glu354gln mutation. *Biochemistry*, **48** (2009), 6095.

[318] Shoji, M., Isobe, H., Shen, J.-R., and Yamaguchi, K. Geometric and electronic structures of the synthetic mn4cao4 model compound mimicking the photosynthetic oxygen-evolving complex. *Physical Chemistry Chemical Physics*, **18** (2016), 11330.

[319] Shoji, M., Isobe, H., Yamanaka, S., Suga, M., Akita, F., Shen, J.-R., and Yamaguchi, K. On the guiding principles for lucid understanding of the damage-free s1 structure of the camn4o5 cluster in the oxygen evolving complex of photosystem ii. *Chemical Physics Letters*, **627** (2015), 44.

[320] Siegbahn, P. E. A structure-consistent mechanism for dioxygen formation in photosystem ii. *Chemistry-A European Journal*, **14** (2008), 8290.

[321] Slater, J. C. Note on hartree's method. *Physical Review*, **35** (1930), 210.

[322] Slater, J. C. A simplification of the hartree-fock method. *Physical Review*, **81** (1951), 385.

[323] Solomon, E. I., Szilagyi, R. K., DeBeer George, S., and Basumallick, L. Electronic structures of metal sites in proteins and models: Contributions to function in blue copper proteins. *Chemical Reviews*, **104** (2004), 419.

[324] Solovyev, I. V., Dederichs, P. H., and Anisimov, V. I. Corrected atomic limit in the local-density approximation and the electronic structure of d impurities in rb. *Physical Review B*, **50** (1994), 16861.

[325] Sproviero, E. M., Gascón, J. A., McEvoy, J. P., Brudvig, G. W., and Batista, V. S. Quantum mechanics/molecular mechanics study of the catalytic cycle of water splitting in photosystem ii. *Journal of the American Chemical Society*, **130** (2008), 3428.

[326] Steill, J. D. and Oomens, J. Action spectroscopy of gas-phase carboxylate anions by multiple photon ir electron detachment/attachment. *The Journal of Physical Chemistry A*, **113** (2009), 4941.

[327] Stephens, P., Devlin, F., Chabalowski, C., and Frisch, M. Ab initio calculation of vibrational absorption and circular dichroism spectra using density functional force fields. *Journal of Physical Chemistry*, **7** (1994), 11623.

[328] Stich, T., Yeagle, G., Service, R., Debus, R., and Britt, R. *Biochemistry*, (2011), 7390.

[329] Strickler, M. A., Hillier, W., and Debus, R. J. No evidence from ftir difference spectroscopy that glutamate-189 of the d1 polypeptide ligates a mn ion that undergoes oxidation during the s0 to s1, s1 to s2, or s2 to s3 transitions in photosystem ii. *Biochemistry*, **45** (2006), 8801.

[330] Strickler, M. A., Hwang, H. J., Burnap, R. L., Yano, J., Walker, L. M., Service, R. J., Britt, R. D., Hillier, W., and Debus, R. J. Glutamate-354 of the cp43 polypeptide interacts with the oxygen-evolving mn4ca cluster of photosystem ii: a preliminary characterization of the glu354gln mutant. *Philosophical Transactions of the Royal Society B: Biological Sciences*, **363** (2008), 1179.

[331] Strickler, M. A., Walker, L. M., Hillier, W., Britt, R. D., and Debus, R. J. No evidence from ftir difference spectroscopy that aspartate-342 of the d1 polypeptide ligates a mn ion that undergoes oxidation during the s0 to s1, s1 to s2, or s2 to s3 transitions in photosystem ii. *Biochemistry*, **46** (2007), 3151.

[332] Stull, J., Stich, T., Service, R., Debus, R., Mandal, S., Armstrong, W., and Britt, R. *J Am Chem Soc*, (2010), 446.

[333] Styring, S., Feyziyev, Y., Mamedov, F., Hillier, W., and Babcock, G. T. ph dependence of the donor side reactions in ca2+-depleted photosystem ii. *Biochemistry*, **42** (2003), 6185.

[334] Su, J. H., et al. *Biochim. Biophys. Acta*, (2011), 1807.

[335] Suga, M., et al. Native structure of photosystem ii at 1.95 å resolution viewed by femtosecond x-ray pulses. *Nature*, **517** (2014), 99.

[336] Sugiura, M., Azami, C., Koyama, K., Rutherford, A. W., Rappaport, F., and Boussac, A. Modification of the pheophytin redox potential in thermosynechococcus elongatus photosystem ii with psba3 as d1. *Biochimica et Biophysica Acta (BBA) - Bioenergetics*, **1837** (2014), 139.

[337] Sutton, C. C., da Silva, G., and Franks, G. V. Modeling the ir spectra of aqueous metal carboxylate complexes: Correlation between bonding geometry and stretching mode wavenumber shifts. *Chemistry—A European Journal*, **21** (2015), 6801.

[338] Swanson, R. M. Photovoltaics power up. *Science*, **324** (2009), 891.

[339] Swope, W. C., Andersen, H. C., Berens, P. H., and Wilson, K. R. A computer simulation method for the calculation of equilibrium constants for the formation of physical clusters of molecules: Application to small water clusters. *The Journal of Chemical Physics*, **76** (1982), 637.

[340] Szabo, A. and Ostlund, N. S. *Modern Theoretical Chemistry*. MacMillan Pub. Inc., New York (1982).

[341] Takei, K.-i., Takahashi, R., and Noguchi, T. Correlation between the hydrogen-bond structures and the c=o stretching frequencies of carboxylic acids as studied by density functional theory calculations: Theoretical basis for interpretation of infrared bands of carboxylic groups in proteins. *The Journal of Physical Chemistry B*, **112** (2008), 6725.

[342] Tamm, L. K. and Tatulian, S. A. Infrared spectroscopy of proteins and peptides in lipid bilayers. *Quarterly Reviews of Biophysics*, **30** (1997), 365.

[343] Tao, J., Perdew, J. P., Staroverov, V. N., and Scuseria, G. E. Climbing the density functional ladder: Nonempirical meta–generalized gradient approximation designed for molecules and solids. *Physical Review Letters*, **91** (2003), 146401.

[344] Terrett, R., Petrie, S., Stranger, R., and J. Pace, R. What computational chemistry and magnetic resonance reveal concerning the oxygen evolving centre in photosystem ii. *Journal of Inorganic Biochemistry*, **162** (2016), 178 .

[345] Trissl, H.-W. and Leibl, W. Primary charge separation in photosystem ii involves two electrogenic steps. *FEBS Letters*, **244** (1989), 85.

[346] Tsui, E. Y. and Agapie, T. Reduction potentials of heterometallic manganese–oxido cubane complexes modulated by redox-inactive metals. *Proceedings of the National Academy of Sciences*, **110** (2013), 10084.

[347] Tsui, E. Y., Kanady, J. S., and Agapie, T. Synthetic cluster models of biological and heterogeneous manganese catalysts for o2 evolution. *Inorganic chemistry*, **52** (2013), 13833.

[348] Tychengulova, A., Capone, M., Pitari, F., and Guidoni, L. Molecular vibrations of an oxygen-evolving complex and its synthetic mimic. *Chemistry – A European Journal*, **25** (2019), 13385.

[349] Umena, Y., Kawakami, K., Shen, J.-R., and Kamiya, N. Crystal structure of oxygen-evolving photosystem ii at a resolution of 1.9 a. *Nature*, **473** (2008), 55.

[350] van Lenthe, E., Snijders, J. G., and Baerends, E. J. The zero-order regular approximation for relativistic effects: The effect of spin–orbit coupling in closed shell molecules. *The Journal of Chemical Physics*, **105** (1996), 6505.

[351] van Wullen, C. Molecular density functional calculations in the regular relativistic approximation: Method, application to coinage metal diatomics, hydrides, fluorides and chlorides, and comparison with first-order relativistic calculations. *The Journal of Chemical Physics*, **109** (1998), 392.

[352] VandeVondele, J. and Hutter, J. An efficient orbital transformation method for electronic structure calculations. *The Journal of Chemical Physics*, **118** (2003), 4365.

[353] VandeVondele, J. and Hutter, J. Gaussian basis sets for accurate calculations on molecular systems in gas and condensed phases. *The Journal of chemical physics*, **127** (2007), 114105.

[354] VandeVondele, J., Krack, M., Mohamed, F., Parrinello, M., Chassaing, T., and Hutter, J. Quickstep: Fast and accurate density functional calculations using a mixed gaussian and plane waves approach. *Computer Physics Communications*, **167** (2005), 103.

[355] Venyaminov, S. Y. and Kalnin, N. N. Quantitative ir spectrophotometry of peptide compounds in water (h2o) solutions. i. spectral parameters of amino acid residue absorption bands. *Biopolymers*, **30** (1990), 1243.

[356] Vincent, J. B., Christmas, C., Chang, H. R., Li, Q., Boyd, P. D. W., Huffman, J. C., Hendrickson, D. N., and Christou, G. Modeling the photosynthetic water oxidation center. preparation and properties of tetranuclear manganese complexes containing [mn4o2]6+,7+,8+ cores, and the crystal structures of mn4o2(o2cme)6(bipy)2 and [mn4o2(o2cme)7(bipy)2](clo4). *Journal of the American Chemical Society*, **111** (1989), 2086.

[357] Vincent, J. B. and Christou, G. A molecular 'double-pivot' mechanism for water oxidation. *Inorganica Chimica Acta*, **136** (1987), L41.

[358] Vinyard, D. J. and Brudvig, G. W. Progress toward a molecular mechanism of water oxidation in photosystem ii. *Annual Review of Physical Chemistry*, **68** (2017), 101.

[359] Visser, H., Dube, C. E., Armstrong, W. H., Sauer, K., and Yachandra, V. K. Ftir spectra and normal-mode analysis of a tetranuclear manganese adamantane-like complex in two electrochemically prepared oxidation states:

Relevance to the oxygen-evolving complex of photosystem ii. *Journal of the American Chemical Society*, **124** (2002), 11008.

[360] Vittal, K. Y. and Junko, Y. Calcium in the oxygen-evolving complex: Structural and mechanistic role determined by x-ray spectroscopy. *Journal of Photochemistry and Photobiology B: Biology*, **104** (2011), 51 .

[361] Vogel, R. and Siebert, F. Vibrational spectroscopy as a tool for probing protein function. *Current opinion in chemical biology*, **4** (2000), 518.

[362] Vrettos, J. S., Limburg, J., and Brudvig, G. W. Mechanism of photosynthetic water oxidation: combining biophysical studies of photosystem ii with inorganic model chemistry. *Biochimica et Biophysica Acta (BBA) - Bioenergetics*, **1503** (2001), 229.

[363] Vrettos, J. S., Stone, D. A., and Brudvig, G. W. Quantifying the ion selectivity of the ca2+ site in photosystem ii: Evidence for direct involvement of ca2+ in o2 formation. *Biochemistry*, **40** (2001), 7937.

[364] Walter, M. G., Warren, E. L., McKone, J. R., Boettcher, S. W., Mi, Q., Santori, E. A., and Lewis, N. S. Solar water splitting cells. *Chem. Rev.*, (2010), 6446.

[365] Wang, D. and Bruner, C. O. Catalytic water oxidation by a bio-inspired nickel complex with a redox-active ligand. *Inorganic Chemistry*, **56** (2017), 13638.

[366] Wang, J.-W., Hou, C., Huang, H.-H., Liu, W.-J., Ke, Z.-F., and Lu, T.-B. Further insight into the electrocatalytic water oxidation by macrocyclic nickel(ii) complexes: the influence of steric effect on catalytic activity. *Catal. Sci. Technol.*, **7** (2017), 5585.

[367] Weigend, F. and Ahlrichs, R. Balanced basis sets of split valence, triple zeta valence and quadruple zeta valence quality for h to rn: Design and assessment of accuracy. *Phys. Chem. Chem. Phys.*, **7** (2005), 3297.

[368] White, S. R. Density matrix formulation for quantum renormalization groups. *Phys. Rev. Lett.*, **69** (1992), 2863.

[369] White, S. R. Density-matrix algorithms for quantum renormalization groups. *Phys. Rev. B*, **48** (1993), 10345.

[370] White, S. R. and Martin, R. L. Ab initio quantum chemistry using the density matrix renormalization group. *The Journal of Chemical Physics*, **110** (1999), 4127.

[371] Wickramasinghe, L. D., Zhou, R., Zong, R., Vo, P., Gagnon, K. J., and Thummel, R. P. Iron complexes of square planar tetradentate polypyridyl-type ligands as catalysts for water oxidation. *Journal of the American Chemical Society*, **137** (2015), 13260.

[372] Wiechen, M., Berends, H.-M., and Kurz, P. Water oxidation catalysed by manganese compounds: from complexes to 'biomimetic rocks'. *Dalton Transactions*, **41** (2012), 21.

[373] Wiechen, M., Zaharieva, I., Dau, H., and Kurz, P. Layered manganese oxides for water-oxidation: alkaline earth cations influence catalytic activity in a photosystem ii-like fashion. *Chemical Science*, **3** (2012), 2330.

[374] Wieghardt, K. The active sites in manganese-containing metalloproteins and inorganic model complexes. *Angewandte Chemie International Edition in English*, **28** (1989), 1153.

[375] Williamson, A., Conlan, B., Hillier, W., and Wydrzynski, T. The evolution of photosystem ii: insights into the past and future. *Photosynthesis Research*, **107** (2011), 71.

[376] Wise, R. R. and Hoober, J. K. *The Structure and Function of Plastids*. Springer-Verlag (2007).

[377] Woon, D. E. and Dunning, T. H. Gaussian basis sets for use in correlated molecular calculations. iii. the atoms aluminum through argon. *The Journal of Chemical Physics*, **98** (1993), 1358.

[378] Xie, Y., Tang, Y., Wu, W., Wang, Y., Liu, J., Li, X., Tian, H., and Zhu, W.-H. Porphyrin cosensitization for a photovoltaic efficiency of 11.5%: A record for non-ruthenium solar cells based on iodine electrolyte. *Journal of the American Chemical Society*, **137** (2015), 14055.

[379] Yachandra, V., DeRose, V., Latimer, M., Mukerji, I., Sauer, K., and Klein, M. Where plants make oxygen: a structural model for the photosynthetic oxygen-evolving manganese cluster. *Science*, **260** (1993), 675.

[380] Yachandra, V. K., Guiles, R., Sauer, K., and Klein, M. P. The state of manganese in the photosynthetic apparatus: 5. the chloride effect in photosynthetic oxygen evolution. is halide coordinated to the epr-active manganese in the o2-evolving complex? studies of the substructure of the low-temperature multiline epr signal. *Biochimica et Biophysica Acta (BBA) - Bioenergetics*, **850** (1986), 333.

[381] Yachandra, V. K., Sauer, K., and Klein, M. P. Manganese cluster in photosynthesis: Where plants oxidize water to dioxygen. *Chemical Reviews*, **96** (1996), 2927.

[382] Yachandra, V. K., Sauer, K., and Klein, M. P. Manganese cluster in photosynthesis: Where plants oxidize water to dioxygen. *Chemical Reviews*, **96** (1996), 2927.

[383] Yamaguchi, K. Configuration interaction (ci), coupled-cluster (cc) and many-body perturbation (mbpt) approaches in the unrestricted hartree—fock—slater (uhfs) model. *Chemical Physics Letters*, **68** (1979), 477 .

[384] Yang, S., Seth, J., Strachan, J.-P., Gentemann, S., Kim, D., Holten, D., Lindsey, J., and Bocian, D. Ground and excited state electronic properties of halogenated tetraarylporphyrins. tuning the building blocks for porphyrin-based photonic devices. *Journal of Porphyrins and Phthalocyanines*, **3** (1999), 117.

[385] Yano, J. and Yachandra, V. Mn4ca cluster in photosynthesis: Where and how water is oxidized to dioxygen. *Chemical Reviews*, **114** (2014), 4175.

[386] Yano, J. and Yachandra, V. K. *Inorganic Chemistry*, (2008), 1711.

[387] Yano, J., et al. X-ray damage to the mn4ca complex in single crystals of photosystem ii: A case study for metalloprotein crystallography. *Proceedings of the National Academy of Sciences*, **102** (2005), 12047.

[388] Yella, A., et al. Porphyrin-sensitized solar cells with cobalt (ii/iii)–based redox electrolyte exceed 12 percent efficiency. *Science*, **334** (2011), 629.

[389] Yin, G., et al. Synthesis, characterization, and solution properties of a novel cross-bridged cyclam manganese(iv) complex having two terminal hydroxo ligands. *Inorganic Chemistry*, **45** (2006), 8052.

[390] Yocum, C. F. The calcium and chloride requirements of the o2 evolving complex. *Coordination Chemistry Reviews*, **252** (2008), 296.

[391] Young, I. D., et al. Structure of photosystem ii and substrate binding at room temperature. *Nature*, **540** (2016), 453 EP .

[392] Zaharieva, I., Chernev, P., Berggren, G., Anderlund, M., Styring, S., Dau, H., and Haumann, M. Room-temperature energy-sampling kβ x-ray emission spectroscopy of the mn4ca complex of photosynthesis reveals three manganese-centered oxidation steps and suggests a coordination change prior to o2 formation. *Biochemistry*, **55** (2016), 4197.

[393] Zaharieva, I., Chernev, P., Risch, M., Klingan, K., Kohlhoff, M., Fischer, A., and Dau, H. Electrosynthesis, functional, and structural characterization of a water-oxidizing manganese oxide. *Energy & Environmental Science*, **5** (2012), 7081.

[394] Zaharieva, I., Dau, H., and Haumann, M. Sequential and coupled proton and electron transfer events in the s2 $\rightarrow$ s3 transition of photosynthetic water oxidation revealed by time-resolved x-ray absorption spectroscopy. *Biochemistry*, **55** (2016), 6996.

[395] Zhang, C., Chen, C., Dong, H., Shen, J.-R., Dau, H., and Zhao, J. A synthetic mn4ca-cluster mimicking the oxygen-evolving center of photosynthesis. *Science*, **348** (2015), 690.

[396] Zhang, Y. and Yang, W. Comment on "generalized gradient approximation made simple". *Physical Review Letters*, **80** (1998), 890.

[397] Zouni, A., Witt, H.-T., Kern, J., Fromme, P., Kraub, N., Saenger, W., and Orth, P. *Nature*, (2001), 739.